Hollow core negative curvature fibres

Yu, Fei

Award date:
2013

Awarding institution:
University of Bath

HOLLOW CORE NEGATIVE CURVATURE OPTICAL FIBRES

Fei Yu

A thesis submitted for the degree of Doctor of Philosophy

University of Bath
Department of Physics

November 2013

COPYRIGHT

Abstract

Hollow core fibre (HCF) is a type of novel optical fibre which has lower refractive index in the hollow core than in the cladding. Total internal reflection (TIR) cannot explain the confinement of light to the core of a HCF. According to the confinement mechanism, the HCFs can be generally divided into hollow core photonic bandgap fibres and hollow core leaky mode fibres depending on their optical properties of the cladding structure. Hollow core negative curvature fibre (HC-NCF) is a kind of hollow core leaky mode fibre, which is defined by the negative curvature of the core boundary.

This thesis presents my study of HC-NCFs over the last two years. My research has focused on developing low loss silica HC-NCFs and exploring the attenuation limit of HC-NCFs. Fifty different HC-NCFs were fabricated, which covered the spectral range from 800 nm to 4.5 μm. Minimum attenuations of 24.4 dB/km and 85 dB/km were measured at around 2400 nm wavelength and 4000 nm respectively, which are the best achieved in HCFs at these wavelengths to the best of my knowledge. The limits of HC-NCF attenuation were revealed by analysing the data from HC-NCFs scaled for minimum attenuation in different spectral regions.

Other properties of HC-NCFs, including bending loss and dispersion, were also studied experimentally. By using white light interferometery, a low group velocity dispersion (GVD) was found in HC-NCFs, which agrees well with simulations. The bending loss of HC-NCFs was preliminarily studied by measuring the transmission spectra under different bending conditions. Significant bending loss was found when the bending radius was less than 15 cm.

Numerical simulations were performed using COMSOL software to study the properties of HC-NCFs. In the simulations, it was found that the capillary thickness is

the most important factor determining the attenuation of HC-NCFs. These results were used to explain the experimental results.

This thesis is comprised of seven chapters. Chapter 1 and 2 supply background material that helps to understand the light guidance mechanism of HC-NCFs. My original work is presented in Chapter 3, 4, 5, and 6. Chapter 7 includes a summary and suggestions for future work.

Acknowledgement

To pursue a dream in life is never easy. In this journey, from time to time you would deviate from the initial intention. Sometimes you correct it and sometimes you don't, not because you would not like to but you find it may be just too late. Until I start to write down these words, I realise I owe my gratefulness to so many people.

First of all, I would dedicate this thesis to my parents. Although I love Physics and also would like to explore the possibility of making it as my career, this thesis is for you. I wish you would be proud of me. I am happy when you are happy.

Then, Jonathan, you lead me to photonics. I guarantee that I will never forget our first phone talk in the PhD interview. I boasted superconitnuum and you responded humbly to a topic for which you were elected to the rank of OSA fellow the next year. You definitely knew I knew nothing! I will hold the utmost respect for it always.

And William, although you are not my second supervisor, I learn the second most of knowledge from you! You make me wonder how much knowledge one person can absorb! You are amazing!

My thanks also go to Dr. Wei Ding, D.r Yingying Wang, Xuesong Zhao who are my SHIXIONG SHIJIE. Thank you for all of your generous help all the time!

Jim, James, Clarissa, Peter and Sam, all of you deserve my special thanks for your great patience for reading my Chinese style English thesis! I remember I still owe you a big Chinese style feast, don't I!

Finally, thanks go to my colleagues in CPPM, my collaborators and all my friends!

In the finally final, special thanks go to Shan, my love. You are the sugar for the three years' coffee.

Content

Chapter 1 Introduction to hollow core fibres

The first part of Chapter 1 gives a brief history of hollow core fibres. Starting from simple dielectric/metal tube waveguides, hollow core photonic bandgap fibres and hollow core negative curvature fibres with extraordinary optical properties have been developed in parallel with our understanding of optical guidance in hollow core fibres.

In the second part, light-gas interaction, high power laser delivery and ultrafast laser pulse delivery are identified as the main applications of hollow core fibres.

1.1 Overview of hollow core fibres

1.1.1 Early developments (before 1990's)

The history of optical fibres, or to be more precise, the history of optical waveguides, can be traced back to the nineteenth century, when the law of total internal reflection (TIR) had been known by scientists already [1]. In the 1950s, the use of a lower refractive index material as the cladding layer around a thin glass strand led to a considerable improvement in the characteristics of index guiding optical waveguide and, in a sense, it gave birth of the first modern optical fibre [2].

Since the 1960s, the study of optical fibres has developed rapidly. In 1965, C. K. Kao and G. Hockham published an analysis suggesting that optical fibre could be a suitable medium for long-distance telecommunication if the fibre losses could be reduced to below 20 dB/km [3]. Later they predicted that the purification of optical glass in the fibre fabrication could control the fibre loss from material absorption to achieve this limit [3]. In 1970, *Corning Glass Works* fabricated the first optical fibre with the attenuation as low as 17 dB/km [3], and further progress in the optical fibre fabrication technology greatly reduced it to only 0.2 dB/km in the wavelength range near 1.55 μm in 1979 [4]. The successful commercialized mass production of low loss optical fibres announced the start of the era of optical communication. In 2009 the Nobel Prize in Physics was awarded to C K. Kao "for ground-breaking achievements concerning the transmission of light in fibres for optical communication".

The emergence of low loss optical fibre did not only lead to a revolution in modern communication technology in the 20th century but also brought about numerous other industrial applications. Nowadays, the optical fibre is not only an object of fundamental research but also an indispensable tool in the optical laboratories.

Above is about the development of the index guiding optical fibres, which confine light in the core region of higher refractive index by TIR. The other important class of optical fibres is the hollow core fibre (HCF). HCF features a vacuum or air core but light can still be effectively confined and transmitted with low loss. As the refractive index of the air/vacuum is usually lower than the cladding solid material, TIR is no longer valid here to describe the picture of light propagation.

The initial study of HCF can be traced to 1936, in which year Carson, Mead, Schelkunoff, and Southworth from the *Bell Telephone Laboratories* published the first

theoretical work on hollow core waveguide with cylindrical cross-section using a conducting boundary condition [5]. They revealed that in the metal hollow core waveguide, with an increase in frequency, the electromagnetic waves would propagate with lower attenuation [5].

Since World War II, the development of radar system with the aim of military usage greatly promoted the study of waveguide operating at microwave frequencies [6]. In the 1970s, *Bell Labs* developed the first commercial hollow core waveguide system (WT4/WT4A millimeter-wave transmission system) to transport microwave electromagnetic signals (40 – 110 GHz) for telecommunications [7].

A 60-mm-diameter hollow tube was used as the waveguide, the inside of which was coated with copper. The field evaluation test showed that the attenuation of the transmission system stayed below 1 dB/km for the whole operational microwave frequency range from 40 to 110 GHz with the minimum attenuation reaching as low as 0.5 dB/km at 85 GHz [7].

Ten years later, the first metal hollow core waveguide operating at the optical frequencies was demonstrated successfully in 1980 [8]. The hollow core waveguide was designed for CO_2 laser transmission at the wavelength of 10.6 μm and it achieved 1 dB/m attenuation level at that wavelength. Ever since, more and more metal hollow core waveguides appeared in both laboratories and industries, varying in shape and inner coating materials [9]. In 1992, Miyagi and his colleagues developed a hollow core phosphor bronze strip waveguide with thin-film coatings of ZnS, PbTe and PbF_2 [10]. Their waveguide achieved 0.1 dB/m attenuation at the wavelength of 10.6 μm. In the same year the delivery of 2.7 kW continuous-wave CO_2 laser was achieved in a 2 m long germanium-coated Ag metal waveguide [11].

The first systematic study of dielectric hollow core waveguide operating in the optical frequency range originated from a theoretical paper by Marcatili and Schmeltzer in the 1960's [12]. In that paper, they used an analytical method to estimate the attenuation level of dielectric hollow core tube for the first time (under the assumption of infinite cladding) and pointed out that a trade-off between the transmission loss and bending loss fundamentally limited the potential use of dielectric hollow core waveguide as a long-haul communication medium.

Since Marcatili and Schmeltzer's pioneering work, the development of dielectric hollow core waveguide was very slow until the appearance of hollow core photonic

bandgap fibre (HC-PBG) [13] and other micro-structured HCFs. Such slow progress was partly due to challenges of fabricating hollow core structure in optical fibres on the scale of micrometers. In addition, some inherent disadvantages of dielectric hollow core waveguides limited development and applications.

Comparing with metal material, the dielectric cannot provide high reflectivity over a broad frequency range. Usually at long wavelengths, most dielectric materials exhibit strong phonon absorption, which fundamentally limits the application of dielectric hollow core waveguides in those wavelength ranges. In contrast, the metal hollow core waveguide, in advance of dielectric hollow core waveguides, had already achieved great success in electromagnetic wave transmission in both the microwave and mid/far-infrared spectral regions. Today, in industry, the metal hollow core waveguide is still preferred for mid-infrared laser transmission [9].

At optical wavelengths dielectric materials can exhibit great transparency; however, the dielectric hollow core waveguide usually suffers from a higher transmission loss than the corresponding index guiding waveguide. This is fundamentally determined by its leaky confinement. Today the common commercial single mode fibre made of silica material can achieve 0.17 dB/km or 0.18 dB/km attenuation near 1550 nm [15]. It is extremely difficult for a silica HCF to compete with the silica single mode fibre in terms of transmission loss in this spectral range.

Consequently, in the early stage when waveguides were mainly used as transmission media of light, the dielectric hollow core waveguide stayed unnoticed. With the emergence of HC-PBG and other novel HCFs with complex structure design, a much lower loss has been achieved. More importantly, such novel designs bring in unique optical properties which much extend their application in both industry and scientific researches.

1.1.2 Photonic crystal fibres

The rebirth of dielectric hollow core waveguides was accompanied by the appearance of hollow core photonic bandgap fibre (HC-PBG) towards the end of the 20th century.

The idea of photonic bandgap (PBG) and the subsequent concept of photonic crystal materials were first proposed by Yablonovitch [16] and John [17] in 1987. A PBG is a frequency gap in the spectrum where an electromagnetic wave is forbidden to propagate in a material or medium. The word “bandgap” is borrowed from

"electronic bandgap" in solid state physics, which originally referred to an energy range in a solid where no propagating electron states can exist.

In 1991, Russell extended the PBG concept to the optical fibre [18]. In 1995 Birks et al. theoretically demonstrated the existence of PBG in a two dimensional silica/air periodic structure [19]. They showed that such a PBG can prevent light from radiating in the plane of periodicity but allows it to propagate out of the plane. Accordingly they suggested a new type of optical fibre independent of TIR based on this structure [19]. In this new fibre, light would be totally confined and transmitted in the core regardless of the refractive index difference between the core and cladding. The first experimental demonstration of light transmission in HC-PBG was reported by Cregan and colleagues in 1999 [13].

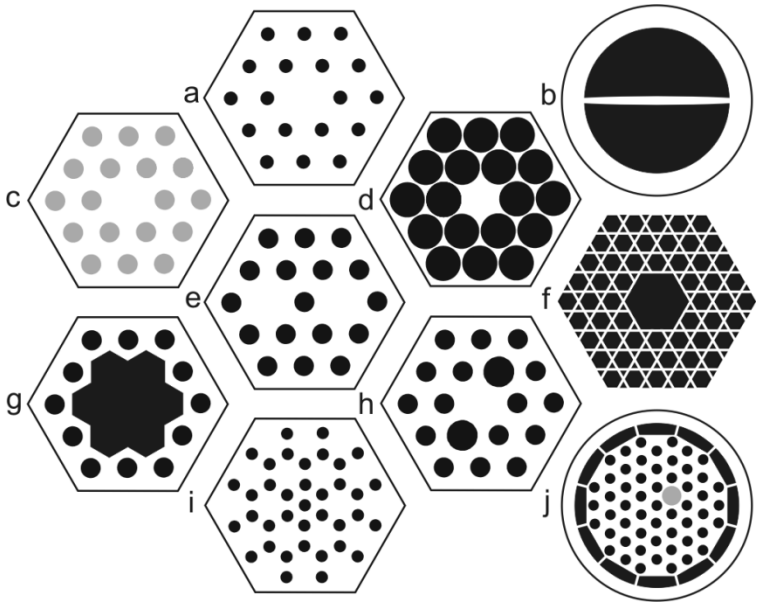

Fig. 1.1 Representative sketches of different types of PCFs (fig1.1 cited from [18]). The black regions are hollow, the white regions are pure glasses, and the gray regions are doped glasses. (a) endless-single-mode solid-core PCF. (b) Nanoweb fibre (not a PCF). (c) All- solid glass PCF with raised-index doped glass strands (colored gray) in the cladding. (d) Supercontinuum PCF (with high air-filling fraction and small core). (e) Dual-core PCF. (f) Kagomé hollow-core PCF. (g) Seven-cell hollow-core PCF. (h) Birefringent PCF. (i) Carbon-ring structure for PBG guidance. (j) Double-clad PCF with offset doped lasing core and high numerical aperture inner cladding for pumping (the photonic-crystal cladding is held in place by thin webs of glass) [18].

The motivation for developing HCF was initially to push the limit of fibre attenuation down to a lower level than the state-of-the-art conventional index guiding fibre. The conventional fibre with a solid doped core has fibre loss fundamentally limited by Rayleigh scattering in the short wavelength range and phonon absorption in the long wavelength range [20]. In HCF, the solid material absorption which

contributes to the transmission loss would be much reduced theoretically since light propagates mainly in the air/vacuum core with extremely small overlap with the solid material in the cladding. Accordingly HCF, in theory, can guide light with loss of several orders of magnitude less than the index guiding fibre [20].

However, further investigations found that the roughness at the air/glass interface of the core boundary, due to the thermal excitation during the fabrication, primarily limits the loss level of HCF [21]. The lowest attenuation obtained in the regular HC-PBG can reach 1.2 dB/km, which is still one order of magnitude higher than commercial single mode fibre [21]. Recently a 37-cell HC-PBG was fabricated with 3.3 dB/km attenuation at 1550 nm. By depressing the interaction between the surface mode and core mode, this fibre exhibited a smooth and flat transmission spectrum [22]. The polarization and wavelength division multiplexed signals over 310 meters of this fibre realized a total data transmission rate of 73.7Tb/s [22].

A major concern about HC-PBG for practical applications is its limited transmission bandwidth which is usually on the scale of tens of nanometers. Such limited bandwidth comes from the nature of PBG guidance. In 2002 a new type of HCF with a Kagome lattice cladding was reported by Benabid and his colleagues [23]. This kind of fibre has a periodic lattice in the cladding but no PBG can be found by simulations or experiments. This fibre apparently guides light and the bandwidth of such guidance can cover a broad frequency range (hundreds of nanometers from the visible to the near infrared spectrum) in the form of multiple transmission bands. Due to its unique cladding lattice, this fibre is named “Kagome” fibre.

As no PBG exists in the cladding, Kagome fibres suffer from a relatively higher loss than index guiding fibres. The attenuation level of Kagome fibre is influenced by the core dimension; usually a smaller attenuation can be measured in a larger core Kagome fibre [24]. Inspired by Kagome fibre, square lattice HCF was also fabricated and demonstrated similar broadband guidance property [25]. By making use of broadband transmission, multi-octave optical frequency combs were successfully realized in hydrogen filled Kagome fibre spanning wavelengths from 325 to 2300 nm [26].

1.1.3 Hollow core negative curvature fibre

1) Development of hollow core negative curvature fibre

Hollow core negative curvature fibre (HC-NCF) is another kind of leaky HCF, which features negative curvature of the core boundary as shown in fig. 1.2.

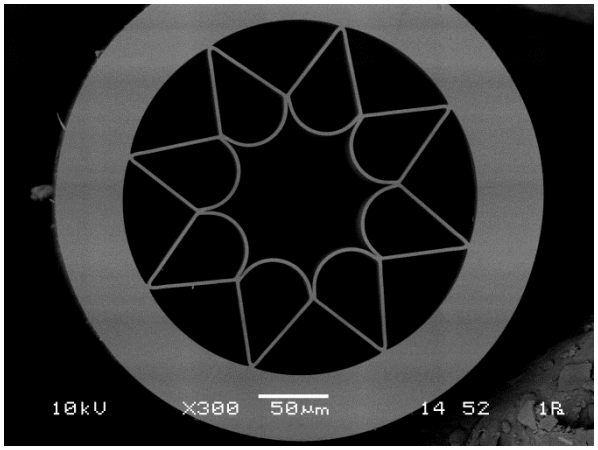

Fig. 1.2 Typical hollow core negative curvature fibre.

The importance of curvature of the core boundary in HCF was firstly discovered in Kagome fibres by Wang et al. in 2010 [27]. A Kagome fibre with negative curvature of the core boundary exhibited an unexpected lower attenuation than regular ones. A series of subsequent experiments confirmed the function of the negative curvature core wall in the reduction of attenuation in Kagome fibres [28].

Later in 2010 Gérôme et al. demonstrated that the complex structure of the cladding has a negligible effect on the confinement loss of Kagome fibre [29]. At the same time, Vincetti and Setti numerically studied HC-NCF with a simplified cladding systematically and revealed that the coupling interaction between the core mode and cladding mode decides the high loss transmission spectral regions of HC-NCF [30].

In 2011, Pryamikov et al. fabricated the first silica HC-NCF without lattice structure in the cladding [31]. They demonstrated that light can be transmitted through a 63 cm length of silica fibre at 3 μm wavelength even though. The fused silica exhibits very high material absorption in this spectral region [32]. Afterwards, Kosolapov et al. extended the transmission window in a similar structured HC-NCF to 10.6 μm for CO_2 laser by using chalcogenide glass instead of silica as the fabrication material [33].

In 2012 during the course of this thesis I designed, fabricated and characterised a silica HC-NCF with low loss transmission in the mid-infrared spectral region from 3 μm to 4 μm, with minimum attenuation of 34 dB/km at a wavelength of 3.05 μm

measured through 83 m of fibre [34]. Transmission of wavelengths beyond 4 μm was also demonstrated [34]. Later, in collaboration with researchers at Heriot-Watt University, we demonstrated the delivery of high energy microsecond pulses at 2.94 μm through the HC-NCF, which could be used for minimally invasive surgical laser procedures [35].

In the same year, Anthony et al. demonstrated THz guidance in HC-NCF made of polymethylmethacrylate [36].

Early in 2013 Kolyadin et al. reported modified silica HC-NCFs with contactless capillary cladding and demonstrated low loss transmission of light in the mid-infrared spectrum range from 2.5 to 7.9 μm [37]. In their work the contactless capillary cladding structure was introduced to reduce the coupling between the core modes and strut modes and measured average attenuations at 5.8 μm and 7.7 μm were 30 dB/m and 50 dB/m respectively.

In May 2013, high average power picosecond and nanosecond pulse delivery at 1030 nm and 1064 nm wavelengths were successfully demonstrated through a silica HC-NCF which I had designed and fabricated for high-precision micro-machining applications [38]. Picosecond pulses with an average power above 36 W and energies of 92 μJ have been transmitted through this HC-NCF without introducing any damage to the fibre structure at the input or output end-faces [38].

In June 2013, we published our results analysing the spectral limits of attenuation of silica HC-NCF in the wavelength range from 800 nm up to 4.5 μm. Our work was based on our measurements of nearly 50 silica HC-NCFs fabricated since 2012 [39]. A minimum attenuation of 24.4 dB/km at around 2400 nm was reported, while 85dB/km was measured at 4000 nm [39].

We recently reported efficient stimulated Raman scattering (SRS) generation at 1.9 μm wavelength by using a 1.06 μm microchip laser to pump a H_2-filled HC-NCF which I had designed and fabricated [40]. Pure vibrational Stokes was obtained in a 6.5 m fiber length and the maximum quantum conversion efficiency was more than 48 % at 23 bar H_2 pressure [40].

2) Summary of my contributions to hollow core negative curvature fibres

My contributions (published) as the first author to the study of HC-NCFs can be summarized as below. Details of these works will be presented in Chapter 5.

1) In 2012, I fabricated my first low loss silica HC-NCF with transmission in the mid-infrared spectrum above 3 μm. I firstly verified the low loss feature of HC-NCF at long wavelength transmission by reliable experimental measurement. Bending loss, mode profile and scaling property of this fibre were also studied [34].

2) In 2013, the silica HC-NCF with the lowest attenuation of 24.4 dB/km at 2400 nm was fabricated and measured [39].

3) By summarizing the attenuation properties of nearly 50 silica HC-NCFs, the spectral limit of attention of HC-NCF was proposed and discussed [39].

The other research works related to HC-NCFs (published) that I have contributed to are summarized below:

1) Delivery of high energy microsecond pulses at 2.94 μm through a silica HC-NCF was successfully demonstrated. This could be used for minimally invasive surgical laser procedures [35].
2) High average power picosecond and nanosecond pulse delivery at 1030 nm and 1064 nm wavelengths were successfully demonstrated through a silica HC-NCF for high-precision micro-machining applications [38].
3) Efficient stimulated Raman scattering generation at the wavelength of 1.9 μm was demonstrated by using a 1.06 μm microchip laser to pump a hydrogen-filled HC-NCF [40].

1.2 Applications of hollow core fibres

1.2.1 Light and gas interaction

One advantage of HCFs is that they can be filled with gas or even liquid and provide a new playground for the study of light–gas interactions. In the free space the interaction between light and gas is limited by the diffraction of light. HCF provides a novel way to overcome this difficulty.

The enhancement of interaction between light and gas can be quantified by the figure of merit (FOM) [23]:

$$\mathrm{FOM} = \frac{\mathrm{l_{eff}}}{\mathrm{A_{eff}}}\lambda \qquad (1-1)$$

in which $\mathrm{l_{eff}}$ is the effective length of interaction region, $\mathrm{A_{eff}}$ is the effective area of light beam and λ is the wavelength.

In the free space, FOM is mainly determined by the laser divergence. In the Gaussian beam, the Rayleigh length at the waist is [41]

$$\mathrm{L} = 2\pi\frac{\mathrm{w}^2}{\lambda} \qquad (1-2)$$

where w is the beam waist radius. Then for Gaussian beam, FOM in the free space is 2.

However in HCFs, eqn. (1-1) can be approximated as [23]

$$\mathrm{FOM} = \frac{\lambda}{\mathrm{A_{core}}\alpha} \qquad (1-3)$$

where α is the fibre loss. For low loss HC-PBG which has core diameter around 10 μm, the FOM can reach nearly 10^6. The light-gas interaction then can be much enhanced by nearly one million times. Such a high efficiency makes HCF an excellent candidate for the study of light-gas interaction.

In 2002 Kagome fibre was used to observe stimulated Raman scattering (SRS) by filling the fibre with hydrogen gas [23]. A frequency-doubled Q-switched Nd:YAG laser at 532 nm was used to pumped a 1 meter long Kagome fibre full of H_2 and a reduced threshold for SRS was observed. In 2004, a much lower threshold power of SRS and nearly 92% Stokes quantum conversion efficiency were reported in a H_2 filled HC-PBG [42]. Those successful demonstrations quickly led a series of studies of

SRS and related gas-light interactions in HCF such as frequency comb generation [43], demonstrations of self-similarity [44], pulse amplification by backward SRS [45], and coherent anti-Stokes Raman scattering [46].

In 2013 an efficient 1.9 μm vibrational SRS generation was reported by using HC-NCF [40]. Pure vibrational Stokes scattering was observed in a 6.5 m long low loss H_2-filled HC-NCF at 23 bars, pumped with a 1064nm microchip laser. A maximum output peak power of 1500 W at 1907 nm was achieved, corresponding to a quantum conversion efficiency above 48 %. This investigation extended the range of stimulated Raman Stokes in gas-filled fibre into the mid-IR wavelengths.

In 2011 population inversion of C_2H_2 gas in Kagome fibre was first realized and observed [47, 48]. This paves the way to gas fibre lasers in the future. The power scaling of conventional index guiding fibre lasers is usually constrained by detrimental nonlinear optical processes and, ultimately, material damage in the solid core gain medium [49]. Compared with conventional solid fibre laser, gas fibre lasers greatly reduce the nonlinear and absorption effects between the light and solid material so that the gas fibre laser can reach a much higher optical power without damaging the fibre in theory. Such lasers can also realize a broad spectral range of emission, from the UV to the IR, which depends on the active gas atoms or molecules and the transmission window of the fibre. Owing to the nature of atomic and molecular gas transitions the gas fibre laser always presents a much narrower laser spectral bandwidth than the solid fibre lasers. Also thermal effects [49] such as thermal lensing under high power operation may be finally conquered in gas fibre lasers.

Recently the study of nonlinear optics in gas-filled HCF has been attracting more and more attention [51]. By filling HCF with noble gases or other gases like nitrogen, novel ultrafast nonlinear optical phenomena were observed under extremely high input ultrafast laser pulse, including deep-UV generation [52], plasma generation and related soliton blueshift [53] and high harmonic generation [54]. Those studies have broadened the area of nonlinear optics and enrich the study of light-gas interaction.

1.2.2 High power laser delivery

High power handling capability was one of the initial motivations to fabricate and study low loss HCFs. Since the appearance of low loss metal hollow core waveguide, the guidance of light in an air/vacuum core has been demonstrated as a successful method to transmit high power laser light [6]. In comparison with index guiding

fibres, HCF can sustain a much higher peak power. Because of the small overlap between the light field and cladding material, both material absorption and nonlinear optical phenomena can be much reduced. Also, since there are no Fresnel reflections at the fibre ends, a high coupling efficiency between the laser source and HCF is possible to achieve in theory [55].

Before the appearance of HC-PBG, the inner surface dielectric/metal coated hollow core waveguides were broadly used in high power laser delivery at mid-infrared wavelengths up to 20 μm [9]. Transmission of a continuous-wave CO_2 laser power as high as 2.7 kW was demonstrated in the metal hollow core waveguide in 1992 [11]. However, in those metal hollow core waveguides, high bending loss and degradation of output beam quality due to multimode transmission constrains the performance because of their large core areas [7, 10, 11, 56].

Since the appearance of HC-PBG and novel HCFs, they have been investigated for high power laser pulse transmission. Bragg fibre [57], HC-PBG [58 - 60] and Kagome fibres [61] have all been demonstrated successfully in high power laser transmission at traditional laser lines locating in the near infrared spectral range. Among them HC-PBG can offer almost a pure single mode guidance with a much lower bending loss in comparison with other HCFs [59-60]. These advantages bring flexibility and accessibility in practical applications such as laser surgery [62] and laser machining [59].

Besides many traditional laser wavelengths, in the spectrum from 2 μm to 25 μm, HCFs are playing a more and more important role for laser transmission. The mid-infrared spectral region is usually characterized by the strong vibrational absorption lines of molecules, and is known as the ‘molecular fingerprint’ region [63]. Material absorption has always been one of the limitations on conventional index guiding fibre performance in the mid-IR. Fused silica, the most common optical fibre material, exhibits extraordinary mechanical and chemical durability but is limited by its high attenuation (above 60 dB/m) at wavelengths longer than 3 μm [32, 64]. Soft glasses, such as chalcogenides and fluorides, which possess a much lower absorption, have been widely adopted as optical fibre materials for the mid-IR [65]. However, compared with the mature state of silica fabrication, the processing routes for purification and fibre drawing still need much improvement to achieve the theoretical performance expected for many of these materials [66]. With the emergence of new

generations of mid-IR laser sources, there is increasing interest in this spectral window for applications in spectroscopy and medicine [63, 66, 67].

The first HC-PBG made of silica glass for mid-IR transmission was first reported in 2005 with attenuation of 2.6 dB/m between 3100 nm and 3200 nm and extremely low bending loss [62]. A modified HC-PBG for 3 μm transmission was reported later with attenuation less than 1 dB/m later [69]. A Kagome fibre, which was used to assemble an acetylene gas fibre laser for mid-IR laser generation, was reported to guide pump light at 1521 nm and two laser lines at 3123.2 nm and 3162.4 nm at the same time [48], although the attenuation was high (more than 20 dB/m) above 3 μm.

HC-NCF, which was initially fabricated for mid-infrared light transmission, exhibits great flexibility and low loss features for laser delivery [31, 32, 33, 37, 38]. In 2011 Pryamikov et al. first reported transmission beyond 3 μm wavelength through a 63 cm long HC-NCF [31]. Later CO_2 laser transmission at 10.6 μm was successfully demonstrated by a HC-NCF made of chalcogenide glass [20]. The delivery of high energy microsecond pulses at 2.94 μm was successfully demonstrated through a silica HC-NCF which could be used for minimally invasive surgical laser procedures [35]. 2.94 μm laser pulses with energies up to 195 mJ at a pulse length of 225 μs were delivered in HC-NCF [35]. In 2013 Kolyadin et al. proved a new design of silica HC-NCF which can transmit light in the mid-infrared spectrum range from 2.5 to 7.9 μm [37].

Picosecond and nanosecond pulse delivery at 1030 nm and 1064 nm wavelengths were also demonstrated successfully through a silica HC-NCF [38]. Picosecond pulses with an average power above 36 W and energies of 92 μJ was delivered in HC-PCF with an average power 7 times bigger than the previously reported record in a hypocycloid-core Kagome-type HC-PCF [38]. No optical damage to the HC-NCF was found in the nanosecond pulse delivery and the fibre was expect to be capable of delivering at least 8 mJ in a 60 ns pulse before damage [38].

1.2.3 Ultrafast laser pulse delivery

Ultrafast (femtosecond) laser pulses have much broader spectra in comparison with the usual nanosecond duration Q-switched laser pulses [41]. The transmission of ultrafast pulses through meter-scale lengths of optical fibre is of great interest for many applications, such as materials processing, imaging applications and spectroscopy. However, in conventional index guiding fibres, the ultrafast pulses

would be quickly torn apart because of dispersion in the broad spectrum, and at the meantime the high field intensity also leads to rapid nonlinear spectral broadening by the material e.g. self-phase modulations and Raman scattering [2]. As a result, in conventional index guiding fibres, an ultrafast laser pulse cannot propagate even through a few centimetres without significant distortion. When increasing pulse energy, optical damage is almost unavoidable at the fibre ends and inside the fibre. Those limits are inevitably imposed by the solid material in the core. As a result, almost since the first appearance of low loss HCFs, researchers have been exploring the application of HCFs to the ultrafast laser pulse delivery.

The first demonstration of ultrafast laser pulse delivery in HC-PBG was reported in 2003 [69]. Megawatt femtosecond soliton propagated over 3m of HC-PBG at the wavelength of 1550nm.

Solitons are formed due to the balance between anomalous group velocity dispersion (GVD) and self-phase modulation (SPM) [70]. The duration τ_0 of the soliton in the fibre is given by [70]:

$$\tau_0 = 1.76\frac{\lambda^3 D A_{eff}}{2\pi^2 c n_2 E_{sol}} \qquad (1-4)$$

where λ is the central wavelength of the soliton, D is the GVD, n_2 is the nonlinear refractive index coefficient of the core material, A_{eff} is the nonlinear effective area of guided mode in fibre, c is the speed of light and E_{sol} is the soliton energy.

The SPM effect is characterized by n_2 and n_2 in air is roughly three orders of magnitude less than in silica [69]. In HC-PBG, the nonlinear response is thus substantially reduced compared with conventional fibres, so HC-PBG can sustain a much higher power of ultrafast laser soliton pulse in the transmission according to eqn. (1-4).

According to eqn. (1-4), as we increase the soliton energy, the pulse width is decreased accordingly. Higher-order solitons can also form from the fundamental solitons as the soliton energy is increased [70]. This evolution results in a change of the temporal shape and spectrum of the pulse. The pulse undergoes significant compression which depends on the soliton order [70]. The compression of ultrafast pulses based on the soliton dynamics is a well-known technique in optical fibres [70,

71]. With an appropriate choice of fibre length, the output pulse can be significantly shorter than the input [71].

In 2004, Luan et al. demonstrated transmission of Titanium-Sapphire ultrafast laser pulses at 800nm wavelength over 5 meters of HC-PBG [72]. Physically, when the spectral width of ultrafast pulses exceeds a few terahertz, the high frequency components of the pulse will pump the low frequency components within the same pulse which is named the intrapulse stimulated Raman scattering effect (ISRS) [70]. ISRS results in a gradual shift of the pulse spectrum toward longer wavelengths as the pulse propagates. Due to the limited transmission window of HC-PBG, the soliton compression stops until the redshift of soliton frequency reaches the transmission band edge of HC-PBG.

To further reduce the soliton self-frequency shift arising from the Raman response of the air core, xenon, as a non-Raman-active gas, was used to fill the HC-PBG. In this way compressed pulse lengths as short as 50fs after a 24cm long propagation with a pulse compression ratio of 2.4 were achieved [73].

In 2007 a tapered HC-PBG successfully compressed unchirped 195fs input pulses at 800 nm wavelength to less than 100fs after single-mode propagation through 8m length, with pulse energies around 50nJ [74]. Soliton compression in a dispersion decreasing fibre was firstly proposed by Tajima in 1987 [75]. As eqn. (1-4) implies, the fundamental soliton can be effectively compressed when D is decreased. It would require that the transvers dimension of fibre is tapered in the direction of soliton propagation. Gérôme and his colleagues applied fibre tapering technique to HC-PBG and demonstrated success [74]. The tapered HC-PBG did not only realize the dispersion decreasing along the length but also shifted the transmission spectral window in accordance with soliton self-frequency shift due to ISRS.

In 2010, the delivery of the ultrafast laser pulse at an even shorter wavelength was demonstrated in HC-PBG [76]. The central wavelength of the transmission window of HC-PBG is determined by the periodicity of the cladding structure. HC-PBG for smaller wavelength transmission suffers from the fabrication difficulty caused by surface tension. In the fabrication, it becomes very difficult to prevent deformation of the cladding structure in a small HC-PBG. This deformation usually comes along with extremely high loss. Therefore the minimum wavelength of ultrafast pulses delivered in HC-PBG had been limited to Ti:sapphire laser wavelengths at around 800 nm. With

Mosley and his colleagues' efforts, sub-picosecond pulses in the green spectral region around 532 nm was launched into 1 m of HC-PBG of low loss, and they achieved temporal compression by up to a factor of 3 [76]. The pulse duration after compression can reach around 100 fs [76].

1.3 Conclusions

Chapter 1 briefly introduces the development of HCFs and their applications.

Before the appearance of HC-PBG in the 1990's, hollow core waveguides with inner surface dielectric/metal coatings were used in labs and industries, and had achieved success in laser transmission at long wavelengths. Since the concept of photonic bandgap was raised, numerous hollow core optical fibres, were fabricated and studied. Those novel HCFs greatly enriched the research field of fibre optics. More recently, HC-NCF, which exhibits multiband transmission and low attenuation features, has been attracting researchers' interests.

HCFs have been successfully applied in many fields due to their unique optical characteristics. Light-gas interaction, high power laser delivery and ultrafast laser pulse delivery were three main applications introduced in this chapter. HC-NCFs have also demonstrated high power laser delivery at 2.94 μm and 1.064 μm.

Reference

[1] J. Hetch, City of light: the story of fiber optics, Chapter 2 (Oxford university press, 1999).

[2] G. P. Agrawa, Nonlinear fibre optics 4th edition, Chapter 1 (Elsevier, 2009).

[3] A. Méndez and T.F. Morse, Specialty optical fibre handbook, Chapter 10 (Elsevier, 2007).

[4] T. Miya, Y .Terunuma; T. Hosaka; and T. Miyashita, "Ultimate low-loss single-mode fibre at 1.55 um,", Electron. lett., **15**, 106 (1979).

[5] J. R. Carson, S. P. Mead, and S.A. Schelkunoff, "Hyper-Frequency Wave Guides---Mathematical Theory," Bell System Techn. J. **15**, 310-333 (1936).

[6] R. E. Collin, Field theory of guided waves 2nd edition(Wiley-IEEE Press, 1990)

[7] D. A. Alsberg, J.C. Bankert, and P.T. Hutchison, "The WT4/WT4A millimeter-wave transmission system," Bell System Techn. J. **56**, 1829 (1977).

[8] E. Garmire, T. McMahon and M. Bass, "Flexible infrared waveguides for high-power transmission," J. Quantum Electron. **16**, 23-32 (1980).

[9] J. Harrington, "A review of IR transmitting, hollow waveguides," Fiber Integr. Opt. **19**, 211-227 (2000).

[10] H. Machida, Y. Matsuura, H. Ishikawa, and M. Miyagi, "Transmission properties of rectangular hollow waveguides for CO laser light," Appl. Opt. **31**,7617-7622 (1992).

[11] A. Hongo, K. Morosawa, K. Matsumoto, T. Shiota, and T. Hashimoto, "Transmission of kilowatt-class CO2 laser light through dielectric-coated metallic hollow waveguides for material processing," Appl. Opt. 31, 5114-5120 (1992).

[12] E. A. J. Marcatili and R. A. Schmeltzer, "Hollow metallic and dielectric waveguides for long distance optical transmission and lasers," Bell Syst. Tech. J. **43**, 1783–1809 (1964).

[13] R. F. Cregan, B. J. Mangan, J. C. Knight, T. A. Birks, P. St. J. Russell1, P. J. Roberts and D. C. Allan, "Single-mode photonic band gap guidance of light in air," Science **285**, 1537-1539 (1999).

[14] A. Méndez and T.F. Morse, Specialty optical fibre handbook, Chapter 3 (Elsevier, 2007).

[15]Corning website: http://www.corning.com/opticalfiber/products/SMF-28_ULL_fiber.aspx

[16] E. Yablonovitch, "Inhibited Spontaneous Emission in Solid-State Physics and Electronics," Phys. Rev. Lett. **58**, 2059-2062 (1987).

[17] S. John, "Strong Localization of Photons in Certain Disordered Dielectric Superlattices," Phys. Rev. Lett. **58**, 2486-2489 (1987).

[18] P. St. J. Russell, "Photonic-Crystal Fibers," J. Lightwave Technol. **24**, 4729-4749 (2006).

[19] T. A. Birks, P. J. Roberts, P. St. J. Russell and D. M. Atkin, "Full 2-D Photonic Bandgaps in Silica/Air Structures," Electron. Lett. **31**, 1941-1943 (1995).

[20] M. Ohashi, K. Shiraki and K. Tajima, "Optical Loss Property of Silica-Based Single-Mode Fibers", J. of Lighwave Tech **10**, 539 (1992).

[21] P. J. Roberts, F. Couny, H. Sabert, B. J. Mangan, D. P. Williams, L. Farr, M. W. Mason, A. Tomlinson, T. A. Birks, J. C. Knight, and P. St. J. Russell, "Ultimate low loss of hollow-core photonic crystal fibres," Opt. Express **13**, 236-244 (2005).

[22] Y. Jung, V. Sleiffer, N. Baddela, M. Petrovich, J. R. Hayes, N. Wheeler, D. Gray, E. R. Numkam Fokoua, J. Wooler, N. Wong, F. Parmigiani, S. Alam, J. Surof, M. Kuschnerov, V. Veljanovski, H. Waardt, de, F. Poletti, and D. J. Richardson, "First Demonstration of a Broadband 37-cell Hollow Core Photonic Bandgap Fiber and Its Application to High Capacity Mode Division Multiplexing," in Optical Fiber Communication Conference/National Fiber Optic Engineers Conference 2013, OSA Technical Digest (online) (Optical Society of America, 2013), paper PDP5A.3.

[23] F. Benabid, J. C. Knight, G. Antonopoulos and P. St. J. Russell, "Stimulated Raman scattering in hydrogen-filled hollow-core photonic crystal fiber," Science **298**, 399-402 (2002).

[24] F. Couny, F. Benabid and P. S. Light, "Large-pitch kagome-structured hollow-core photonic crystal fiber," Opt. Lett. **31**, 3574-3576 (2006).

[25] F. Couny, P. J. Roberts, T. A. Birks, and F. Benabid, "Square-lattice large-pitch hollow-core photonic crystal fiber," Opt. Express **16**, 20626-20636 (2008).

[26] F. Couny, F. Benabid, P. J. Roberts, P. S. Light, and M. G. Raymer, "Generation and photonic guidance of multi-octave optical-frequency combs," Science **318**, 1118-1121 (2007).

[27] Y. Wang, F. Couny, P. J. Roberts, and F. Benabid, "Low loss broadband transmission in optimized core – shaped Kagome Hollow Core PCF," in Conference on Lasers and Electro-Optics/Quantum Electronics and Laser Science, Postdeadline Papers (Optical Society of America, Washington, D.C., 2010), paper CPDB4.

[28] Y. Y. Wang, N. V. Wheeler, F. Couny, P. J. Roberts, and F. Benabid, "Low loss broadband transmission in hypocycloid-core Kagome hollow-core photonic crystal fiber," Opt. Lett. **36**, 669-671 (2011).

[29] F. Gérôme, R.Jamier, J. Auguste, G. Humbert, and J. Blondy, "Simplified hollow-core photonic crystal fiber," Opt. Lett. **35**, 1157-1159 (2010).

[30] L. Vincetti and V. Setti, "Waveguiding mechanism in tube lattice fibers," Opt. Express **18**, 23133-23146 (2010).

[31] A. D. Pryamikov, A. S. Biriukov, A. F. Kosolapov, V. G. Plotnichenko, S. L. Semjonov, and E. M. Dianov, "Demonstration of a waveguide regime for a silica hollow-core microstructured optical fiber with a negative curvature of the core boundary in the spectral region > 3.5 μm," Opt. Express **19**, 1441-1448 (2011).

[32] R. Kitamura, L. Pilon, and M. Jonasz, "Optical constants of silica glass from extreme ultraviolet to far infrared at near room temperature," Appl. Opt. **46**, 8118-8133 (2007).

[33] A. F. Kosolapov, A. D. Pryamikov, A. S. Biriukov, V. S. Shiryaev, M. S. Astapovich, G. E. Snopatin, V. G. Plotnichenko, M. F. Churbanov, and E. M. Dianov, "Demonstration of

CO2-laser power delivery through chalcogenide-glass fiber with negative-curvature hollow core," Opt. Express **19**, 25723-25728 (2011).

[34] F. Yu, W. J. Wadsworth, and J. C. Knight, "Low loss silica hollow core fibers for 3–4 μm spectral region," Opt. Express **20**, 11153-11158 (2012).

[35] A. Urich, R. R. J. Maier, F. Yu, J. C. Knight, D. P. Hand, and J. D. Shephard, "Flexible delivery of Er:YAG radiation at 2.94 μm with negative curvature silica glass fibers: a new solution for minimally invasive surgical procedures," Biomed. Opt. Express **4**, 193–205 (2013).

[36] J. Anthony, R. Leonhardt, S. G. Leon-Saval, and A. Argyros, "THz propagation in kagome hollow-core microstructured fibers," Opt. Express **19**, 18470–18478 (2011).

[37] A. N. Kolyadin, A. F. Kosolapov, A. D. Pryamikov, A. S. Biriukov, V. G. Plotnichenko, and E. M. Dianov, "Light transmission in negative curvature hollow core fiber in extremely high material loss region," Opt. Express **21**, 9514-9519 (2013).

[38] P. Jaworski, F. Yu, R. R.J. Maier, W. J. Wadsworth, J. C. Knight, J. D. Shephard, and D. P. Hand, "Picosecond and nanosecond pulse delivery through a hollow-core Negative Curvature Fiber for micro-machining applications," Opt. Express **21**, 22742-22753 (2013).

[39] F. Yu and J. C. Knight, "Spectral attenuation limits of silica hollow core negative curvature fiber," Opt. Express **21**, 21466-21471 (2013).

[40] Z. Wang, F. Yu, W. Wadsworth, and J. Knight, "Efficient 1.9 μm wavelength conversion by stimulated Raman scattering in H2-filled hollow core fiber pumped with 1.06 μm microchip laser," Opt. Express (submitted).

[41] A. E. Siegman, Lasers (University Science Books, 1990).

[42] F. Benabid, G. Bouwmans, J. C. Knight, P. St. J. Russell, and F. Couny, "Ultrahigh efficiency laser wavelength conversion in a gas-filled hollow core photonic crystal fiber by pure stimulated rotational Raman scattering in molecular hydrogen," Phys. Rev. Lett. **93**, 123903 (2004).

[43] F. Couny, F. Benabid, P. J. Roberts, P. S. Light, and M. G. Raymer, "Generation and photonic guidance of multi-octave optical-frequency combs," Science **318**, 1118–1121 (2007).

[44] A. Nazarkin, A. Abdolvand, A. V. Chugreev, and P. St. J. Russell, "Direct observation of self-similarity in evolution of transient stimulated Raman scattering in gas-filled photonic crystal fibers," Phys. Rev. Lett. **105**, 173902 (2010).

[45] A. Abdolvand, A. Nazarkin, A. V. Chugreev, C. F. Kaminski, and P. St. J. Russell, "Solitary pulse generation by backward Raman scattering in H2-filled photonic crystal fibers," Phys. Rev. Lett. **103**, 183902 (2009).

[46] A. B. Fedotov, S. O. Konorov, V. P. Mitrokhin, E. E. Serebryannikov, and A. M. Zheltikov, "Coherent anti-Stokes Raman scattering in isolated air-guided modes of a hollow-core photonic-crystal fiber," Phys. Rev. A **70**, 045802 (2004).

[47] A. M. Jones, A. V. V. Nampoothiri, A. Ratanavis, T. Fiedler, N. V. Wheeler, F. Couny, R. Kadel, F. Benabid, B. R. Washburn, K. L. Corwin, and W. Rudolph, "Mid-infrared gas filled photonic crystal fiber laser based on population inversion," Opt. Express **19,** 2309–2316 (2011).

[48] A. V. V. Nampoothiri, A. M. Jones, A. Ratanavis, R. Kadel, N. V. Wheeler, F. Couny, F. Benabid, B. R. Washburn, K. L. Corwin, and W. Rudolph, "Mid-IR laser emission form a C_2H_2 gas filled hollow core photonic crystal fiber," Proc. SPIE **7580**, 758001 (2010).

[49] D. J. Richardson, J. Nilsson, and W. A. Clarkson, "High power fiber lasers: current status and future perspectives," J. Opt. Soc. Am. B **27**, B63–B92 (2010).

[50] A. V. Vasudevan Nampoothiri, Andrew M. Jones, C. Fourcade-Dutin, Chenchen Mao, Neda Dadashzadeh, Bastian Baumgart, Y.Y. Wang, M. Alharbi, T. Bradley, Neil Campbell, F. Benabid, Brian R. Washburn, Kristan L. Corwin, and Wolfgang Rudolph, "Hollow-core Optical Fiber Gas Lasers (HOFGLAS): a review [Invited]," Opt. Mater. Express **2**, 948-961 (2012)

[51] J. C. Travers, W. Chang, J. Nold, N. Y. Joly, and P. St. J. Russell, "Ultrafast nonlinear optics in gas-filled hollow-core photonic crystal fibers [Invited]," J. Opt. Soc. Am. B **28**, A11-A26 (2011).

[52] N. Y. Joly, J. Nold,W. Chang, P. Hölzer, A. Nazarkin, G. K. L. Wong, F. Biancalana, and P. St. J. Russell, "Bright spatially coherent wavelength-tunable deep-UV laser source using an ar-filled photonic crystal fiber," Phys. Rev. Lett. **106**, 203901 (2011).

[53] P. Hölzer, W. Chang, J. C. Travers, A. Nazarkin, J. Nold, N. Y. Joly, M. Saleh, F. Biancalana, and P. St. J. Russell, "Femtosecond nonlinear fiber optics in the ionization regime," Phys. Rev. Lett. **107**, 203901 (2011).

[54] O. H. Heckl, C. R. E. Baer, C. Kränkel, S. V. Marchese, F. Schapper, M. Holler, T. Südmeyer,J. S. Robinson, J. W. G. Tisch, F. Couny, P. Light, F. Benabid, and U. Keller, "High harmonic generation in a gas-filled hollow-core photonic crystal fiber," Appl. Phys. B **97**, 369–373 (2009).

[55] C. J. Hensley, M. A. Foster, B. Shim, and A. L. Gaeta, "Extremely High Coupling and Transmission of High-Powered-Femtosecond Pulses in Hollow-Core Photonic Band-Gap Fiber," in 2008 Conference on Lasers and Electro-Optics & Quantum Electronics and Laser Science Conference, Vols 1–9 (Ieee, New York, 2008), pp. 2010–2011.

[56] J. P. Parry, T. J. Stephens, J. D. Shephard, J. D. C. Jones, and D. P. Hand, "Analysis of optical damage mechanisms in hollow-core waveguides delivering nanosecond pulses from a Q-switched Nd:YAG laser," Appl. Opt. **45**, 9160–9167 (2006).

[57] B. F. Bowden and J. A. Harrington, "Fabrication and characterization of chalcogenide glass for hollow Bragg fibers," Appl. Opt. 48(16), 3050–3054 (2009).

[58] G. Humbert, J. C. Knight, G. Bouwmans, P. St.J. Russell, D. P.Williams, P. J. Roberts, and B. J. Mangan, "Hollow core photonic crystal fibers for beam delivery," Opt. Express **12**, 1477–1484 (2004).

[59] J. D. Shephard, J. D. C. Jones, D. P. Hand, G. Bouwmans, J. C. Knight, P. S. Russell, and B. J. Mangan, "High energy nanosecond laser pulses delivered single-mode through hollow-core PBG fibers," Opt. Express **12**, 717–723 (2004).

[60] J. D. Shephard, F. Couny, P. S. Russell, J. D. C. Jones, J. C. Knight, and D. P. Hand, "Improved hollow-core photonic crystal fiber design for delivery of nanosecond pulses in laser micromachining applications," Appl. Opt. **44**, 4582–4588 (2005).

[61] B. Beaudou, F. Gerôme, Y. Y. Wang, M. Alharbi, T. D. Bradley, G. Humbert, J.-L. Auguste, J.-M. Blondy, and F. Benabid, "Millijoule laser pulse delivery for spark ignition through kagome hollow-core fiber," Opt. Lett. **37**, 1430-1432 (2012)

[62] J. D. Shephard, W. N. Macpherson, R. R. J. Maier, J. D. C. Jones, D. P. Hand, M. Mohebbi, A. K. George, P. J. Roberts, and J. C. Knight, "Single-mode mid-IR guidance in a hollow-core photonic crystal fiber," Opt. Express **13**, 7139–7144 (2005).

[63] F. K. Tittel, D. Richter, and A. Fried, "Mid-infrared laser applications in spectroscopy," in Solid-state mid-infrared laser sources, I.T. Sorokina and K.L. Vodopyanov, ed. (Springer, Berlin, 2003).

[64] O. Humbach, H. Fabian , U. Grzesik, U. Haken, and W. Heitmann, "Analysis of OH absorption bands in synthetic silica," J. Non-Cryst. Solids **203**, 19-26 (1996).

[65] J. S. Sanghera, L. B. Shaw, and I. D. Aggarwal, "Applications of chalcogenide glass optical fibers," C. R. Chimie. **5**, 873-883 (2002).

[66] B. Jean and T. Bende, "Mid-IR laser applications in medicine," in Solid-state mid-infrared laser sources, I.T. Sorokina and K.L. Vodopyanov, ed. (Springer, Berlin, 2003).

[67] B. Gaspirc and U. Skaleric, "Clinical evaluation of periodontal surgical treatment with an Er : YAG laser: 5-year results," J. Periodontol. **78**, 1864-1871(2007).

[68] N. Gayraud, L. W. Kornaszewski, J. M. Stone, J. C. Knight, D. T. Reid, D. P. Hand, and W. N. MacPherson, "Mid infra-red gas sensing using a hollow-core photonic bandgap fiber," Optical Fiber Sensors (OFS) 2006 paper ThA5 (2006).

[69] D. G. Ouzounov, F.R.Ahmad , D.Muller ,N. Venkataraman, M.T. Gallagher , M.G.Thomas, J. Silcox , K.W. Koch, A.L.Gaeta, "Generation of Megawatt Optical Solitons in Hollow-Core Photonic Band-Gap Fibers," Science **301**, 1702-1704 (2003).

[70] G. P. Agrawa, Nonlinear fibre optics 4th edition, Chapter 5 (Elsevier, 2009).

[71] L. F. Mollenauer, R. H. Stolen, J. P. Gordon, and W. J. Tomlinson, "Extreme picosecond pulse narrowing by means of soliton effect in single-mode optical fibers," Opt. Lett. 8, 289–291 (1983).

[72] F. Luan, J. Knight, P. Russell, S. Campbell, D. Xiao, D. Reid, B. Mangan, D. Williams, and P. Roberts, "Femtosecond soliton pulse delivery at 800nm wavelength in hollow-core photonic bandgap fibers," Opt. Express **12**, 835-840 (2004)

[73] D. G. Ouzounov, C. J. Hensley and A.L. Gaeta, "Soliton pulse compression in photonic band-gap fibers," Opt. Express **13**, 6153-6159 (2005).

[74] F. Gérôme, K. Cook, A. K. George, W. J. Wadsworth, and J. C. Knight, "Delivery of sub-100fs pulses through 8m of hollow-core fiber using soliton compression," Opt. Express **15**, 7126-7131 (2007).

[75] K. Tajima, "Compensation of soliton broadening in nonlinear optical fibers with loss," Opt. Lett. 12, 54-56 (1987).

[76] P. J. Mosley, W. C. Huang, M. G. Welch, B. J. Mangan, W. J. Wadsworth, and J. C. Knight, "Ultrashort pulse compression and delivery in a hollow-core photonic crystal fiber at 540 nm wavelength," Opt. Lett. **35**, 3589-3591 (2010).

Chapter 2 Background of leaky hollow core fibre theory

Chapter 2 introduces the background theory of leaky HCF which is important to help us understanding light transmission in HC-NCF.

In section 2.1, the mode theory of leaky HCF is discussed. Mode theory, which has achieved great success in index guiding fibres, faces challenges in modelling leaky HCF and is still developing.

Section 2.2 introduces other models of leaky HCFs, which are Marcatili and Schmeltzer's formula [5], the ARROW model [6, 7] and the cladding mode coupling model [8].

Section 2.3 briefly discusses the role of the negative curvature core boundary in HCF. Although the negative curvature core wall has been demonstrated as effective in reducing attenuation of HCF, the theoretical model has not been fully established yet. In this section, the function of the negative curvature core wall is analysed in term of depressing coupling between the core and cladding modes.

In section 2.4, the scaling law of Maxwell equations is introduced. Based on this law, the transmission window of HCF can be shifted by scaling the dimension of HCF during the fabrication.

2.1 Mode theory for leaky hollow core fibre

2.1.1 Framework of mode theory for conventional fibre

Mode theory has been demonstrated great success in the study of optical waveguides and forms our basis of understanding light propagation in the index guiding optical waveguides [1].

In mathematics, mode theory essentially grows up from solving the simplified Helmholtz equation, under certain boundary conditions [1].

In conventional optical waveguides where the core material has a refractive index higher than the cladding, light can be totally confined in the core due to TIR under certain conditions. In an ideal optical waveguide, which is assumed to be uniform along the longitudinal direction **z** and has no scattering or material absorption, light can be transmitted without any loss. According to the translation symmetry of the optical waveguide in the **z** direction, the mode field in the optical waveguide can be express as

$$\mathbf{E}(x,y,z) = \mathbf{e}(x,y)\exp(i\beta z); \mathbf{H}(x,y,z) = \mathbf{h}(x,y)\exp(i\beta z) \qquad (2-1)$$

Here, β is the propagation constant and is real. Helmholtz's equation is simplified as below [1]

$$(\nabla_t^2 + n^2k^2 - \beta^2)\mathbf{e} = -(\boldsymbol{\nabla}_t + i\beta\mathbf{z})\mathbf{e}_t \cdot \boldsymbol{\nabla}_t \ln(n^2) \qquad (2-2)$$

$$(\nabla_t^2 + n^2k^2 - \beta^2)\mathbf{h} = \{(\boldsymbol{\nabla}_t + i\beta\mathbf{z}) \times \mathbf{h}_t\} \times \boldsymbol{\nabla}_t \ln(n^2) \qquad (2-3)$$

where $k = \frac{2\pi}{\lambda}$ and λ is the free space wavelength, and $n = n(x,y)$ describes the spatial distribution of refractive index of the optical waveguide. Usually n is a piecewise constant function and is discontinuous only at the material boundaries. In this case, the right hand sides of eqn. (2-2) and eqn. (2-3) can be ignored in most areas of a waveguide.

In cylindrical coordinates, the transverse and longitudinal components of the field are tangled in a complex way [1]:

$$\mathbf{e}_t = \frac{i}{n^2k^2 - \beta^2}\left\{\beta\boldsymbol{\nabla}_t e_z - \left(\frac{\mu_0}{\varepsilon_0}\right)^{1/2} k\mathbf{z} \times \boldsymbol{\nabla}_t h_z\right\} \qquad (2-4)$$

$$\mathbf{h}_t = \frac{i}{n^2k^2 - \beta^2}\left\{\beta\boldsymbol{\nabla}_t h_z + \left(\frac{\mu_0}{\varepsilon_0}\right)^{1/2} kn^2\mathbf{z} \times \boldsymbol{\nabla}_t e_z\right\} \qquad (2-5)$$

The **z** component of the field simply satisfies

$$\left(\partial_r^2 + r^{-1}\partial_r + r^{-2}\partial_\phi^2 + U^2\right)\Psi = 0 \qquad (2-6)$$

where $\Psi = e_z$ or h_z, $U^2 = (n^2k^2 - \beta^2)$. By applying $\Psi = \psi(r)\theta(\phi)$, the partial differential eqn (2-6) is solved by

$$(d_r^2 + r^{-1}d_r + U^2 - m^2r^{-2})\psi(r) = 0 \qquad (2-7)$$

$$\left(d_\phi^2 - m^2\right)\theta(\phi) = 0 \qquad (2-8)$$

In a circularly symmetric optical waveguide, m must be integer by symmetry.

Equation (2.7) is Bessel equation or modified Bessel equation which is determined by the sign of U^2 [2]. By applying boundary conditions, β can be obtained from solving the eigenvalue equation [1].

As shown above, the framework of mode theory is mathematically established on solving the Bessel equation, a singular Sturm-Liouville boundary value problem [2].

2.1.2 Challenges from leaky HCF

In leaky HCF, the physics behind light transmission cannot be explained by TIR as the light is transmitted in the core of lower refractive index. Except of HC-PBG with photonic bandgap in the cladding, loss is an inherent feature of transmission inside leaky HCFs. The mode theory which was established on the model of index guiding must be modified accordingly in order to apply to HCFs. This modification faces many challenges and is still under development.

1) Complex β and complex Bessel functions

In HCF, the translation symmetry along the **z** direction is still valid but because of unavoidable leakage loss, β becomes complex,

$$\beta = \beta_r + i\alpha \qquad (2-9)$$

where β_r and α are both real. After normalization we transform eqn. (2-7) into a standard form of Bessel equation

$$\left(d_R^2 + R^{-1}d_R + 1 - m^2R^{-2}\right)\psi(R) = 0 \qquad (2-10)$$

where $R^2 = r^2U^2$. As β is complex, the solution of the Bessel equation moves to the complex domain.

In conventional mode theory, solutions of eqn. (2-7) are Bessel function of the first kind $J_m(R)$ and modified Bessel function of the second kind $K_m(iR)$, which describe the modal fields along the radial direction in the core and cladding regions respectively [1, 3].

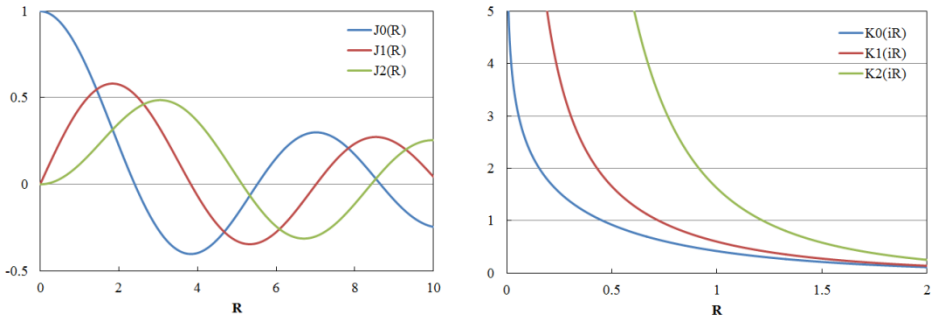

Fig. 2.1 Left: Bessel function of the first kind for real R and integer order $m = 0, 1, 2$; right: modified Bessel function of the second kind for real R and integer order $m = 0, 1, 2$.

In the core region, $U^2 > 0$, R and $J_m(R)$ are real. $J_m(R)$ oscillates and gradually decays as R increases when m is positive integer. In the cladding, $U^2 < 0$ and iR is pure imaginary. $K_m(iR)$ is real along the imaginary axis and exponentially decays as R increases. In cylindrical coordinates, $J_m(R)$ represents standing wave in the core while $K_m(iR)$ describes the evanescent field in the cladding.

In the leaky HCF, the failure of TIR results in inherent loss of modes, which brings an imaginary part in the propagation constant β. In the mode theory of leaky HCF, R here is complex rather than real or pure imaginary. Although Bessel functions are still valid as solutions to Bessel eqn. (2-10) for complex argument, they are not real functions any more but complex.

The complex function which describes a mode introduces a phase distribution of the field. Here complex $\psi = |\psi|e^{i\arg(\psi)}$ in eqn. (2-10) is to describes the field strength by its amplitude $|\psi|$ and the phase distribution by its argument $\arg(\psi)$. In the core of leaky HCF, the phase distribution of a mode may present a difficult look than the conventional fibre.

In section 3.4 of Chapter 3, our simulations will demonstrate that in our low loss HC-NCF, effective index of fundamental mode, which is defined as

$$n_{eff} = \frac{\beta}{k} \qquad (2-11)$$

typically has $\mathrm{Re}(n_{eff}) > 0.999$, and $\mathrm{Im}(n_{eff})$ in the order of $10^{-2}\sim10^{-4}$ in magnitude within the low loss spectral region. In simulations, the core diameter is usually 15 times larger than the wavelength. The complex values of J_1 with these complex parameters are plotted in fig. 2.2.

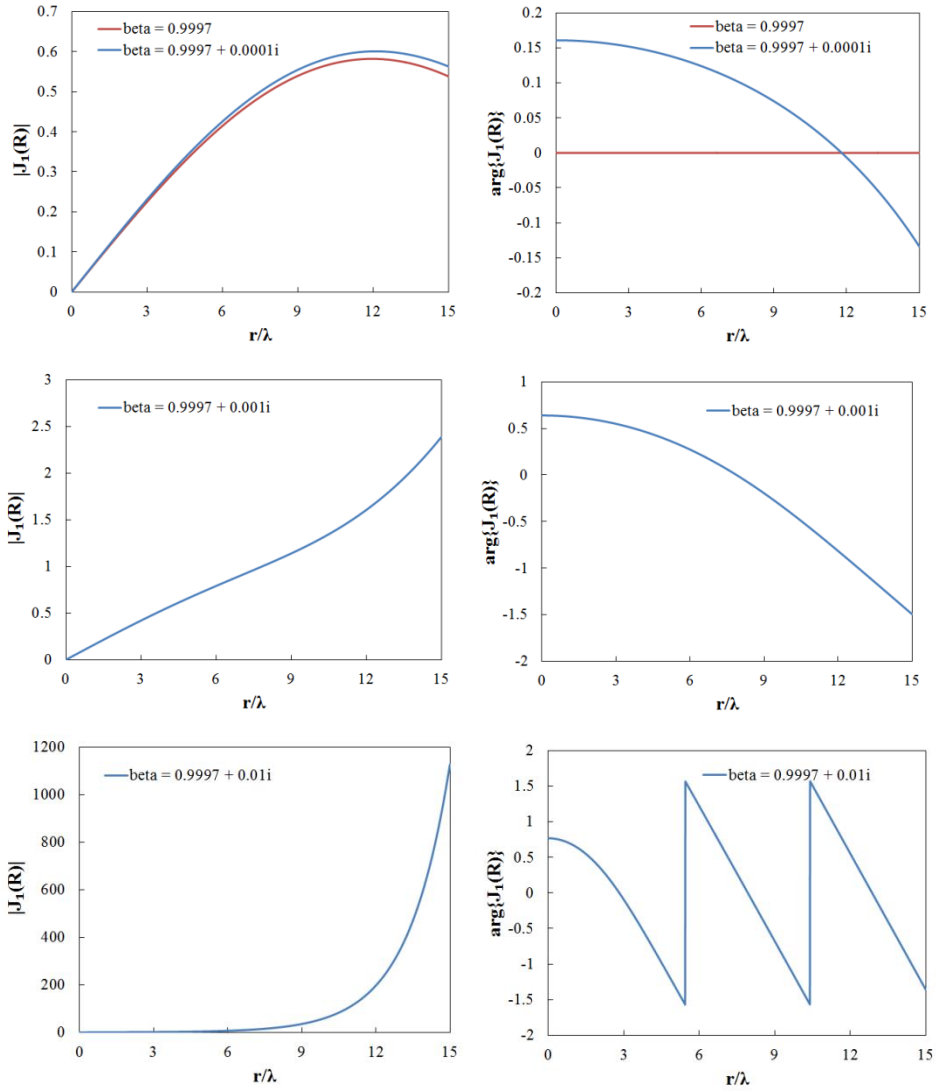

Fig. 2.2 Bessel functions of the first kind J_1 with $\beta = 0.9997, 0.9997 + 0.0001\mathrm{i}, 0.9997 + 0.001\mathrm{i}$ and $0.9997 + 0.01\mathrm{i}$.

From fig. 2.2 we can see that for β with very small imaginary part (that can even be ignored), the complex field distribution behaves similarly to its corresponding real function. But, as the loss becomes significant, the modes present new features. Those features mathematically originate from the nature of the complex function. Physically, the inherent loss is caused by the failure of TIR.

2) New eigenfunction and eigenvalue equation

The failure of TIR not only brings in a complex β but also changes the eigenvalue equation. As light is no longer totally confined in the core, the external field outside the core region is not described by the modified Bessel function of the second kind $K_m(iR)$ but by a Hankel function $H_m(R)$ instead.

Hankel functions are defined as

$$H_m^{(1)} = J_m + iY_m \qquad (2-12)$$

$$H_m^{(2)} = J_m - iY_m \qquad (2-13)$$

where Y_m is the Bessel function of the second kind.

Asymptotic expansions of Hankel functions for large argument $(R \to \infty)$ are as follows [3]

$$H_m^{(1)}(R) \sim \left(\frac{2}{\pi R}\right)^{1/2} \exp\left\{i\left(R - m\frac{\pi}{2} - \frac{\pi}{4}\right)\right\} \qquad (2-14)$$

$$H_m^{(2)}(R) \sim \left(\frac{2}{\pi R}\right)^{1/2} \exp\left\{-i\left(R - m\frac{\pi}{2} - \frac{\pi}{4}\right)\right\} \qquad (2-15)$$

Asymptotic features indicate that Hankel functions essentially describe travelling wave in cylindrical coordinates. $H_m^{(1)}$ represents the travelling wave propagating from the origin towards infinity and $H_m^{(2)}$ is in the opposite direction.

Besides the replacement of Bessel functions by Hankel functions to describe the field of mode in the cladding, the eigenvalue equation also becomes much more complicated due to complex boundary conditions of real HCFs.

In the index guiding fibre, as the field in the cladding quickly decays, only the boundary between the core and cladding matters in the derivation of the eigenvalue equation and other boundaries beyond are always ignored. But, in leaky HCFs, all boundaries becomes equivalently important and the change of eigenfunction makes the derivation of eigenvalue equations much more complicated. Even in the simplest capillary waveguide/ tube waveguide, the new boundary condition can bring in great challenges (which are much more difficult to solve).

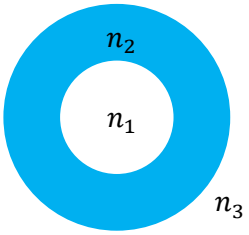

Fig. 2.3 Schematic of a capillary waveguide where refractive indexes in different regions satisfy $n_2 > n_3 \geq n_1$. Light propagates in the core in a leaky way.

In a capillary waveguide, ψ of region n_1 has $\psi = \begin{pmatrix} A_e \\ A_h \end{pmatrix} J_m$, where A_e represents the magnitude of the electric field and A_h for the magnetic field;

In region n_2, due to the multiple reflections between boundaries, ψ can be expressed as $\psi = \begin{pmatrix} B_e \\ B_h \end{pmatrix} H_m^{(1)} + \begin{pmatrix} C_e \\ C_h \end{pmatrix} H_m^{(2)}$;

In region 3we assume that wave propagates outwards from the core, so $\psi = \begin{pmatrix} D_e \\ D_h \end{pmatrix} H_m^{(1)}$.

At two boundaries, the continuity of $(e_\varphi, e_z, h_\varphi, h_z,)$ make two sets of 4×4 linear equations and each contains 6 variables. Together they transform to a complete 8×8 linear equation set containing 8 independent variables.

$$M_{8\times8}(A_e, A_h, B_e, B_h, C_e, C_h, D_e, D_h)^T = 0 \qquad (2-16)$$

The eigenvalue equation can then be derived from

$$\det(M_{8\times8}) = 0 \qquad (2-17)$$

Obviously, even the eigenvalue equation of the simplest capillary waveguide already becomes so complicated that the calculation has to heavily depend on numerical simulations. We could expect that in real HCFs with finer structures like HC-NCF, the eigenvalue equation will be too difficult to solve in an analytical way.

In summary, in leaky HCFs, because of the failure of TIR, a complex propagation constant must be introduced. This takes Bessel function from the real domain to the complex domain. The external field of the mode outside the core no longer simply decays in the radial direction but propagates transversely. The Hankel function must replace the modified Bessel function of the second kind for the field outside the core region. Meanwhile the complex boundary condition determines the form of eigenvalue

equation due to the fine structure of cladding. Those new changes bring challenges in the establishment of mode theory of leaky HCF, which is still under development.

2.1.3 Leaky mode of conventional fibre and mode of leaky HCF

This section introduces the leaky mode concept in the conventional index guiding fibre, which helps us to understand the cladding mode coupling model [8] discussed in section 2.2.3.

1) Leaky modes in the mode theory

In the conventional fibre, when TIR fails, e.g. $\beta < kn_{cladding}$, power starts to radiate transversely from the core to the environment. Under this situation, there are two kinds of new modes which can carry power away from the core, one is the radiation mode and the other is the leaky mode [1].

A radiation mode is characterised by continuous β which implies that the boundary conditions of this kind mode are always satisfied. As a result the freedom of eigenvalue equation set must be smaller than number of variables. To maintain the stable distribution of the field in the core and physical rationality, ψ_{rad} of radiation mode can be expressed as

$$\psi_{rad} = \begin{cases} AJ_m & \text{in the core} \\ BJ_m + CH_m^{(1)} & \text{in the cladding} \end{cases} \quad (2-18)$$

Leaky modes are characterised by discrete β. In comparison with radiation mode, leaky modes can be expressed as below out of discrete nature of β.

$$\psi_{leaky} = \begin{cases} AJ_m & \text{in the core} \\ BH_m^{(1)} & \text{in the cladding} \end{cases} \quad (2-19)$$

Leaky modes in conventional fibres behave as a bound mode and can be interpreted as bound modes just below cut-off condition [1].

Normalized frequency of waveguide is defined as

$$V = \frac{2\pi}{\lambda} a \sqrt{n_{core}^2 - n_{cladding}^2} \quad (2-20)$$

where a is the core radius. When V reaches the cut-off frequency V_c of a certain mode, a perturbation of infinitesimal increment $\Delta\lambda$ will make $V < V_c$, but it can barely change the mode profile. This small change V brings in an infinitesimal imaginary

part of β [1]. Such an imaginary part of β implies that the bound mode radiates power from the core to the external.

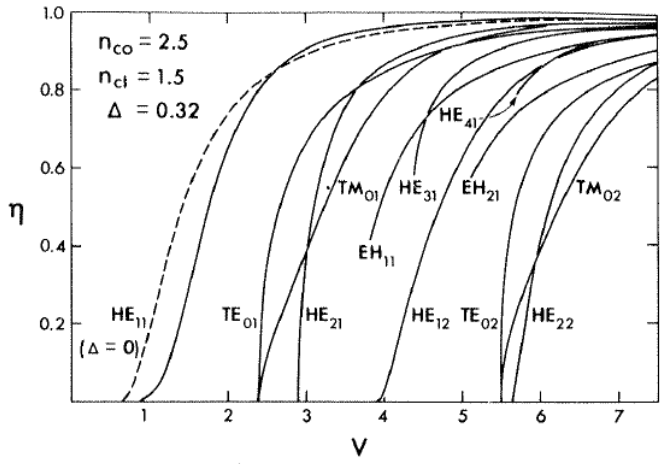

Fig. 2.4 Fraction of modal power in the core as function of V.The dashed line is limit for the fundamental mode as $n_{core} \rightarrow n_{cladding}$. This fig is cited from ref [1].

The origin of leaky modes can be examined by studying mode properties near cut-off. As V reaches cut-off, bound modes expand rapidly into the cladding and finally radiates to the environment below cut-off. However, as fig. 2.4 shows, all modes except of $TE_{0n}, TM_{0n}, HE_{1n}$ and HE_{2n} still have portion of energy stored in the core even at cut-off. It implies that power of light will not simply dissipate into the environment but can still propagate along the length even below cut-off just as bound modes (which has the lateral wave vector still to satisfy the transvers resonance condition and has a stable field distribution along the propagation). Figure 2.4 can be regarded as evidence supporting the existence of the leaky mode. In fact, theoretical analysis demonstrates that $\mathrm{Im}(\beta)$ of leaky mode is very small for those high order bound modes below cut-off [5]. For $TE_{0n}, TM_{0n}, HE_{1n}$ and HE_{2n}, no energy can be found stored in the fibre below the cut-off and attenuation coefficients of corresponding leaky modes are numerically found very large [4].

The attenuation of leaky modes in conventional fibres can be deduced from eigenvalue equation [1]

$$\alpha = \frac{4}{\pi}\frac{\sqrt{2\Delta}}{a}\frac{(U^r)^2}{V^3}\left|\frac{1}{H_{m-1}^{(1)}(Q^r)H_{m+1}^{(1)}(Q^r)}\right| \qquad (2-21)$$

where $\Delta = \frac{n_{core} - n_{cladding}}{n_{core}}$, a is core radius, $U^r = Re\left(\frac{2\pi a}{\lambda}\sqrt{n_{core}^2 - n_{eff}^2}\right)$, $Q^r = Re\left(\frac{2\pi a}{\lambda}\sqrt{n_{cladding}^2 - n_{eff}^2}\right)$.

After simplification, we can have

$$\alpha \propto \frac{\lambda}{a^2} \qquad (2-22)$$

In summary leaky modes in conventional index guiding fibres are "bound modes" below cut-off which have almost identical field distributions as bound modes but do not satisfy TIR. They radiate energy along the length with fairly small attenuation factor which is quite different from the fast decaying radiation modes.

2) Leaky mode in conventional fibre and mode in leaky HCF

Leaky modes in the index guiding fibre and modes in the leaky HCF have no inherent relationship. The introduction of leaky mode in the mode theory is key for us to understand the interaction between the core modes and cladding modes in leaky HCFs. This mode coupling interaction plays an important role in determining the low loss transmission window of leaky HCFs. More details will be discussed in section 2.2.3.

The preliminary condition of mode coupling is the phase matching condition. However because of refractive index differences, the coupling between the core modes and cladding modes in leaky HCFs can only happen between the airy modes in the core and leaky modes in the cladding material.

In the leaky HCF, n_{eff} of low loss mode is almost equal to n_{core}. Under the approximation of ray optics, as $n_{eff} \sim n_{core}$, light transmitted in the HCF can be regarded as being reflected by the core wall at the grazing incident angle. The grazing incident supplies high reflectivity to support light transmission along the leaky HCF. As a result, low loss modes in leaky HCF must satisfy approximation of quasi-plane wave propagation. Because of much higher refractive index differences, no bound modes in the cladding material but leaky modes can couple with airy modes in the core of HCFs.

Leaky modes exist below cut-off. In ray optics model, it corresponds to incident optical ray just below critical angle. Under certain condition, when transverse

resonance condition is satisfied, leaky modes exist. In this situation, leaky modes are far from the approximation of quasi-plane wave propagation in the solid material (this can explain why low order leaky mode barely exits and bound modes of $TE_{0n}, TM_{0n}, HE_{1n}$ and HE_{2n} do not have corresponding leaky modes under cut-off as shown in fig. 2.4).

As a result, only the leaky mode can possess the effective refractive index below the air line and make it possible to interact with the airy modes in the core in leaky HCFs.

Radiation modes in the cladding can also participate in the coupling with the cores in leaky HCFs. However under this situation, the loss of core modes will be too significant that the discussion of light propagating in the core becomes meaningless.

2.2 Other theoretical models of leaky hollow core fibre

To effectively analyse the mode properties, different models of leaky HCFs were also proposed. Among them, three important models are introduced and discussed in this section.

2.2.1 Marcatili and Schmeltzer's formula

In 1964, Marcatili and Schmeltzer firstly systematically studied the attenuation and bending properties of hollow waveguides. They concluded that hollow core dielectric waveguide was not attractive as a transmission medium for long distant optical telecommunications [5].

In their theory, the cladding structure of the waveguide was simplified. Their assumed that wave propagated in a lower refractive index core surrounded by an infinite and uniform cladding of higher refractive index. Some mathematical approximations were made in the derivation of analytical expressions of the modes.

Their estimation of attenuation of HCF was widely acknowledged and used to evaluate the performance of hollow core waveguides [5]

$$\alpha = \left(\frac{u_{nm}}{2\pi}\right)^2 \frac{\lambda^2}{a^3} \mathrm{Re}(\nu_n) \qquad (2-23)$$

where u_{nm} is mth root of $J_{n-1} = 0$; a is the radius of hollow core; λ is wavelength; ν_n is a constant for different modes and is given by

$$\nu_n = \begin{cases} \dfrac{1}{\sqrt{n^2-1}}, & \text{for } TE_{0m} \\ \dfrac{n^2}{\sqrt{n^2-1}}, & \text{for } TM_{0m} \\ \dfrac{1}{2}\dfrac{n^2+1}{\sqrt{n^2-1}}, & \text{for } EH_{nm} \end{cases} \qquad (2-24)$$

where n is the refractive index of the cladding material.

Eqn. (2-23) indicates that attenuation of leaky HCF is mainly determined by the mode order and core size. The fundamental mode in a large core always has a much lower attenuation than other modes. However they also pointed out that enlarging the core size also brought in higher bending loss which can fundamentally limit the applications of hollow core waveguide. In a straight tube waveguide made of silica glass with 1 mm core radius, the predicted attenuation of EH_{11} can reach 1.85 dB/km

at the wavelength of 1 μm, however this attenuation will be doubled if the bending radius is 10 km.

2.2.2 Anti-resonance reflecting optical waveguide model

ARROW, the Anti-Resonant Reflecting Optical Waveguide model is widely adopted as a simple model to explain HC-PBG and other HCFs. The ARROW model was firstly proposed in 1986 to explain the enhanced confinement in the planar waveguide where a series of high-low index regions form the cladding [6]. In 2002 it was used to provide an easy way to understand the light transmission in HC-PBG in terms of waveguide theory rather than the tight binding theory [7].

The ARROW model is 2D model and can be extend to higher dimensions. The basic idea behind is that the first high index layer of cladding around the core functions as a Fabry-Perot resonator which provides reflection to enhance the confinement of light in the lower index core. As fig. 2.5 shows, when the wavelength of light in the core matches a resonant wavelength of the Fabry-Perot cavity, light will leak out of the core through the high index layer. As the wavelength is far away from resonance of the cladding, light will be reflected back and more strongly confined in the core of the waveguide. The wavelengths matching the resonance condition finally determine the edge of low loss bands of hollow core waveguide.

Mathematically the ARROW model can be expressed as,

$$\lambda_{anti} = \frac{4d}{(2m+1)}\sqrt{n_2^2 - n_1^2} \qquad (2-25)$$

in which d is the thickness of the cladding, n_1 and n_2 are refractive indexes of the core and the cladding, m is the integer staring from 0. λ_{anti} is the wavelength out of cladding resonance and therefore can propagate in the hollow core with a relatively small attenuation.

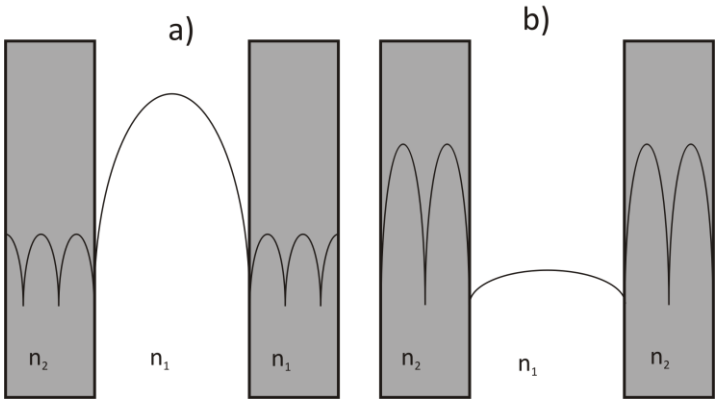

Figure 2.5 Schematic representations of the optical field intensity profile in the core region and first high index regions. a) is the anti-resonant case where light is confined in the core region and b) is when the wavelength is close to a resonance of the high index regions corresponding to the peak transmission of the Fabry-Perot cavity.

The ARROW model uses ray optics to explain the waveguide characteristics. Therefore the ARROW model is only effective when $d/\lambda \gg 1$, and is invalid to apply in the long wavelength spectral region. ARROW cannot predict the loss magnitude or any other band details either. Although the ARROW model is far from perfection, it is still widely acknowledged as one of the most effective and frequently used model to understand leaky HCFs.

2.2.3 Cladding leaky mode coupling model

In 2010 Vincetti and Setti purposed that coupling between dielectric modes in the cladding and airy mode in the core decides the position of low loss transmission and they demonstrated this conclusion by numerical simulations with the finite element method [8]. Coupling between airy and dielectric modes can be used to direct the design of low loss HCFs.

In Vincetti and Setti's simulations, the cladding of HCF was formed of capillary. The dielectric layer of capillary was considered as a high index waveguide which had been theoretically modelled by Kharadly and Lewis in 1969 [9]. Below the cut-off, leaky modes of the dielectric layer waveguide can couple with airy modes in the core. Under this circumstance, high loss spectral region of the airy mode was decided by coupling with the leaky mode in the cladding while the energy of light in the core would quickly leak through the cladding to the external.

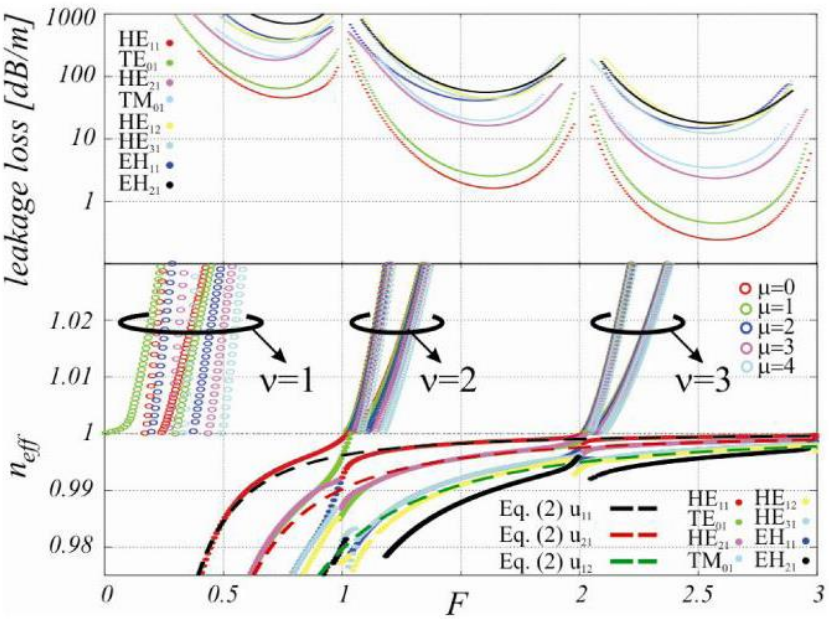

Fig. 2.6 Top: Loss of airy modes of different orders (fig. 2.6 is cited from ref [5]). Bottom: dispersion curves of airy and dielectric modes versus the normalized frequency F. Dielectric layer has refractive index n=1.44 is considered. Dashed lines represent the dispersion curves predicted by [5].

Figure 2.6 top shows the simulation results of spectral attenuation of core modes. Fig. 2.6 bottom shows dispersion curves of dielectric mode (cladding mode) and airy modes (core mode) as functions of normalized frequency F which is defined in eqn. (2-20). ν and μ are radial and azimuthal indexes respectively which are used to label the order of mode.

In fig. 2.6 bottom, the dashed lines are dispersion curves of airy mode predicted by Marcatili and Schmeltzer [5]. Below the air line, in the low loss spectral region, the simulated dispersion curve of core modes overlap well with the air mode in Marcatili and Schmeltzer's prediction. Starting from the cut-off of dielectric mode, the core mode dispersions gradually deviate from Marcatili and Schmeltzer's prediction and join the dispersion curves of dielectric mode as F decreases. As the effective indexes of core mode and cladding mode depart from each other, the much reduced mode coupling causes the attenuation of air modes to drop quickly thus forming the low loss bands.

To obtain broad low-loss spectral regions, the cut-off frequencies of different dielectric modes must be more convergent rather than spread out in the spectrum. As fig. 2.7 shows, simulation demonstrates that as thickness or refractive index of dielectric layer increases, cut-off frequencies of dielectric modes start to scatter

broadly (ρ is the inner and outer diameter ratio of capillary). This implies that a thin capillary is always preferable fabricating low loss HCF. This has been also shown in my simulation described in the next section.

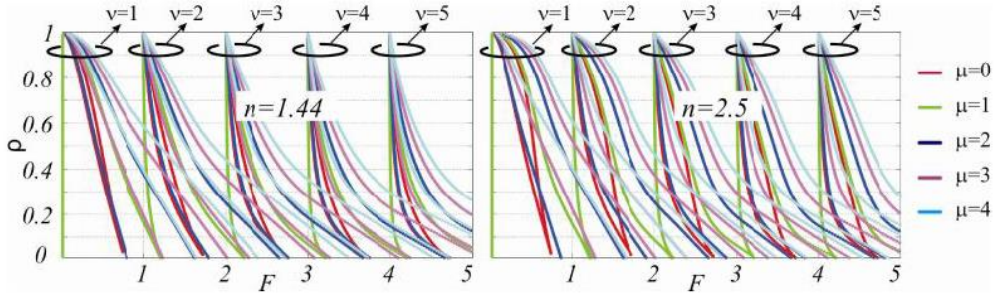

Fig. 2.7 Normalized cut-off frequencies versus the inner and outer diameter ratio of capillary ρ, for two different dielectric refractive indices: n=1.44 and 2.5 (fig. 2.7 is cited from ref. [5]).

The mode coupling model can be helpful for qualitative analysis of loss properties of leaky HCFs; however this analysis will becomes more and more complicated due to the increased complexity of cladding structures. Numerical simulations then become more and more important to understand the guidance properties of leaky HCFs.

2.3 Discussion of the curvature of the core wall in leaky HCF

The importance of curvature of the core boundary had not been recognized until Wang et al. demonstrated that negative curvature can effectively reduce attenuation of Kagome fibre [10]. However, until now no model has quantitatively explained the effect of core curvature in the leaky HCF. The function of curvature of core boundary has not been fully understood yet. This section attempts to analyse the role of boundary curvature in term of depressing coupling between the core mode and cladding modes.

In the capillary waveguide, the core boundary is of cylindrical shape with surface normal direction from the core to the external. Usually we define this direction as positive and such curvature of core wall as positive.

Here I will try to present a picture of the function of negative curvature in leaky HCF based on mode coupling model.

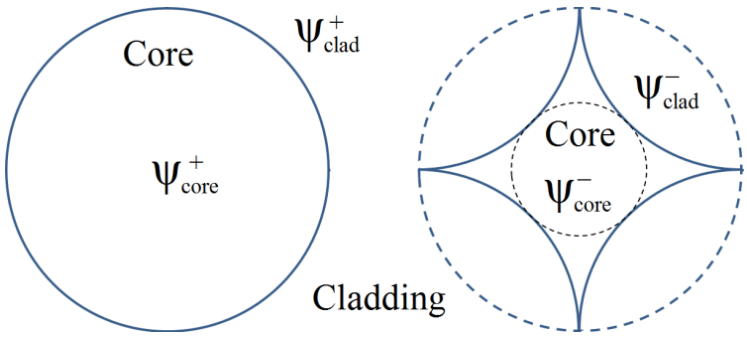

Fig. 2.8 Schematic of cores with positive (left) and negative curvature (right). $\Psi^{\pm}_{core}$ and $\Psi^{\pm}_{clad}$represent modes in the cores and claddings.

Figure 2.8 is a schematic of core regions in HCF with positive curvature (left) and negative curvature (right). Outside the core is cladding region which may have fine structures (omitted in the figure). The solid blue lines show the core-cladding boundary. $\Psi^{\pm}_{core}$ and $\Psi^{\pm}_{clad}$represent modes in the cores and claddings. On the right of fig. 2.8, the negative core boundary is formed by folding dashed line (virtual positive curvature core wall) towards the core.

In HC-NCF (fig. 2.8 right), the folding of boundary compresses the mode area and as a result the core mode becomes smaller in size. The approximate core mode area is illustrated by the black dashed line which is fundamentally constrained by the core boundary. A smaller core size results in a smaller β of the core mode at the same time. In fig. 2.8, we can find that at the same wavelength, Ψ^{-}_{core} has a smaller β than Ψ^{+}_{core},

which means that the dispersion curve of Ψ_{core}^{-} would shifts down from the air line in comparison with Ψ_{core}^{+}. In this case the coupling between the core mode Ψ_{core}^{-} and the cladding mode Ψ_{clad}^{-} becomes weaker because of the phase mismatching. A reduced attenuation can be expected in the HC-NCF at the same transmission spectral window.

The overlap between the core mode and cladding mode is also possibly reduced due to the negative curvature. If we assume that the profile of core mode is refrained, then the coupling coefficient between the core modes and cladding modes can be reduced too by the reduction of overlap between the core mode and cladding mode, which decrease the attenuation of HC-NCF.

In summary, when the core boundary has a negative curvature, the shift of the core mode dispersion curve and reduction of core mode overlap with cladding mode may depress the coupling between the airy mode in the core and leaky mode in the cladding, which fundamentally reduces the attenuation of HC-NCFs.

2.4 Scaling law of Maxwell equations

Under the assumption of a macroscopic system, there is no fundamental length scale of electromagnetic wave in the dielectric media [12]. The electromagnetics properties in such a system are scale invariant while media dimension scales with wavelength. This is the underlining principle to direct HCF fabrication by scaling fibre dimensions for different transmission wavelength regions.

The master equation governing the light in a medium is as follows [12],

$$\boldsymbol{\nabla} \times \left\{ \frac{1}{\varepsilon(\mathbf{r})} \boldsymbol{\nabla} \times \mathbf{H}(\mathbf{r}) \right\} = \left(\frac{2\pi}{\lambda} \right)^2 \mathbf{H}(\mathbf{r}) \qquad (2-27)$$

where $\varepsilon(\mathbf{r})$ represents material and structural spatial distribution of dielectric media and $\mathbf{H}(\mathbf{r})$ is its eigenmode.

Let us assume that the dimension of dielectric media is scaled s times from the original but keeps the geometrical structure similar. Then the new medium is expressed as $\varepsilon'(\mathbf{r}) = \varepsilon(\mathbf{r}/\mathrm{s})$. For the new medium, its new eigenmode $\mathbf{H}'(\mathbf{r})$ and corresponding eigen-wavelength λ' satisfies

$$\boldsymbol{\nabla} \times \left\{ \frac{1}{\varepsilon(\mathbf{r}/\mathrm{s})} \boldsymbol{\nabla} \times \mathbf{H}'(\mathbf{r}) \right\} = \left(\frac{2\pi}{\lambda'} \right)^2 \mathbf{H}'(\mathbf{r}) \qquad (2-28)$$

If we make a substitution of variable in eqn. (2-27), by using $\mathbf{R} = \mathrm{s}\mathbf{r}$ and $\boldsymbol{\nabla}' = \boldsymbol{\nabla}/\mathrm{s}$, we can have

$$\boldsymbol{\nabla}' \times \left\{ \frac{1}{\varepsilon(\mathbf{R}/\mathrm{s})} \boldsymbol{\nabla}' \times \mathbf{H}(\mathbf{R}/\mathrm{s}) \right\} = \left(\frac{2\pi}{\mathrm{s}\lambda} \right)^2 \mathbf{H}(\mathbf{R}/\mathrm{s}) \qquad (2-29)$$

Because $\mathbf{H}(\mathbf{r})$ can always map λ one by one (neglecting degeneration of eigenmodes), by comparing eqn. (2-28) and eqn. (2-29) we finally have

$$\lambda' = \mathrm{s}\lambda \qquad (2-30)$$

As a result, scaling of structures can change wavelength by the same scaling factor but maintain the eigenmode profile unchanged.

Let us assume in a waveguide that $\mathbf{e}_{\mathrm{t}}^{(\mathrm{mn})}$ is the electric field of mode of order (m, n) which satisfies eqn. (2-4), and β_{mn} is the correspondent eigenvalue. When the waveguide dimension is transversely scaled by factor s but keep longitudinal scaling as 1, eqn. (2-4) becomes

$$\left(\nabla_t^2 + \frac{n(\mathbf{t}/s, \mathbf{z})^2 k^2}{s^2} - \beta'^2_{mn}\right)\mathbf{e}_t^{(mn)}(\mathbf{t}, \mathbf{z}) =$$
$$= -(\nabla_t + i\beta'_{mn}\mathbf{z})\mathbf{e}_t(\mathbf{t}, \mathbf{z}) \cdot \nabla_t \ln\left(n^2(\mathbf{t}/s, \mathbf{z})\right) \quad (2-31)$$

in which β' is the new propagation constant for the mode of the same order.

By using $\mathbf{T} = \mathbf{t}/s$ and $\nabla_T = s\nabla_t$, eqn. (2-31) becomes,

$$\left(\nabla_T^2 + n(\mathbf{T}, \mathbf{z})^2 k^2 - (s\beta'_{mn})^2\right)\mathbf{e}_t^{(mn)}(s\mathbf{T}, \mathbf{z}) =$$
$$= -(\nabla_T + is\beta'_{mn}\mathbf{z})\mathbf{e}_t(s\mathbf{T}, \mathbf{z}) \cdot \nabla_T \ln\left(n^2(\mathbf{T}, \mathbf{z})\right) \quad (2-32)$$

Since $\mathbf{e}_t^{(mn)}(\mathbf{t}, \mathbf{z})$ always maps β_{mn} one by one we must have,

$$\beta'_{mn} = \frac{\beta_{mn}}{s} \quad (2-33)$$

Finally we can conclude that

1) Transverse scaling of the medium dimension changes β of mode by the same factor but inversely;
2) After scaling, mode profile scales accordingly while other properties maintain the same.

The scaling property is a fundamental property of the electromagnetic field. By using this law, we can fabricate fibres for different spectral windows by simply scaling fibre size. However it needs to be remembered that the scaling law will lose validity in high material loss spectral region. There ε will have a strong wavelength dispersion which cannot be ignored.

2.5 Conclusions

Chapter 2 presents background material to understand the guidance mechanism of leaky HCF including HC-NCFs.

The theory of leaky HCF is still far from mature. Numerical simulation methods are still the basic tool to study and analyse properties of leaky HCF.

Marcatili and Schmeltzer's formula [5], the ARROW model [6, 7] and the cladding mode coupling model [8] present simple pictures describing the light guidance in leaky HCFs and help us understand the guidance mechanism of leaky HCFs..

The qualitative analysis indicates that the negative curvature core wall can reduce the interaction between the core modes and cladding mode, which ultimately decreases attenuations of the HC-NCFs.

Finally, the scaling law of Maxwell's equations is introduced and mathematically proved. This law directs the fabrication of HC-NCFs for applications in different wavelength ranges.

Reference

[1] A. W. Snyder and J. D. Love, Optical waveguide theory (Chapman & Hall, 1983).

[2] M. A. Gwaiz, Sturm-Liouville theory and its applications (Springer-Verlag, 2008).

[3] G. F. Carrier, M. Krook and C. E. Pearson, Complex function of a variable theory and technique (SIAM, 2005).

[4] A. W. Snyder and D. J. Mitchell, "Leaky mode analysis of circular optical waveguides," Opto-electronics, **6**, 287-96 (1974).

[5] E. A. J. Marcatili and R. A. Schmeltzer, "Hollow metallic and dielectric waveguides for long distance optical transmission and lasers," Bell Syst. Tech. J. **43**, 1783–1809 (1964).

[6] M. Duguary, Y. Kokubun, T. Koch and L. Pferiffer, "Antiresonant reflecting optical waveguides in SiO2-Si multilayer structures," Appl. Phys. Lett. **49**, 13-15 (1986).

[7] N. M. Litchinitser, A. K. Abeeluck, C. Headley, and B. J. Eggleton, "Antiresonant reflecting photonic crystal optical waveguides," Opt. Lett. **27**, 1592-1594 (2002).

[8] L. Vincetti and V. Setti, "Waveguiding mechanism in tube lattice fibers," Opt. Express **18**, 23133-23146 (2010).

[9] M. Kharadly and J.Lewis, "Properties of dielectric-tube waveguides," Proc. IEE **116**, 214-224(1969).

[10] Y. Wang, F. Couny, P. J. Roberts, and F. Benabid, "Low loss broadband transmission in optimized core – shaped Kagome Hollow Core PCF," in Conference on Lasers and Electro-Optics/Quantum Electronics and Laser Science, Postdeadline Papers (Optical Society of America, Washington, D.C., 2010), paper CPDB4

[11] P. J. Roberts, F. Couny, H. Sabert, B. J. Mangan, D. P. Williams, L. Farr, M. W. Mason, A. Tomlinson, T. A. Birks, J. C. Knight, and P. St.J. Russell, "Ultimate low loss of hollow-core photonic crystal fibres," Opt. Express **13**, 236-244 (2005).

[12] J. D. Joannopoloulos, S. G. Johnson, J. N. Winn and R. D. Meade, Photonic crystal molding the flow of light (Princeton university press, 2008).

Chapter 3 Simulations of hollow core negative curvature fibre

In this section, numerical simulations of HC-NCF by Comsol (a commercially available finite element method software package) are presented and discussed. The capillary thickness of cladding is found as the most important factor determining the attenuation of HC-NCF.

3.1 Simulation model and important parameters in simulation

3.1.1 Geometry of simulated model

The geometry of HC-NCF investigated in my study in this chapter is depicted in Fig 3.1. The core has a closed boundary formed by 8 identical capillaries touching each other, which form the cladding. A jacket tube is used to protect the fibre structure from the environment in fabrication and applications. The jacketing tube contacts the cladding capillaries at points. The core diameter is *D* which is defined as the distance between capillaries across the core. The jacket tube thickness is t, d_{in} and d_{out} are inner and outer diameter of capillary respectively. A parameter η is defined as

$$\eta = \frac{d_{in}}{d_{out}} \qquad (3-1)$$

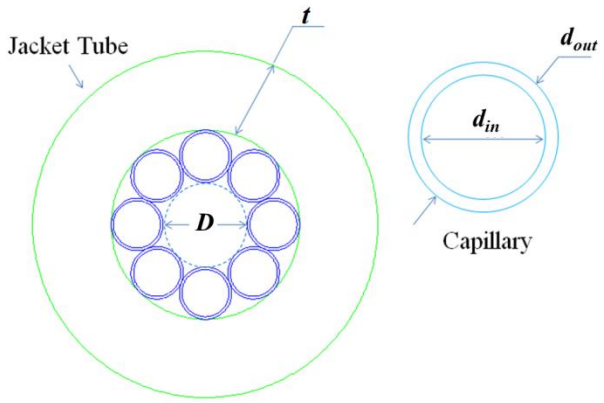

Fig. 3.1 Geometry of negative curvature HCF

According to the scaling law, low attenuation or band position can be shifted easily by scaling the fibre dimension. Therefore the absolute D value is not important. In our simulation D is fixed as 36 μm. Our simulation results are all presented as function D normalized by wavelength λ.

3.1.2 Material dispersion and absorption

In the simulations the material of jacketing tube and cladding is silica glass. All the other regions in fig. 3.1 including the core of the fibre is filled with air with the refractive index n = 1.

The Sellmeier equation [1] is used here to approximate the silica glass material dispersion in the simulations.

$$n^2(\omega) = 1 + \sum_{j=1}^{m} \frac{B_j \lambda^2}{\lambda^2 - \lambda_j^2} \qquad (3-2)$$

where λ_j is the resonance wavelength and B_j is the strength of the jth resonance. Here λ_j and B_j are evaluated as $B_1 = 0.6961663$, $B_2 = 0.4079426$, $B_3 = 0.8974794$, $\lambda_1 = 0.0684043$ μm, $\lambda_2 = 0.1162414$ μm, $\lambda_3 = 9.0896161$ μm [1].

In our simulation, the material absorption as the function of wavelengths is not considered when calculating spectral attenuation of fibres. Actually, due to phonon absorption, silica glass starts to present strong absorption features after 2 μm and beyond 3 μm the absorption of silica increases very rapidly [2]. At 4 μm material absorption reaches over 800 dB/m. Instead of modelling this directly, the attenuation due to the material absorption is studied by introducing different absorption strengths when calculating the mode attenuation at a single wavelength. Relevant results can be found in section 3.5.

Neither the material absorption nor the dispersion of air is considered in the simulation.

3.1.3 Fundamental mode restriction

There has been no clear definition or systematic classification of modes in leaky HCF so far. Terminology is borrowed from conventional fibre optics to name and describe modes in leaky HCF [3].

The fundamental mode of HC-NCF is defined by the largest value of β (neglecting polarization) which satisfies the eigenvalue equation at the given wavelength. Figure 3.2 shows the simulated spatial distribution of power flow in the longitudinal direction for two modes in HC-NCF. On top is the fundamental mode, which is Gaussian-like and has $n_{eff} = 0.999555 - i6.660849 \times 10^{-9}$; on bottom is a higher order mode, which has $n_{eff} = 0.998866 - i1.574214 \times 10^{-8}$.

The attenuation of the fibre is defined as [1]

$$\alpha_{dB} = -\frac{10}{L} log_{10}\left(\frac{P_{out}}{P_{in}}\right) \qquad (3-3)$$

where L is the length of fibre, P_{in} and P_{out} are input and output powers in the fibre. According to eqn. (2-10), we have attenuation in dB unit equal to

$$\alpha_{\mathrm{dB}} \approx -4.343\alpha \qquad (3-4)$$

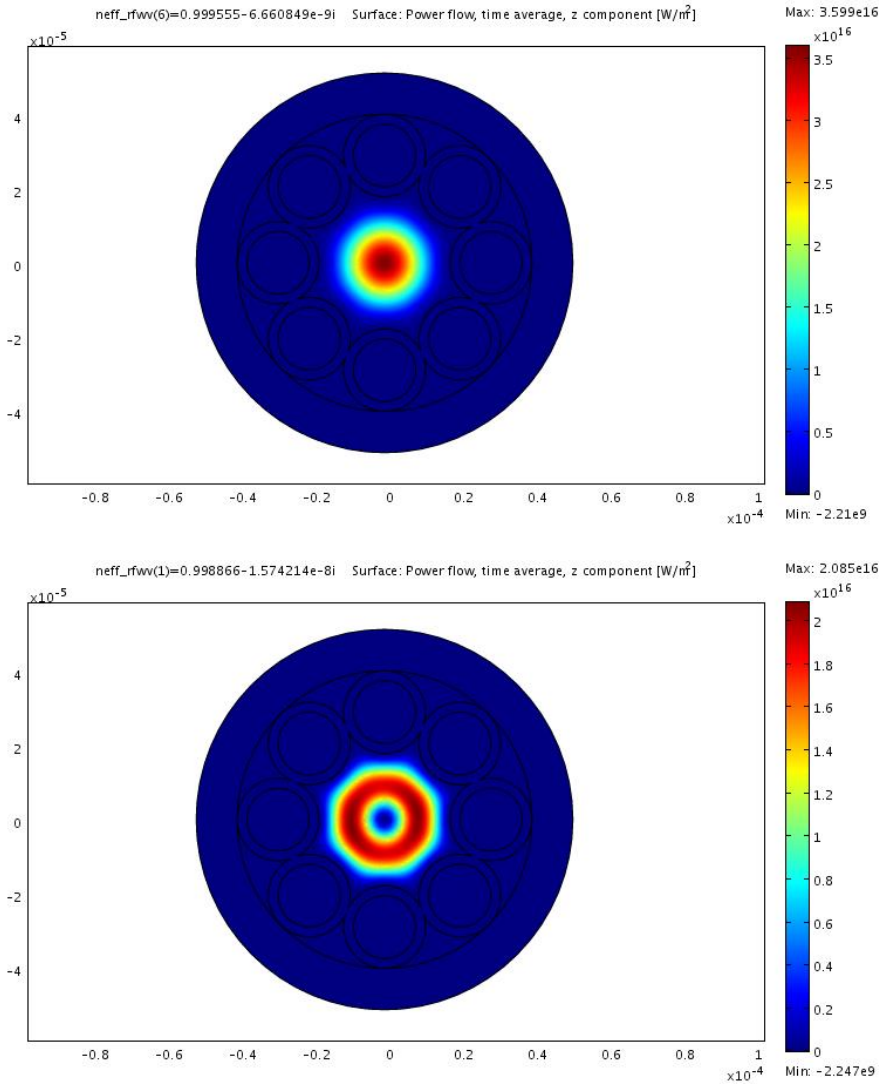

Fig. 3.2 Top: distribution of power flow in longitudinal direction of fundamental mode in HC-NCF with η = 0.76; bottom: distribution of power flow in longitudinal direction of high order mode with η = 0.76. Units of x and y axes are meters.

In fig. 3.2 we can see that the high order mode has a more complicated field pattern and that the attenuation level is almost one order of magnitude higher than the fundamental mode. Since a higher order mode always exhibits higher loss, the fundamental mode plays a more important role in real applications. As a result, our simulations mainly focus on the properties of fundamental mode in HC-NCFs including attenuation and dispersion. Unless otherwise indicated, all the simulation results presented in this chapter are about the fundamental mode.

3.1.4 Simulation method

All of our simulations presented in this chapter are calculated by *Comsol* 3.5a. The package for hybrid-mode analysis of the perpendicular wave transmission in the RF module and the UMFPACK linear system solver are adopted for calculations in all the simulations.

To restrict our calculation to the fundamental mode, the initial effective index for mode searching is always set to 1 and is iterated with the return effective index until the fundamental mode is found.

A perfect matching layer is adopted in the simulations outside the jacket tube to absorb any transvers energy flow. A scattering boundary condition is applied to external boundary of the air layer. Coordinates of perfect matching layer and scattering boundary condition are unified as cylindrical coordinates.

Meshing is performed by the inherent arithmetic of *Comsol* software and restriction is manually applied to make sure the meshing dimension inside fibre is no more than a quarter of the wavelength in simulation. (Some regions inside jacket tube and external air layer usually have bigger meshing size due to limit of RAM storage)

3.2 Effect of capillary thickness on fibre loss

In our simulated model the cladding is very simple and one of the most important parameters that significantly influences fibre loss is the capillary thickness, characterized by η.

In our simulations we calculated the fundamental mode attenuation as function of wavelength for different values of η equal to 0.1, 0.5, 0.76, 0.9 and 0.95. The simulated wavelength range is between 1.2 μm and 1.8 μm, covering the important near-infrared wavelength range for research and applications. All the attenuation curves are plotted in fig. 3.3.

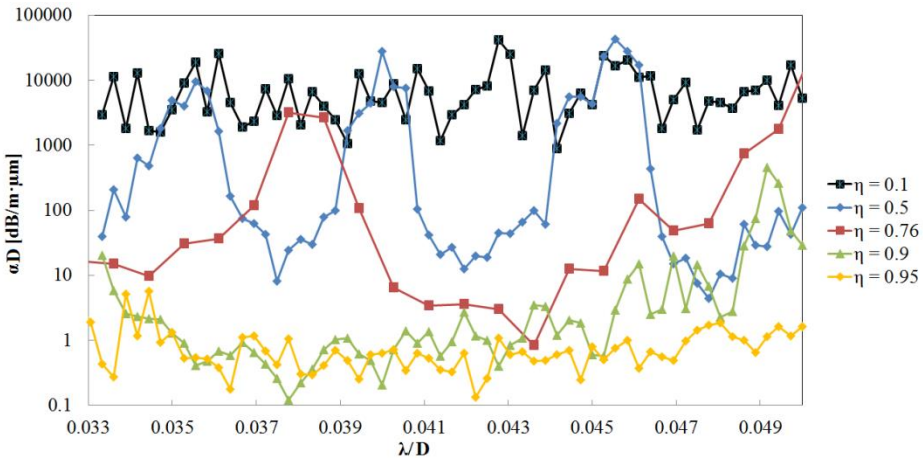

Fig. 3.3 Normalized attenuations of fundamental mode as function of normalized wavelength for different capillary thickness ratios.

From fig. 3.3 we find that as the thickness of the capillary wall is reduced, the attenuation level of the fundamental mode drops quickly. At the same time the low loss band becomes wider and flatter.

According to the ARROW model, wavelengths which satisfy the resonant condition of capillary thickness can leak through the cladding and these wavelengths form the edge of transmission bands, given by

$$\lambda_{res} = \frac{2d}{m}\sqrt{n_2^2 - n_1^2} \qquad (3-5)$$

where d is the capillary thickness and $n_2 = 1.44$ and $n_1 = 1$. Resonant wavelengths and corresponding orders for different capillary thicknesses are calculated and listed in table 3.1.

	$\eta = 0.1$	$\eta = 0.5$	$\eta = 0.76$	$\eta = 0.9$	$\eta = 0.95$
normalized λ_m	$\frac{0.5828}{m}$	$\frac{0.3238}{m}$	$\frac{0.1554}{m}$	$\frac{0.0648}{m}$	$\frac{0.0323}{m}$
m for Fig. 3.3	12 - 17	9, 8, 7	4	-	-

Table. 3.1 Normalized Resonance wavelengths and orders for different η with $n_2 = 1.44$ and $n_1 = 1$.

Comparing Table 3.1 with fig. 3.3, we can see that the resonance wavelengths predicted by the ARROW model match fairly well with the high loss wavelengths of the simulated attenuation curves especially for $\eta = 0.5$ and 0.76. For the thicker capillaries, it becomes harder to distinguish between low loss and high loss spectral regions.

Figure 3.3 reveals the relation between the fibre loss and capillary thickness in the cladding. A thinner capillary supports fewer cladding modes at the same wavelength so that the coupling between the core modes and cladding modes becomes weaker, and effectively reduces the mode attenuation.

A simulation of mode attenuation at even longer wavelengths is shown in fig. 3.4 for $\eta = 0.76$. In this scan, no band can be found when $\lambda/D \geq 0.103$. The high loss at the long wavelength can be estimated by Marcatili and Schmeltzer's formula, e.g. eqn. (2-23). In a capillary waveguide, mode attenuation scales with λ^2 and longer wavelengths suffer higher loss in the transmission. This can also be interpreted that for long wavelength, the wave property of light becomes stronger. As the leaky HCF cannot supply any absolute confinement like TIR, the increased loss due to diffraction will finally limit the transmission of light in the long wavelength regime.

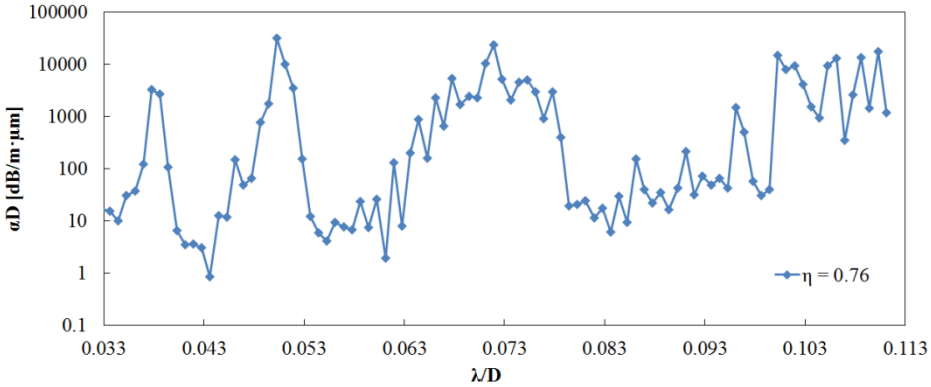

Fig. 3.4 Simulation of mode attenuation in a broad wavelength range for $\eta = 0.76$.

Here the ARROW model becomes invalid when explaining the properties of leaky HCF at long wavelengths and no theory can currently predict the longest "cut-off" wavelength in the first band of HC-NCFs.

3.3 Effect of jacketing tube thickness on fibre loss

The effect of jacketing tube thickness on the mode attenuation is also examined. Simulation results are plotted in fig. 3.5. No material absorption is considered in related simulations.

In simulation, η is 0.76 and the thickness of jacketing tube t is changed randomly while the rest parts of the structure in the simulation model remain the same. For those t/D =.278, 0.156, 0.114, attenuation curves match fairly well. For t/D =0.028,

the attenuation curve at the high region shifts down a little but remains the same at the low loss region.

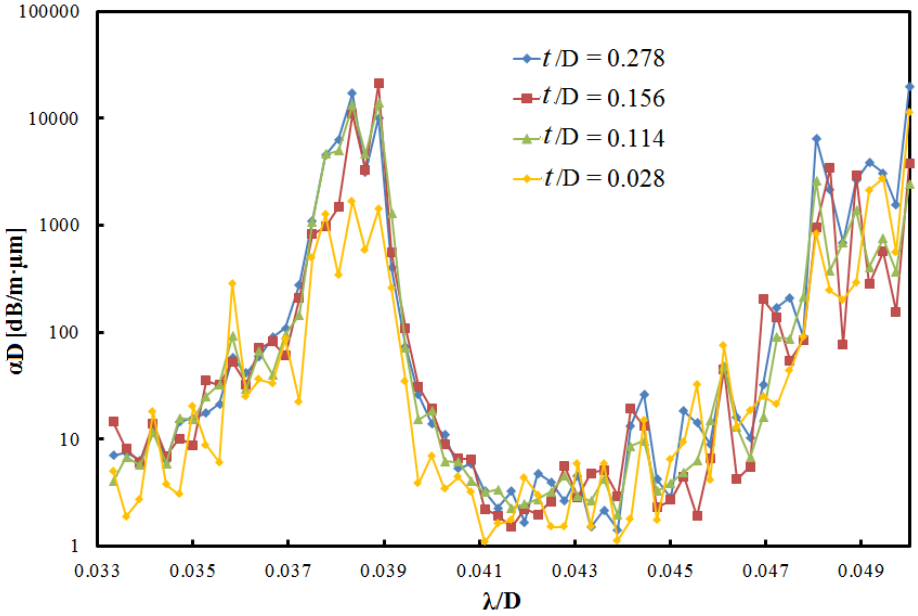

Fig. 3.5 Effect of jacket tube thickness on mode attenuation when $\eta = 0.76$. Normalized attenuations of fundamental mode are plotted as function of wavelength with different thickness of jacket tube. The rest of structure in the simulation remains the same.

From fig. 3.5 we can conclude that jacketing tube thickness barely has any effect on attenuation of fundamental mode of HC-NCF. Those unchanged attenuation curves can be explained by the very limited coupling between the core mode and mode in the jacketing tube due to the long spatial distance.

The function of a jacketing tube is mainly to provide mechanical protection for the fibre. The jacketing tube thickness cannot be too thin or it will lose mechanical robustness. The ratio range of t/D in the simulation is from 0.028 to 0.278 and corresponds to thicknesses as from 1μm to 10 μm. In the real fabrications, to maintain mechanical strength of the fibre, t is always bigger than 50 μm.

3.4 Effect of material absorption on fibre loss

In the simulated wavelength range, the silica glass is almost transparent to light and the material absorption can be almost neglected. However if we expand or reduce the fibre size for applications for other wavelengths, the effect of material absorption becomes substantial and important.

Silica glass becomes opaque in the ultraviolet spectrum below 200 nm and in the mid-infrared spectrum above 3000 nm due to electron transition absorption and phonon absorption respectively [2].

The effect of material absorption on the mode attenuation is simulated at a single wavelength. By adding an imaginary part to the silica refractive index, different material absorptions are added to the simulation. The relation between the material absorption and fundamental mode attenuation is plotted in fig. 3.6.

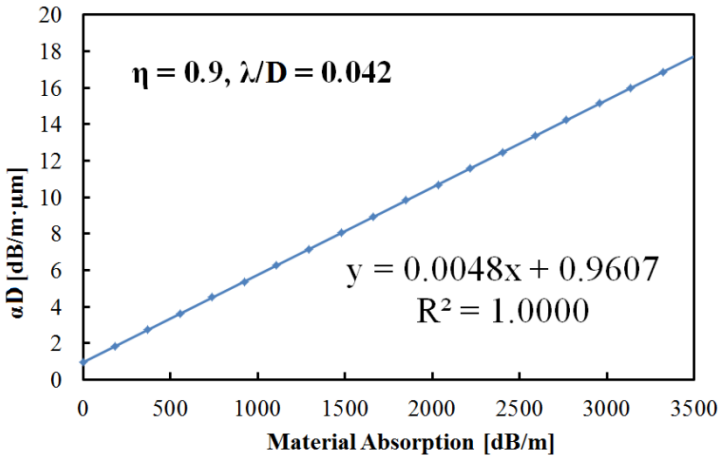

Fig. 3.6 Relation between the fundamental mode attenuation and material absorption when $\eta = 0.9$ and $\lambda/D = 0.042$. The slope of the linear fitting function is 0.0048.

Figure 3.6 shows a linear relationship between the material absorption and the final mode attenuation, as expected. In our stimulated model of HC-NCF, the total mode attenuation can be regarded as the addition of mode attenuation which is determined by the leaky waveguide property, and the attenuation caused by the material absorption. The slope of the fitted curve indicates how significantly the material absorption affects the total modal attenuation. With $D = 36$ μm in the model, the modal attenuation caused by the material absorption is 7500 times less than the material absorption itself. Such a small effect of material absorption on fibre loss is caused by the extremely small overlap between the core mode and silica material in the cladding (the negative curvature core wall may contribute to the much reduced overlap between the core mode and cladding material). Such a small effect of material absorption on fibre loss also implies that HC-NCF has the great potential in light transmission in the spectrum where fibre material becomes lossy and opaque.

3.5 Dispersion property

Mode dispersion is usually characterized by group-velocity dispersion (GVD) [1],

$$\mathrm{GVD} = -\frac{\lambda}{c}\frac{d^2 n_{eff}}{d\lambda^2} \qquad (3-6)$$

in which n_{eff} is the effective refractive index defined by eqn. (2-11).

n_{eff} is an scaling invariant parameter. Figure 3.7 shows simulated n_{eff} as function of wavelengths for different η. In the plot we can find that for $\eta = 0.5$ and 0.76, n_{eff} has sudden changes around the resonant wavelengths of the capillary wall and at other wavelengths, n_{eff} is rather smooth. For $\eta = 0.95$, n_{eff} is smooth and flat all over the spectrum and for $\eta = 0.5$, n_{eff} varies up and down due to the strong coupling with the cladding modes.

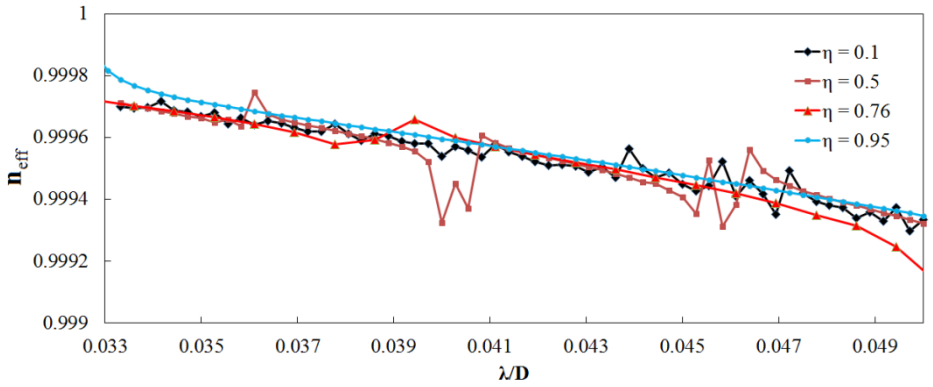

Fig. 3.7 n_{eff} as a function of wavelengths for different η.

Near the resonance wavelengths, the core mode and cladding mode couple with each other and n_{eff} experiences a sudden change due to anti-crossing. This effect can also be found in fig. 2.6. Far from the resonance n_{eff} mainly reflects the core mode property and is only determined by λ/D. For $\eta = 0.1$, we find that n_{eff} curves overlap fairly well with other curves. As in this condition, the loss of NCF maintains constantly high, according to Kramers–Kronig relation [4], the fluctuation of dispersion curve is not significant.

To study GVD of the core mode without interference from cladding, $\eta = 0.95$ is selected as the cladding barely changes the core mode dispersion in the wavelength range of interest. n_{eff} and normalized GVD curves are plotted in fig. 3.8.

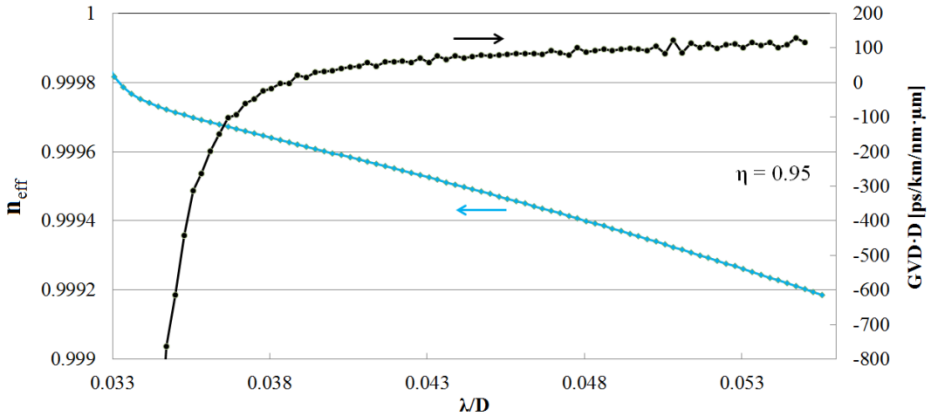

Fig. 3.8 n_{eff} and GVD curves as functions of wavelengths for $\eta = 0.95$.

From fig. 3.8 we can find that most of the GVD curve in the low loss spectrum stays in the anomalous dispersion region and exhibits low dispersion. According to the ARROW model prediction, the first resonance wavelength for $\eta = 0.95$ is $\lambda/D = 0.0323$ that locates on the left of the curve. As the wavelength approaches the resonance, GVD rapidly changes the dispersion sign and becomes bigger.

3.6 Conclusions

Chapter 3 presents the numerical simulation results of HC-NCFs by *Comsol*.

The simulations mainly focus on the loss properties of HC-NCF. In the simulation, the effects of capillary thickness, jacket tube, as well as material absorption are studied. To obtain broad and low loss transmission bands in HC-NCF, thin-capillary cladding should be always preferred according simulations. Although the loss due to the material absorption is 7500 times less, material absorption may still finally limit light transmission at extremely short and long wavelengths where the material becomes extremely lossy.

Simulations also confirm that the cladding strongly affect the core mode dispersion near the resonance wavelengths. For the rest of spectrum the mode dispersion is mainly determined by the leaky mode property, which has a low GVD.

Reference

[1] G. P. Agrawa, *Nonlinear fibre optics*, Chapter 1 (Elsevier, 2009).

[2] R. Kitamura, L. Pilon, and M. Jonasz, "Optical constants of silica glass from extreme ultraviolet to far infrared at near room temperature," Appl. Opt. **46**, 8118-8133 (2007).

[3] A. W. Snyder and J. D. Love, *Optical waveguide theory* (Chapman & Hall, 1983).

[4] Magnus Haakestad and Johannes Skaar, "Causality and Kramers-Kronig relations for waveguides," Opt. Express **1**3, 9922-9934 (2005)

Chapter 4 Fabrication of hollow core negative curvature fibre

Chapter 4 reviews the fabrication process of HC-NCFs and discusses the challenges in fabricating good quality HC-NCFs.

In section 4.1, the stack-and-draw technique, which is used to fabricate HC-HCFs, is illustrated in detail.

In section 4.2, the primary challenges of fabricating HC-NCFs are discussed There are maintaining uniformity along the fibre length and prohibiting degradation of the cladding structure. Both are inherent problems originating from the stack-and-draw technique.

4.1 Stack-and-draw technique

4.1.1 General procedures

In 1996 Knight et al. reported the first all-silica single mode photonic crystal fibre fabricated with the stack-and-draw technique [1]. The special optical properties of photonic crystal fibre greatly stimulated the development of specialty optical fibres. The stack-and-draw technique has been widely demonstrated with great success in the fabrication of specialty optical fibre in both laboratory and industry [2].

In the 1970's, the stack-and-draw technique was first reported in the fabrication of specialty optical fibre in *Bell laboratory* [3]. The stack-and-draw technique can be generally divided into the stacking process and the drawing process. Compared with other fibre fabrication methods, for example the vapour deposition method, the stack-and-draw technique is much more flexible. By stacking a preform with capillaries and rods of different sizes together, it can realize rather complex fibre designs including complicated geometric profiles and special refractive index distribution.

Figure 4.1 is a schematic to illustrate the procedures of the stack-and-draw technique used to fabricate HC-NCFs. All material used in fabrications presented in this thesis was F300 synthesized fused silica material from *Heraeus* which has a low concentration of OH^- group [4].

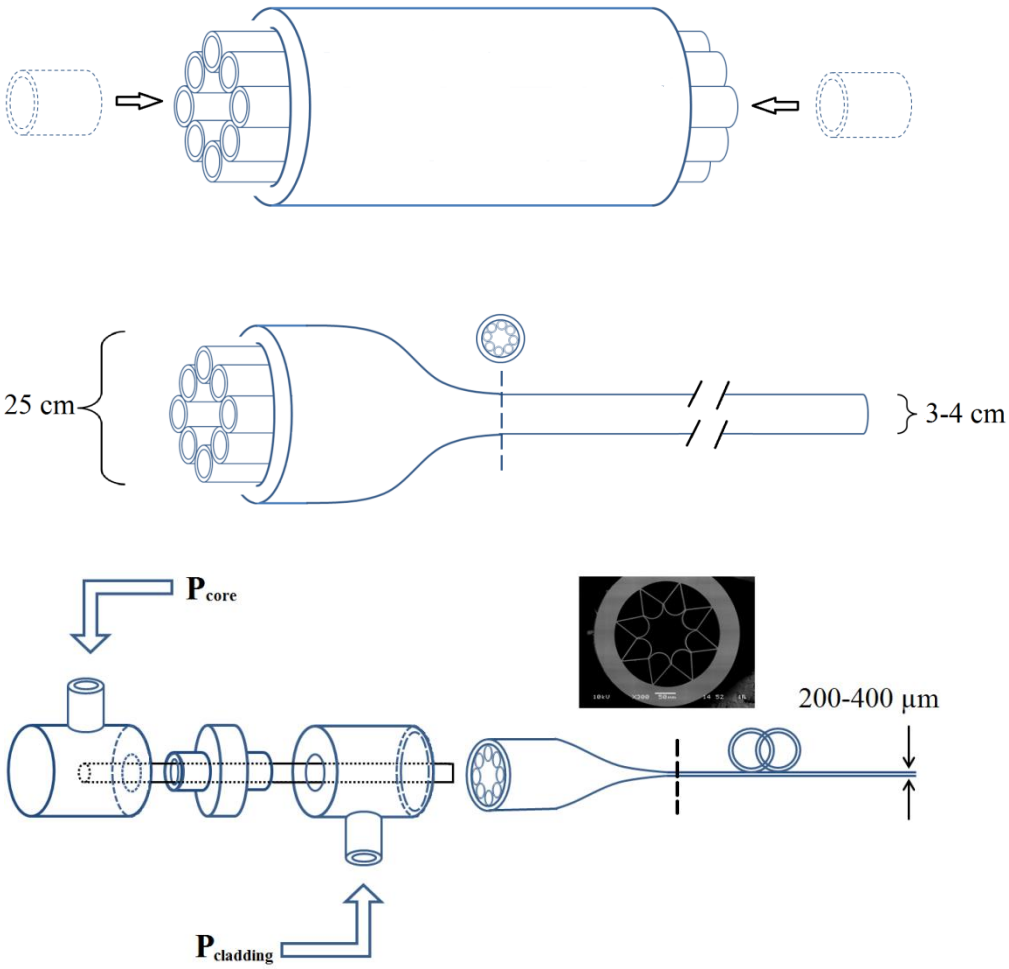

Fig. 4.1 Schematic of stack-and-draw technique to fabricate HC-NCFs. Top: stacking with capillaries. To maintain the cladding structure, two short capillaries (dashed line) are to insert to both ends as support. Middle: drawing of canes. The middle part of stack without supporting capillaries is drawn into canes of smaller diameter. Bottom: fibre fabrication from canes. Different pressures are applied to different regions of cane. Pressure difference is important to form the negative curvature core wall. The inset picture is a SEM image of typical NCF.

1) Stacking

Stacking (fig. 4.1 top) is used to build a macroscopical structure up with capillaries or rods of different sizes matching the fibre design. The initial capillaries and rods need to be drawn from raw silica tubes in advance. Once assembled, the whole stack is usually 20 – 25 cm in diameter. To fabricate HC-NCF, two short capillaries or rods always need to be inserted in the core region at the ends of the stack to support the cladding and prevent the stack from collapsing.

2) Drawing of cane

The cane is an intermediate preform which is drawn from the stack (fig. 4.1 middle). The cane is essentially a complete optical waveguide but on the millimetre scale. HC-NCF will be finally drawn from the cane rather than directly from the stack.

The drawing of cane is a necessary and important step in the fabrication of HC-NCF and other HCFs. It can avoid a dramatic scale change from stack in centimetres to final fibre in micrometres. According to the model of amorphous material under high temperature in fibre fabrication, a large drawdown ratio makes the fine structure (mainly air holes) very sensitive to fabrication conditions such as temperature, filled-in gas pressure and drawing tension [5]. Preventing the structure from deformation becomes more difficult in the large scale change [5]. As a result, drawing fibre from the smaller cane rather than a bigger stack is the key to obtain good quality HC-NCFs. In my fabrication of HC-NCF, the cane size is usually about 3 – 4 cm in diameter.

3) Drawing of fibre

The drawing process is illustrated in fig. 4.1 bottom.

In this stage, the cane is installed in a specially designed cane holder usually made of metal. This cane holder as shown in fig. 4.1 bottom is a device to fasten the cane to the fibre tower and apply pressurised gases (usually pure nitrogen) into the cane to maintain air holes from collapse in the drawing process. In this stage, the feed speed of the cane, the draw speed of the fibre, the furnace temperature and the gas pressure must be carefully adjusted or the fine structure of fibre can be easily deformed otherwise.

In the drawing stage, polymer material will be coated around the final fiber for protection and enhancement of the mechanical strength of optical fiber.

4.1.2 Integrity of canes

Obtaining a good quality cane is critical to obtain good quality HC-NCF. Suitable canes should be free from deformation of the structure, collapsed holes, stacking faults or defects. In fabrication of HC-NCF, the cane must have the cladding capillaries fused with each other and with the jacketing tube. The fusion between capillaries is to achieve a well-sealed core region from the cladding for the pressurisation in the next stage of fibre drawing. Any failure of fusion between the capillaries, or between the capillaries and jacket tube will cause the failure of the negative curvature core wall and break the symmetry of the fibre.

Figure 4.2 is a comparison between failed and successful canes and fibres drawn from them respectively. All the conditions of stacking and fibre drawing are identical. The cane in fig. 4.2 (1) has three capillaries out of touch with the jacketing tube as indicated by arrows. In the final fibre (fig. 4.2 (3)) that is drawn from it, the cladding becomes completely deformed. The cane in fig. 4.2 (2) is a successful one as every capillary in the cladding is in contact with the jacketing tube and the adjacent capillaries. The fibre (fig. 4.2 (4)) drawn from it exhibits great symmetry and uniformity. Measurements have demonstrated that, HC-NCF with low attenuation always has excellent symmetry and this is predominantly determined by the quality of the cane.

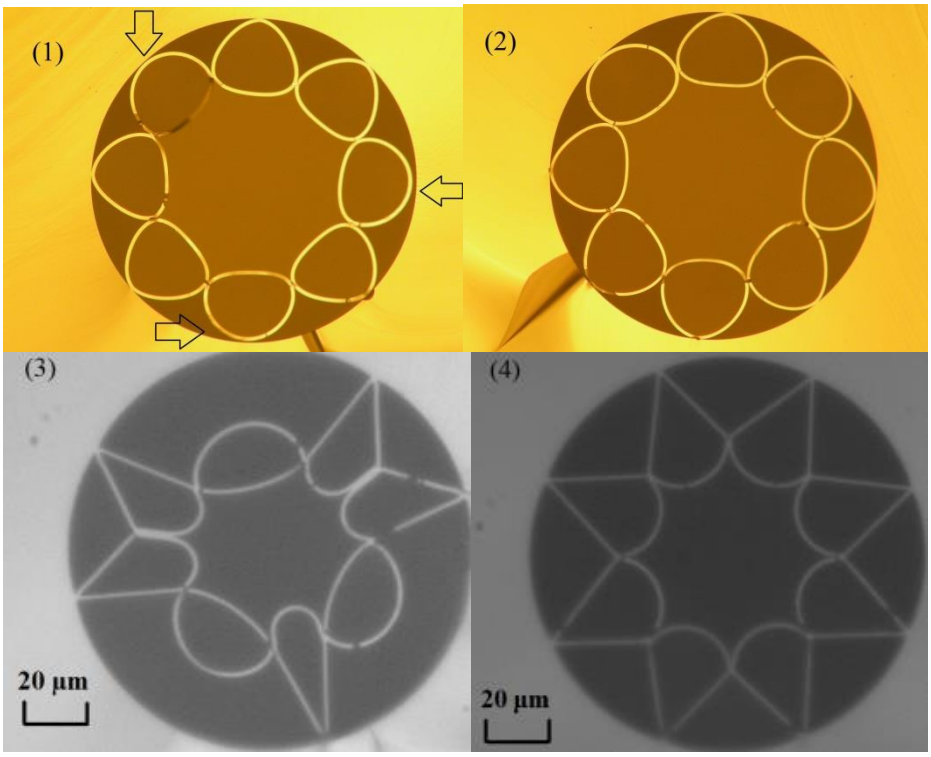

Fig. 4.2 Comparison between failed and successful canes and fibres drawn from them. (1) failed cane: arrows point out three defects where cladding fails touching the jacket tube. (2) successful cane: each capillary in the cladding well touches jacket tube and capillaries besides. (3) fibre drawn from the cane shown in (1). (4) fibre drawn from the cane in (2). Conditions of stacking and fibre fabrication are the same.

HC-NCF has a much simpler cladding structure than other specialty optical fibre such as HC-PBG. Although its simple structure makes stacking much easier, it requires that the cane has a high standard of fusion between capillaries in the cladding. And achieving such fusion is sometime a challenge in the fabrication of HC-NCFs. Surface tension is always against such contact between capillaries so that the fusion

between capillaries can be unstable along the length due to lack of support from the cladding structure. In fabrication, once the contact between the capillaries is insufficient, the capillaries will quickly shrink and finally collapse due to surface tension under high temperature. Once this happens, the integrity of cladding is almost impossible to recover unless external force is applied. As a result, to have good quality canes, the precise control of capillary size, and low fabrication temperature are critical.

1) Control of capillary size

From my experience in fabrication, less than 0.5 % variation in capillary diameter from design is necessary to fabricate a good cane. Within this limit, capillaries in the stacking can support each other tightly and this would guarantee the integrity of the cane. The capillaries drawn down for stacking are usually 3 - 4 mm in diameter, so the diameter variation of the capillary must be controlled within 15 - 20 μm.

In the real fabrication, the external diameter of capillary varies in length. Undersized capillary can cause failure of forming negative curvature core wall ultimately; however the oversized capillary can make the stacking extremely difficult. In stacking, capillaries are inserted in to a jacket tube one after another. The capillary is extremely easy to damage due to the friction if it is oversized at certain point along the length. Nevertheless, to obtain a good cane and fibre, undersized capillary is always less tolerated.

2) Low temperature fabrication

Besides the capillary size control, low temperature is also necessary to maintain the integrity of canes. At higher temperature, where silica glass has a less viscosity, surface tension can have a greater effect on the cladding structure and sometimes can cause capillaries in the cladding to collapse. At low temperature the viscosity of silica becomes higher which can help reduce the capillary deformation to some extent. In my fabrication furnace temperature is usually set between 1880 ℃ and 1920 ℃ for cane fabrication, which is a very low temperature in the silica fibre fabrication.

4.1.3 Formation of negative curvature core wall

Forming a negative curvature core wall in HC-NCF is challenging due to the effects of surface tension and low viscosity at high temperatures.

Above the glass transition temperature, as the temperature rise up, the viscosity of silica decreases. The surface tension then can more easily modify the fibre structure in spite of the viscosity. Air holes in the cane tend to collapse in the fabrication of HCFs which is a well-known effect. To form the negative curvature, external force must be applied in HC-NCF to counter the surface tension. This is achieved by applying the pressurized nitrogen gas into the cane during the fabrication. At the same time, the furnace temperature should be controlled as low as possible. Low temperature is helpful to increase the viscosity of silica material and prevent the fine structure from collapse.

1) Pressurisation

Figure 4.3 shows HC-NCFs fabricated in different pressurisation conditions. In fig. 4.3, (1) is the cane and (2), (3) and (4) are fibres drawn from the cane. In this fabrication, different pressures were applied to the core and cladding regions respectively as fig. 4.1 illustrates. The pressure in the core of the cane was applied by a capillary inserted in the core(as fig. 4.1 bottom) and the core pressure P_1 was controlled by channelling nitrogen gas into the core region by that capillary. The remaining area of the cane was uniformly pressurised via the cane holder by P_2. When $P_2 > P_1$, the core boundary is pushed from the cladding towards the core region so exhibits a negative curvature. A higher pressure difference would make a more curved core boundary. In the cladding, because the pressure is uniformly applied, all boundaries are straight. The pressure differences applied in fabrications of fibres (2), (3) and (4) were 8 kPa, 15 kPa and 45 kPa respectively.

The other fabrication conditions for the three fibres in fig. 4.3 were kept all the same. Furnace temperature was 1940 ℃. Feed speed was 65 mm/min and draw speed was 10.9 m/min. Drawdown ratio was about 20 times.

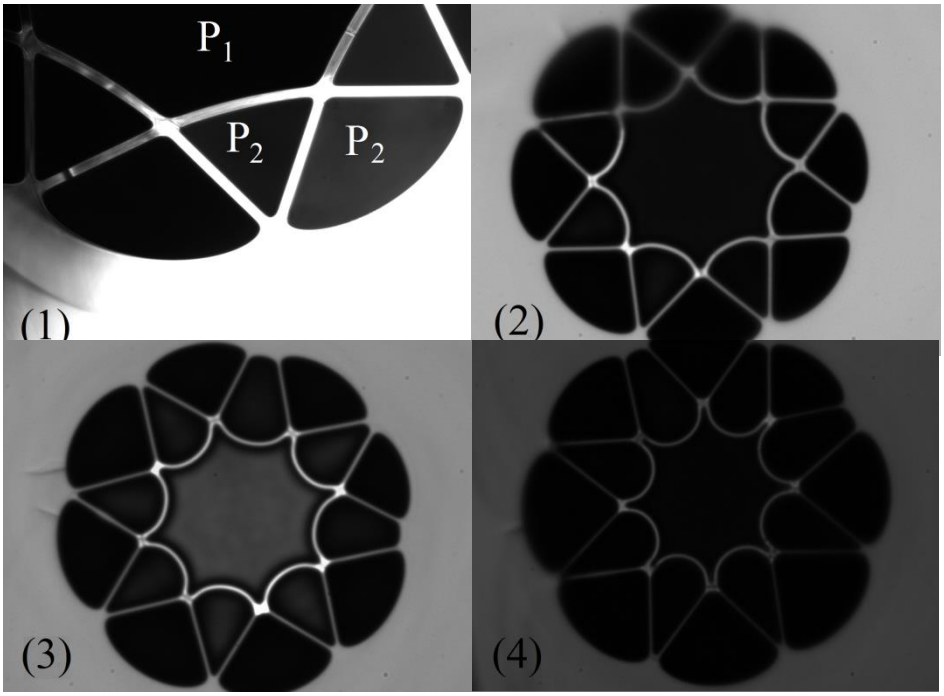

Fig. 4.3 Various the negative curvature core walls which are controlled by two different pressures in the core and cladding. (1) pressure P_1 is applied to core and P_2 is applied to cladding. $P_1 > P_2$ is necessary to form the negative curvature of the core wall. (2)(3)(4) are fibres drawn from cane in (1) and have various pressure differences as 8 kPa, 15 kPa and 45 kPa respectively. All the other fabrication conditions were the same.

Another pressurisation method is to control different regions of the cane independently by many pressurizing capillaries. Figure 4.4 (1) is the cane with three different pressures applied to different region inside. Pressure P_1 is applied to the core region via a capillary; P_2 in eight capillaries of the cladding is controlled via eight thinner gas-guiding capillaries and P_3 is applied to the remaining parts of the cane via the cane holder. Figure 4.4 (2) and (3) are fibres drawn from the cane in fig. 4.4 (1). To obtain negative curvature of core wall, P_2 must be highest of the three.

Many fibres were drawn with this method under different fabrication conditions and the two fibres in fig 4.4 (2) and (3) were typical ones selected. Although this method can keep the cylindrical shape of capillaries in the cladding the same as the model simulated in chapter 2, claddings or cores in those fibres were always found to be asymmetric.

In fabrications, the two-pressure drawing method is always preferred and was successful in fabricating high quality HC-NCFs.

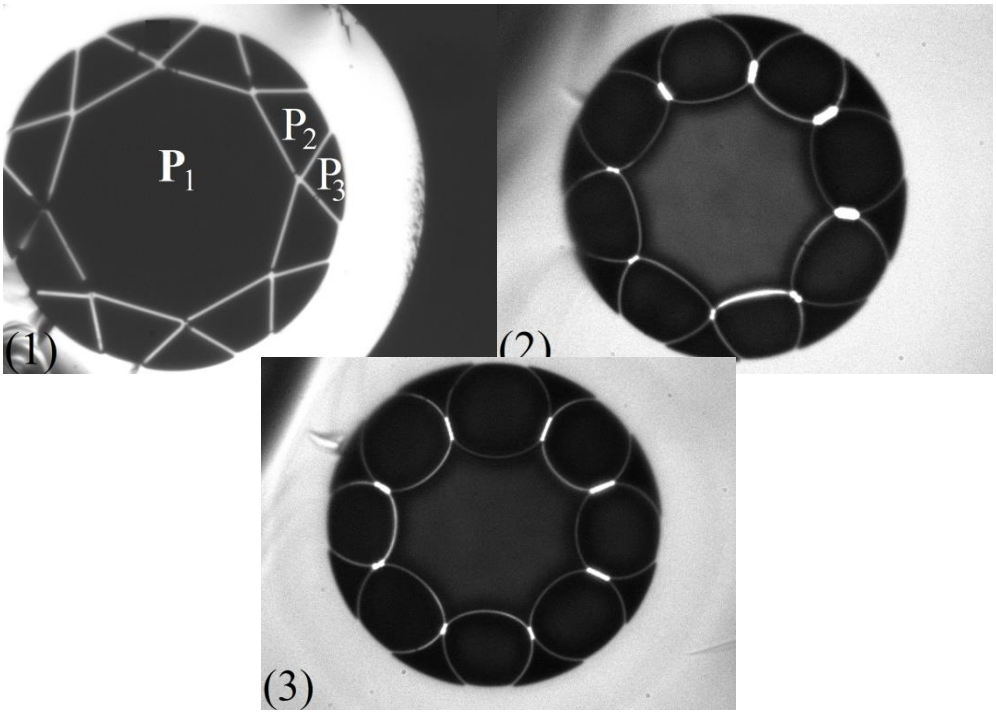

Fig. 4.4 HC-NCFs with three pressures to control curvature of the core wall. (1) cane: P_1 is applied to the core, P_2 is applied to the capillaries of the cladding and P_3 is applied to the remaining regions. P_2 is the highest pressure. (2) and (3) are two typical fibres drawn from cane in (1). The core and cladding in each fibre are asymmetric which are common to see in the fabrication with this pressurisation method.

2) High viscosity condition

Besides using pressurisation to counter surface tension, increasing the viscosity of the silica material can also reduce the effects of surface tension. This has been demonstrated as essential to form the negative curvature core wall in fabrications.

Figure 4.5 shows two hollow core fibres with failed core wall curvature. They were both fabricated with the two-pressure drawing method but under relatively high temperature above 1940 ℃. Even more pressure difference between the cladding and the core was applied, but the nitrogen gas simply pushed the flat cladding wall towards the core rather than helped to form the negative curvature.

From my experience, the recommended pyrometer reading for emergence of negative curvature of the core wall is between 1900 ℃ and 1920 ℃. Besides temperature, controlling the dwell time of the cane inside the furnace is also closely related with the thermal dynamics and plays an important role of obtaining the negative curvature core wall. Feed speed of the cane is important; a common feed

speed for HC-NCF of 300 μm in diameter should be faster than 50 mm/min while the drawdown ratio should stay below 15.

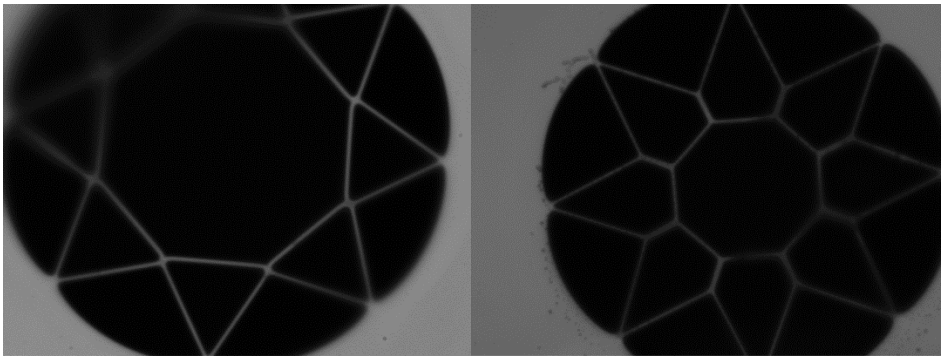

Fig. 4.5 Hollow core fibres with failed core wall curvature. Fibres on left and right were both fabricated under pressurisation but in a relatively high temperature above 1940 ℃.

4.2 Challenges in hollow core negative curvature fabrication

HC-NCF has almost the simplest cladding in HCFs however its fabrication is challenging.

4.2.1 Uniformity along the length

The guidance properties of light in HCF strongly depend on the cladding structure as discussed in Chapter 2. The uniformity of the cladding structure along the length of HC-NCF is important to maintain low loss transmission. As a result, the demanding of uniformity should be much more stressed for HC-NCF than for solid optical fibres. However because most areas in HC-NCF are full of air, the strength of HC-NCF against external perturbation in the fabrication is expected much lower than solid fibres and maintaining the uniformity of HC-NCF along the length is quite a challenge in fabrication.

1) Point defect and defect monitoring

One type of non-uniformity along the length in HC-NCF presents as point defects. Figure 4.6 shows transmission spectra of a HC-NCF by cutting certain lengths from the output end. The coupling condition at the fibre input end stayed the same during the whole measurement. Comparing the transmission spectra we can find that an impressive high loss feature in the 7 m long HC-NCF which was only caused by the first 30 cm length from the output end. After removing the first 30 cm piece, the loss dropped down to a much lower level.

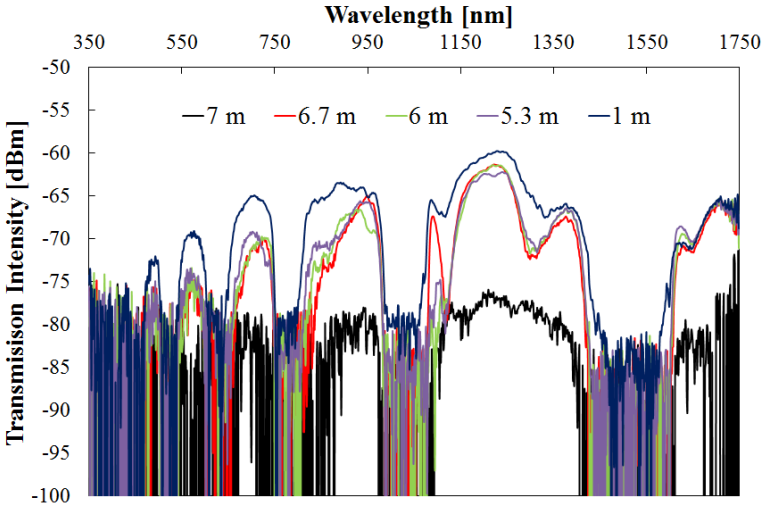

Fig. 4.5 Transmissions spectra from the HC-NCF at different lengths. The output end was cut shorter and the transmission spectrum was measured. The input end stayed the same.

Non-destructive identification of point defects in HC-NCF is difficult. The optical time-domain reflectometer (OTDR) is a common non-destructive method to obtain the uniformity information [6]. By recording the back scattered optical pulse signal, the point defect as a significant back scattering source in the fibre can be determined [6]. However the scattering properties of the non-uniformity along the length of HC-NCF are still unknown. Moreover, HCF length is usually much shorter than OTDR technique requires.

In the fabrication process, the current way to monitor the uniformity of fibre is to measure the external diameter of fibre by device in real time. This in-line method can supply feedback to system to adjust fabrication condition to maintain the uniformity of fibre. Figure 4.6 is a diameter record in a single draw of HC-NCF. The peaks in the plot represent significant and highly localised diameter variations of the fibre.

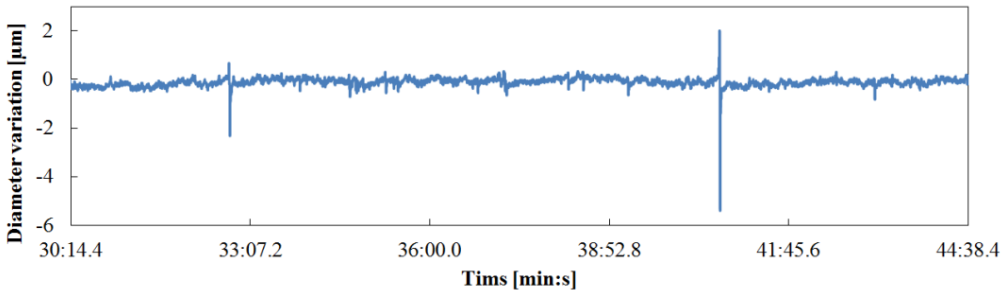

Fig. 4.6 External diameter variation of HC-NCF with time in a real fabrication.

The limit of diameter monitoring is that it cannot supply us with a detailed picture inside the fibre and it only works if the point defect in fibre causes a significant diameter variation.

2) Causes of non-uniformity

Any unstable factor in the fabrication can lead to the non-uniformity problem. Some of those factors are random and others are intrinsic in the fibre fabrication. Among them, uniformity of cane and stabilisation of pressurization are two main reasons for non-uniformity of HC-NCF, which can be improved in the fabrication.

The cane for fibre fabrication is usually 1 meter to 1.2 meter long. Over this length scale, the variation of external diameter is about $\pm$ 2 % which can be much improved by introducing feedback control. Although drawing process of cane is the same as capillaries, 0.5% error control is almost impossible for canes. As the drawdown ratio from the stack to the cane is smaller than the ratio from the tube to the capillary, the

total length of the cane is much shorter and the whole fabrication would be much quicker. A highly precise diameter control is a time consuming process and during this course, unqualified samples are to throw away. Since the cost of stacking make the cane much more valuable than elementary capillaries, $\pm$ 2 % diameter variation of the cane is usually acceptable.

The most effective way to improve the quality of cane is to make the canes smaller in size so that the increased drawdown ratio helps make more canes from one stack. But a smaller cane will make pressurisation more difficult and limit the final length of one complete piece of HC-NCF drawn from it.

4.2.2 Degradation of cladding

Figure 4.7 shows two HC-NCFs of two sizes under the optical microscope. The picture on the left is a HC-NCF of smaller size for the short wavelength transmission and the other on the right is a large fibre for the long wavelength transmission. Comparing these two fibres we can find that the fusion of capillaries in the cladding is greater in smaller fibres as indicated in the figure. The loss of smaller fibre was experimentally found to be higher than that of the larger fibre. And HC-NCFs with such degradation of cladding structures, especially for the short wavelength transmission, are always found with higher loss than expected.

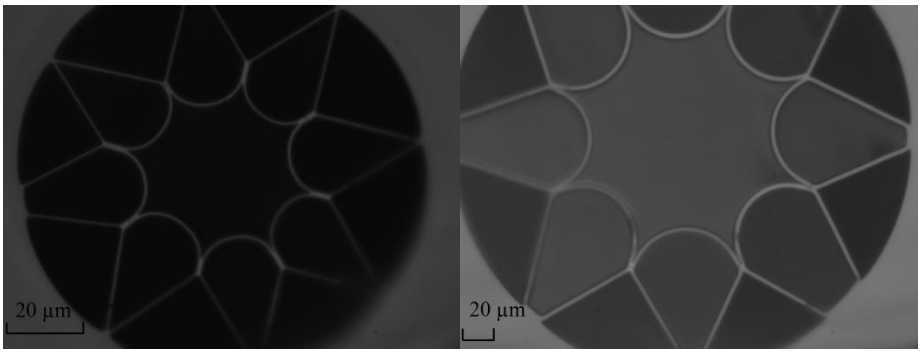

Fig. 4.7 Optical microscope pictures of HC-NCFs of different sizes. Fusion of capillaries in the cladding is greater in the smaller fibre.

The reason of degradation of cladding structure in the fabrication is complex. This phenomenon is rarely found in the fabrication of large HC-NCFs for the long wavelength transmission. Surface tension plays an important role here. Currently the best way to prevent the degradation is to use low temperature in the fabrication and shorten the dwelling time of the cane in the furnace. However, in the fabrication, it is found that such degradation always happens when the size of HC-NCF is below

certain dimension (core size smaller than 30 μm). The effect of degradation of cladding structure on HC-NCF loss will be discussed further in Chapter 5.

4.3 Conclusions

Chapter 4 explains the fabrication technique of HC-NCFs in detail and discusses the unsolved challenges of fabrication.

The stack-and-draw technique is the main fabrication method of HC-NCF, which can be generally divided into three steps which are stacking, drawing of cane and drawing of fibre. Integrity of the cane is a preliminary condition to obtain high quality HC-NCF. To form the negative curvature of the core wall, pressurisation and low temperature in fabrication are the most important requirements.

The challenges of making good HC-NCF are to maintain the uniformity along the length and prevent degradation of the cladding structure. Neither of these challenges has been completely resolved. By adopting new techniques in future the quality of HC-NCFs may be improved.

Reference

[1] J. C. Knight, T. A. Birks, P. St. J. Russell, and D. M. Atkin, "All-silica single-mode optical fiber with photonic crystal cladding," Opt. Lett. **21**, 1547-1549 (1996).

[2] J. C. Knight, "Photonic crystal fibres", Nature **424**, 847 (2003).

[3] P. Kaiser and H. W. Astle, "Low loss single material fibers made from pure fused silica," Bell Syst. Tech. J. **53**, 1021–1039 (1974).

[4] O. Humbach, H. Fabian , U. Grzesik, U. Haken, and W. Heitmann, "Analysis of OH absorption bands in synthetic silica," J. Non-Cryst. Solids **203**, 19-26 (1996).

[5] Y. Chen and T. A. Birks, "Predicting hole sizes after fibre drawing without knowing the viscosity," Opt. Mater. Express **3**, 346-356 (2013).

[6] M. K. Barnoski and S. M. Jensen, "Fiber waveguides: a novel technique for investigating attenuation characteristics," Appl. Opt. **15**, 2112-2115 (1976)

Chapter 5 Attenuation of hollow core negative curvature fibres

Chapter 5 presents characterisation of the attenuation properties of HC-NCFs.

Section 5.1 introduces the cut-back method which is used to measure the attenuation of HC-NCFs. Section 5.2 presents measurement results of the material absorption of F300 synthetic fused silica. This material was used to fabricate all the HC-NCFs discussed in this thesis.

Section 5.3 presents attenuation properties of HC-NCFs in different spectral regions. To explore the attenuation limit of HC-NCFs, many fibres were fabricated. Among them, nine HC-NCFs with the lowest attenuation (in the first band) in different spectral regions are selected and studied.

In section 5.4, the limit of attenuation of HC-NCFs is studied by analysing the minimum attenuations of the nine HC-NCFs presented in section 5.3. The analysis reveals different mechanisms governing the fibre attenuation property in different spectral regime.

5.1 The cut-back measurement

The cut-back measurement is the experimental method adopted in this thesis to experimentally obtain the attenuations of different HC-NCFs. Figure 5.1 shows a schematic of the cut-back measurement.

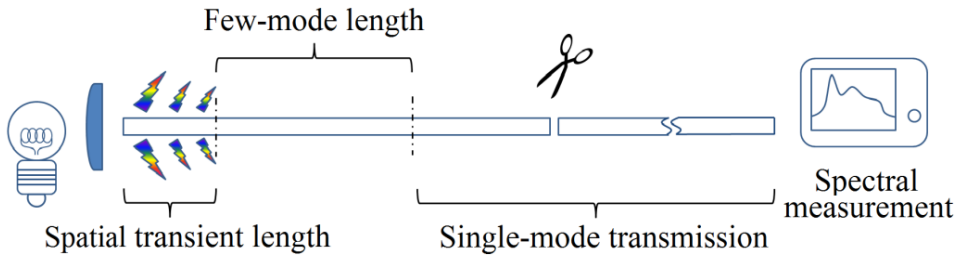

Fig. 5.1 Schematic of the cut-back measurement.

The cut-back measurement is relatively simple with straight-forward operational procedures. By measuring the transmission spectra of the fibre before and after the cut-back, the attenuation of the cut piece can be determined by

$$\alpha(\lambda) = \frac{1}{\Delta L} 10 log_{10} \left\{ \frac{P_2(\lambda)}{P_1(\lambda)} \right\} \qquad (5-1)$$

in which ΔL is the length of fibre removed, $P_1(\lambda)$ is the spectral power density measured at the output of the longer fibre before cut-back and $P_2(\lambda)$ is after the cut-back.

A dependable cut-back measurement needs attentions to the following aspects in the experiment:

1) The light source must have an emission spectrum matching the measurement method;
2) The mode excitation at the input end of the fibre should be stable and unchanged in the whole measurement;
3) The cut-back position must ensure the pure fundamental mode transmission in the cut piece of the fibre;
4) Extra loss from bending needs to be prevented.

5.1.1 Light source and detection

Excellent stability of spectral intensity over time, a broad spectral wavelength range and high brightness are the three basic requirements for the light source to excite modes in the fibre for the cut-back measurement.

Not all light sources are suitable for the cut-back measurement and the applicable light source must match the detection method well. In our experiments, all the spectra were measured and recorded by the optical spectrum analyser (OSA) *Ando AQ-6315A* (wavelength range from 350 nm to 1750 nm) and a scanning monochromator *Bentham TMc300* (wavelength range from 250 nm to 5.4 μm).

The spectral detection with OSA or the monochromator takes a certain time for signal integration, which is determined by the spectral range of interest, the resolution of the measurement, fibre losses and the intensity of the light source. One single spectral scan may take time from a few seconds to even an hour. During the measurement, the light source must show excellent stability of spectral intensity distribution over time on the scale of hours. Therefore many coherent light sources with fluctuating output power are not appropriate candidates for the cut-back measurement.

Inside the OSA and the monochromator, a lock-in amplifier system is usually used for detecting weak signals. Since the lock-in amplifier works under continuous or quasi-continuous signal condition, a pulsed light source with a repetition rate comparable with the chopper frequency of the lock-in system is not suitable for the cut-back measurement either.

As a result of these constraints, incoherent light sources are often preferred for cut-back measurements. In incoherent light sources, the stability of the emission spectrum in time is essentially determined by the stability of the driving current. With the help of the state-of-art electronic technology, the driving current of the incoherent light source usually can supply the cut-back measurement with satisfactory stability in the temporal domain. The other advantage of incoherent light sources is that they have much broader spectral ranges than the coherent light sources, although the average spectral power density cannot compete with lasers.

In this chapter, without specific illustration, all the cut-back measurements were performed by using a tungsten lamp which exhibits a broad spectrum from near-UV to mid-IR (5 μm). Figure 5.2 is the emission spectrum of the tungsten lamp measured by the monochromator from 2 μm to 5.4 μm. In fig. 5.2, the absorption features come

from certain molecules in the air: the features between 2600 nm and 2800 nm are from CO_2 and H_2O [1, 2], and the dip between 4200 nm and 4400 nm is from CO_2 absorption [1]. The small abrupt spectrum shift at 3600 nm is due to the change of the sorting filter wheel inside the monochromator.

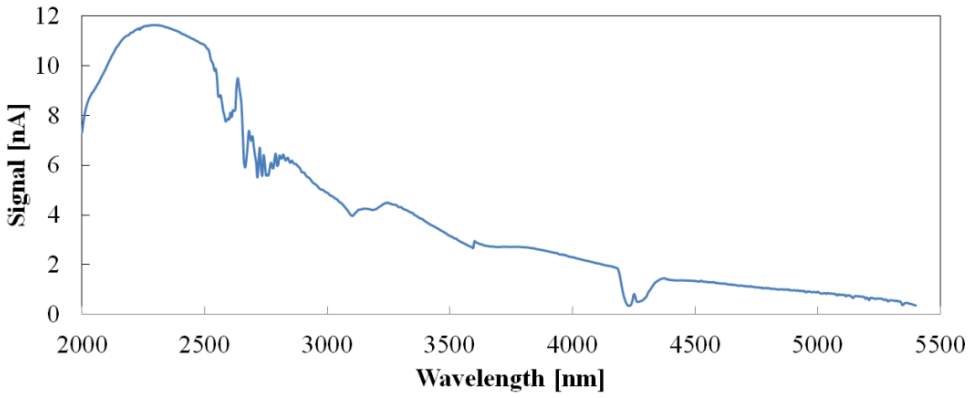

Fig. 5.2 Emission spectrum of the tungsten lamp measured by the monochromator. The absorption features between 2600 nm to 2800 nm are from CO_2 and H_2O in the air [1, 2], and the dip between 4200 nm and 4400 nm is from CO_2 absorption in the air [1]. The abrupt shift at 3600 nm is due to the filter changed in the scanning. Resolution of the measurement was 10 nm and step size was 5 nm.

The disadvantage of the tungsten lamp is its limited luminance especially at wavelengths above 3 μm in the mid-infrared spectral region. The luminance of the tungsten lamp, can be estimated by Planck's law [3]

$$\mathrm{I}(\lambda, \mathrm{T}) = \frac{2\mathrm{hc}}{\lambda^3} \frac{1}{e^{\frac{\mathrm{hc}}{\mathrm{kT}\lambda}} - 1} \qquad (5-2)$$

where $\mathrm{I}(\lambda, \mathrm{T})$ is the spectral luminance, in units of is energy per unit time (or the power) radiated per unit area of emitting surface in the normal direction per unit solid angle per unit wavelength; T is the temperature; h is the Planck constant; c is the speed of light and k is the Boltzmann constant.

Figure 5.3 is the calculated black body radiation at different temperatures. From fig. 5.3 we can find that a significant increase of temperature cannot effectively improve the spectral intensity in the mid-infrared region beyond 3 μm. The numerical aperture of HC-NCF is much smaller than a conventional solid core fibre. If we assume the numerical aperture of HC-NCF is 0.04 then approximately $0.08^3/4\pi$ of the total power of lamp intensity can be coupled into HC-NCF. Detectors for mid-infrared wavelengths often have a much lower responsitivity than those designed for visible or near infrared wavelengths. Hence the weak intensity of the broad band light

source is always a problem of the cut-back measurements of HC-NCFs in the mid-infrared spectral region.

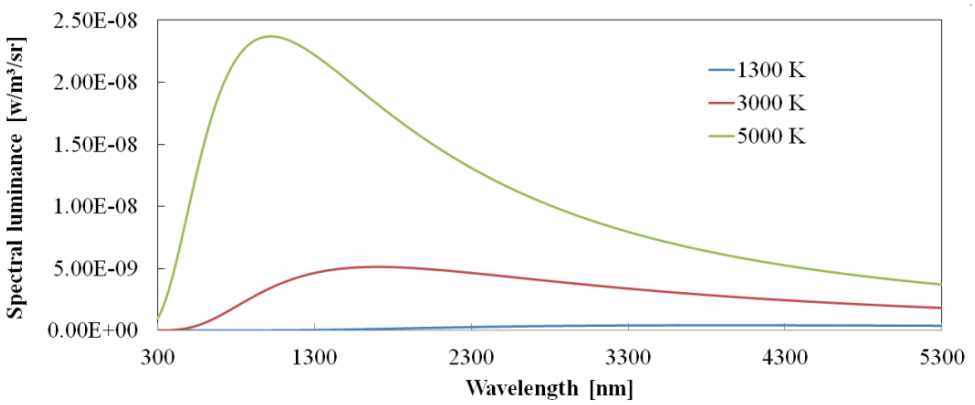

Fig. 5.3 Calculated black body radiations under different temperatures.

5.1.2 Coupling between the light source and fibre

Another difficulty in the cut-back measurement of HC-NCFs is the interference from the cladding light. With free space coupling at the fibre input end, light propagating in the free space is directly shone on to the fibre end, so both the cladding and core of the fibre are illuminated. In the index guiding fibre, e.g. a single mode fibre, light in the cladding quickly leaks away because of the smaller refractive index of the cladding and absorption from the coating material. In HCFs, the cladding, which is made of solid material, always has an effective refractive index higher than the core, so the cladding itself can be regarded as an independent index guiding waveguide. In the cut-back measurement of HCF, the suppression of the cladding light is therefore a pre-condition for a reliable measurement.

There are two common ways to solve the problem of cladding light interference. One is to use a lens to image the lamp filament onto the core of fibre so that the coupling to the cladding will be reduced. The other way is the fibre-butt coupling method as fig. 5.4 illustrates. One end of a single mode fibre (SMF) is used to collect the light from the lamp and the other end of the fibre is moved as close to the core of the HCF as possible. To avoid coupling light to the cladding, the core of the SMF need to be adjusted and aligned with the core of HC-NCF carefully.

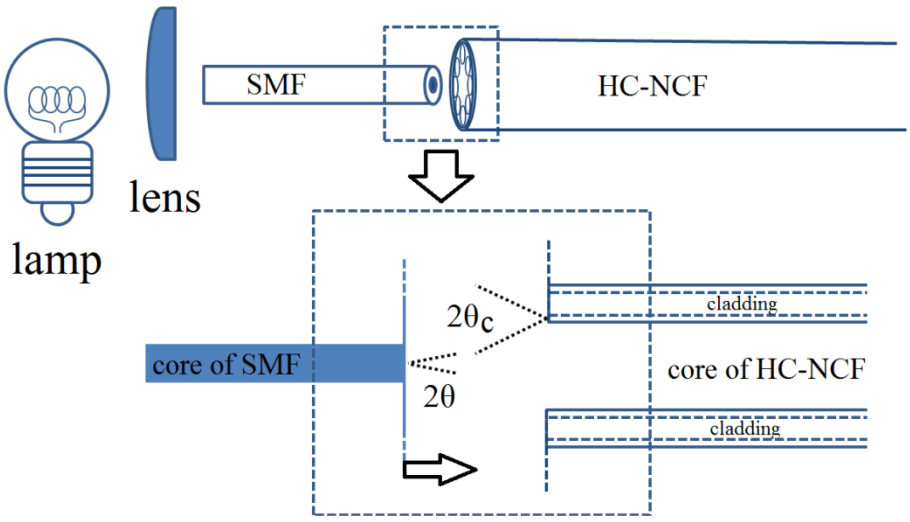

Fig. 5.4 Schematic of the fibre-butt coupling method. A SMF is used to collect the light from the lamp at one end and the other end is moved as close to the core of the HC-NCF as possible. To avoid cladding coupling, the cores of SMF and HC-NCF need to be aligned carefully.

The ability of the index guiding fibre to collect light is usually characterised by θ_c, known as the critical angle. When the incident angle is smaller than $\theta_c$the incident coupled light can always satisfy TIR and propagate in the fibre,

$$\theta_c = arcsin(\mathrm{NA}) \qquad (5-3)$$

where NA is the numerical aperture of fibre.

In HC-NCF, the cladding has a much larger numerical aperture than standard single mode fibre because there is a large refractive index difference between the air and solid material. For the silica cladding of HC-NCF, the numerical aperture of the silica cladding is above 1, but SMF-28 only has the numerical aperture of 0.14. In this situation, the cladding is able to receive incident light from all angles reaching the cladding end. The way to avoid the coupling is to make a transversely spatial mismatch between SMF28 and HC-NCF. The transverse spatial mismatch can greatly reduce the light coupled into the cladding from the end of fibre. Fibre-butt coupling is a fast and convenient way which is usually preferred in the cut-back measurement of large core HCFs.

The disadvantage of the butt coupling method is the low coupling efficiency. To avoid the cladding mode excitation, the core of SMF28 should be smaller than the core of HC-NCF. The mismatching of the core areas between the single mode fibre and HC-NCF can limit the coupling efficiency of fibre-butt coupling. In contrast, the

lens coupling method can achieve mode area matching by carefully choosing the magnification, but then the coupling efficiency will suffer from the very strict incident angle requirement arising from the small numerical aperture of HC-NCF. This critical requirement brings great difficulty in the fibre coupling. Also, the lens coupling is a dispersive coupling method, and the coupling efficiency therefore varies at different wavelengths. In my work the fibre-butt coupling method is usually preferred for the cut-back measurements.

The cladding light interference can be ignored when the silica material exhibits high loss. At those wavelengths, the free spacing coupling would replace the fibre-butt coupling as most of the light coupling in the cladding will quickly be absorbed by the silica material and cannot interfere with the cut-back measurement any more. No cladding light can be found transmitting even after a very short piece of fibre under the free space coupling. So, any power, which can be detected after transmission of a piece of HCF at those wavelengths, must then come from the air core rather than the absorptive cladding.

5.1.3 Cut-back position and cut-back length

As fig. 5.1 shows, the length of HC-NCF can be qualitatively divided into 3 cascaded regions due to the mode properties.

The first part starting from one end, where all the modes in the fibre are excited by the light source, is the transient region. This concept is borrowed from the conventional mode theory for the index guiding fibre [4]. In this length, the radiation modes rapidly decay along the fibre leaking energy to the external environment through the cladding. In the conventional mode theory, this length can be estimated by the formula [4]

$$z_0 = \frac{\rho}{2\theta_c} exp(V/2) \qquad (5-4)$$

in which ρ is core radius, θ_c is the critical angel and V is the normalized frequency.

In HC-NCF, this formula needs to be rewritten accordingly but it may still help us estimate the length scale of spatial transient region of HCF. If we assume that the numerical aperture (NA) of HC-NCF is 0.04, and the core radius is about 40 μm, the transient length is about 2.7 mm at a wavelength of 3 μm. The transient length increases rapidly with increasing NA. When NA =0.1, for the same wavelength and

core diameter, we have z_0 = 0.434 m. Usually in HC-NCF the numerical aperture for the fundamental mode is small [5], and this implies a short transient region starting from the excitation end of the fibre. $z_0 \leq 0.5$ m is considered here as a reasonable length limit of the spatial transient region for HC-NCFs.

After the spatial transient region follows the few-mode transmission region. In this region, besides the fundamental mode, high order modes propagate with much lower attenuation than the radiation modes. The length of this region is totally determined by the attenuation level of high order modes. After this length, because high order modes are strongly attenuated, the residual energy of light will be mainly carried by the fundamental mode and propagate further along the fibre length. Kolyadin and his colleagues experimentally determined that the few-mode length plus the transient length is less than 3 m in their silica HC-NCF at 3.39 μm [6].

In our cut-back measurements, the residual length of HC-NCF after the cut-back was always longer than 3 m to make sure that the cutback measurement results reliably reflect the attenuation of the fundamental mode in HC-NCF and no higher order modes could interfere with the measurement. In the near infrared wavelength range, cameras were always used to monitor the output of the fibre to identify the mode profile before and after the cut-back in experiments.

5.1.4 Preventing bending loss during the cut-back measurement

Bending loss is an important factor which can perturb the accuracy of the cut-back measurement. In a reliable cut-back measurement, the cut fibre must exceed a certain length to make sure that enough power difference can be detected before and after the cut-back. A significant power difference can reduce measurement errors caused by uncertain and accidental factors in the experiment. Usually 3 dB is an appropriate power difference in the cut-back measurement; however this requires the cut fibre length to be at least 30 m for a 0.1 dB/m attenuation level. The ideal way to lay such long fibre on the optical bench during the cut-back measurement is to put it straight, but it is almost impossible due to lab space limitations. Usually, a long fibre has to be wound in loops. A large loop diameter is necessary to prevent bend losses. The loop diameter in my cut-back experiments in this chapter was always greater than 1 m.

5.2 Material absorption

The HC-NCFs presented in this thesis are all fabricated with F300 synthetic fused silica glass from *Heraeus* [2]. Fused silica, the most common optical fibre material, exhibits extraordinary mechanical and chemical durability. In the visible and near infrared wavelength ranges, fused silica is almost transparent. But due to the phonon absorption, the application of fused silica is limited by its high attenuation (above 60 dB/m) at the wavelengths longer than 3 μm [2]. The material absorption data of F300 supplied by the manufacturer is in the wavelength range below 3.5 μm [2]. As our HC-NCFs have achieved low attenuation transmission at the wavelengths above 4 μm, it becomes necessary to extend our knowledge of F300 absorption to this wavelength range.

5.2.1 Experiment

Figure 5.5 is the schematic of the experiment to measure F300 absorption. A Tungsten lamp was used as the broadband light source. Three silica slices were cut from one F300 rod as samples to measure in the experiment. They were 170 mm, 28 mm and 2 mm thick respectively. The two ends of each piece were polished.

In the measurement, the distance between the sample and the slit of monochromator (entrance of the monochromator) was longer than 1 m. The aim of this is to avoid multi-path transmission of light in the silica sample by cylindrical side reflection. The material absorption was calculated based on the transmission spectra recorded by the monochromator.

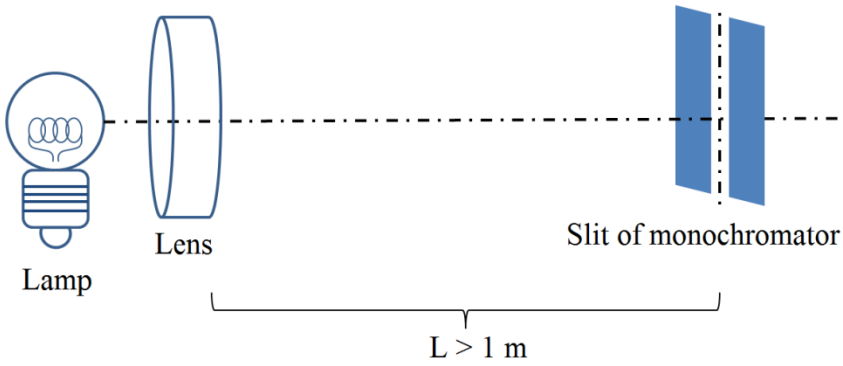

Fig. 5.5 Schematic of the silica material absorption measurement. A tungsten lamp was used as the light source. The distance between the silica sample and the slit of monochromator was longer than 1 m to guarantee the paraxial incidence.

5.2.2 Results and discussions

Figure 5.6 shows three transmission spectra through the 170 mm silica sample. The position and orientation of the sample were slightly changed for each spectral scan in the measurement. The positions of the lamp and monochromator remained unchanged during the whole experiment. The resolution of the monochromator was 10 nm and the scanning step size was 5 nm. The original data is plotted in the top of fig. 5.6 and on the bottom are transmission curves normalized by the spectral intensity at 2 µm.

In fig. 5.6 top, it can be seen that the transmissions of the light through the silica sample varies as the sample is moved. However, in fig. 5.6 bottom, we can find that the three normalized curves overlap after 2850 nm.

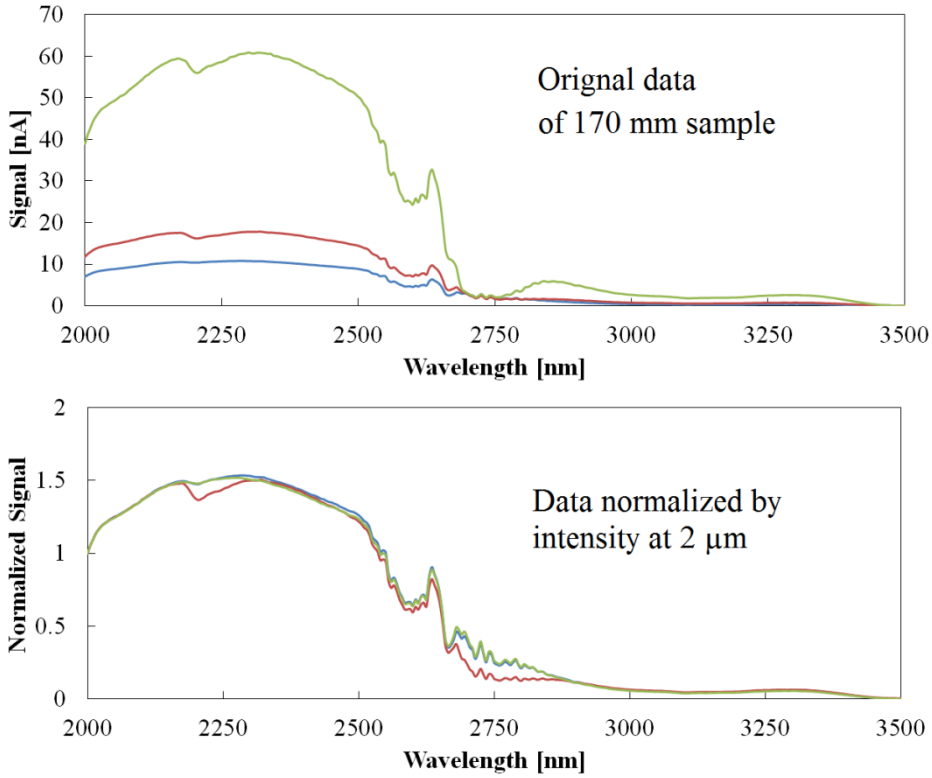

Fig. 5.6 Original transmission spectra through 170 mm silica sample and normalized spectra by the intensity at 2 µm. Absorption features between 2500 nm and 2900 nm come from CO_2 and H_2O absorption [1, 2]. OH^- groups in the silica could contribute to the absorption peaks in this spectral range.

The refractive index of silica changes less than 1 % between 2 µm and 4 µm [7]. Under the normal incidence assumption, the reflection at the sample end is almost the same for all the wavelengths between 2 µm and 4 µm. The multi-path transmission inside the sample mainly contributes to the variations of the transmission spectra. The off-paraxial light at certain angles can enter the slit of the monochromator by reflection of the cylindrical sides. This can greatly enhance the detected signal

strength in the monochromator. Normalisation can help reduce the multi-path effect. The multi-path effect will finally disappear as the sample thickness decreases, which is demonstrated in fig. 5.7 in the thinner silica sample.

Absorption features between 2500 nm and 2900 nm come from CO_2 and OH^- absorption [1, 2]. Both molecules in the air and OH^- groups in the silica could contribute to losses in this spectral range.

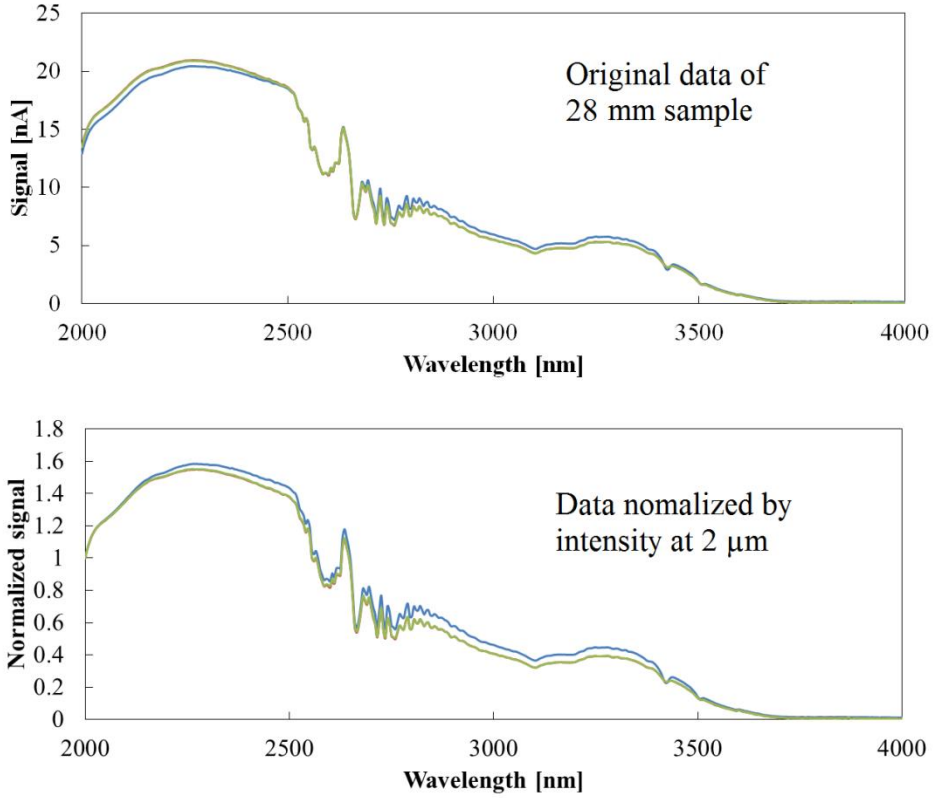

Fig. 5.7 Original transmission spectra through the 28 mm silica sample and spectra normalized by intensity at 2 μm. Absorption features between 2500 nm and 2900 nm come from CO_2 and H_2O absorption [1, 2]. OH^- groups in the silica could contribute to losses in this spectral range.

Figure 5.8 shows the silica material absorption spectra calculated by comparing the normalized transmission spectra through 170 mm, 28 mm and 2 mm samples with the normalized emission spectrum of the tungsten lamp in fig. 5.2. In the short wavelength range from 2800 nm to 3450 nm in fig. 5.8 (2), the material absorption calculated from the 170 mm thick sample is higher than from the 28 mm thick sample. But they ultimately overlap between 3450 nm and 3500 nm. After 3500 nm, the silica absorbs all light travelling in the 170 mm sample. Since a longer sample can give a better

accuracy, the calculated material absorption result from 170 mm sample is preferred as the final material absorption of F300 from 2800 nm to 3500 nm.

In the wavelength range above 3500 nm, we can find that absorption curves from the 28 mm sample and the 2 mm sample completely overlap between 3500 nm and 3600 nm. After 3600 nm due to the absorption, no transmission can be detected through 28 mm sample (fig. 5.7). As a result, the calculated material absorption result from 2 mm sample is preferred as the final absorption of F300 in the spectral range from 3500 nm to 4800 nm.

Figure 5.9 gives the final material absorption of F300 synthetic fused silica material from 2800 nm to 4800 nm. From fig. 5.9 we can find that silica absorption increases rapidly after 3500 nm and at 4 μm the absorption nearly reaches 900 dB/m. Although, according to the simulation results in chapter 3, the loss caused by the solid material absorption in HC-NCFs is tiny, the high material absorption would still be expected to dominate the attenuation level of HC-NCF in the long wavelength range above 3.5 μm.

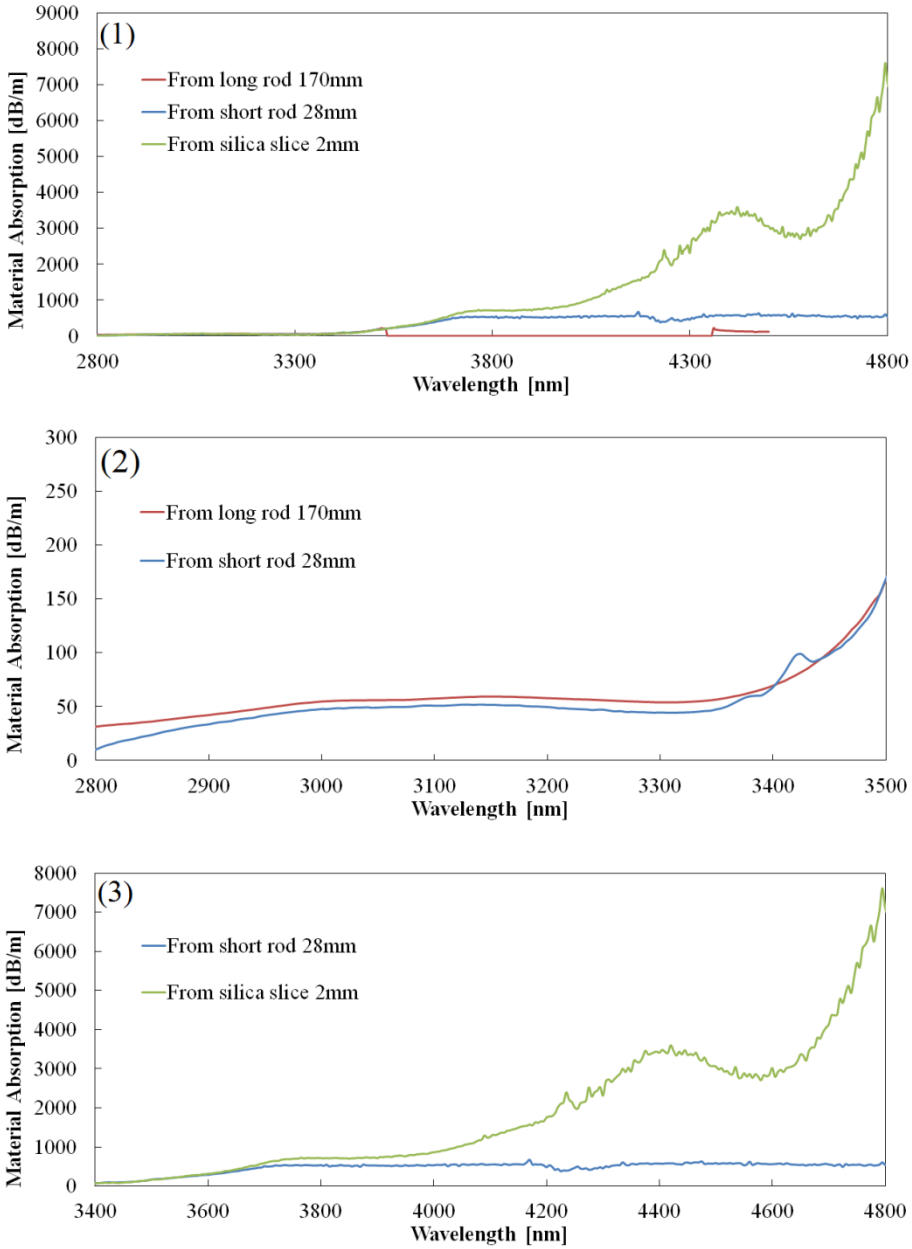

Fig. 5.8 Silica material absorption calculated from transmission spectra of the 170 mm, 28 mm and 2 mm thick silica samples, and emission spectrum of the tungsten lamp. (1) all absorption curves plotted together; (2) comparison between calculated absorptions from the 170 mm and 28 mm silica samples between 2800 nm and 3600 nm; (3) comparison between calculated absorptions from the 28 mm and 2 mm silica samples between 3400 nm and 4800 nm.

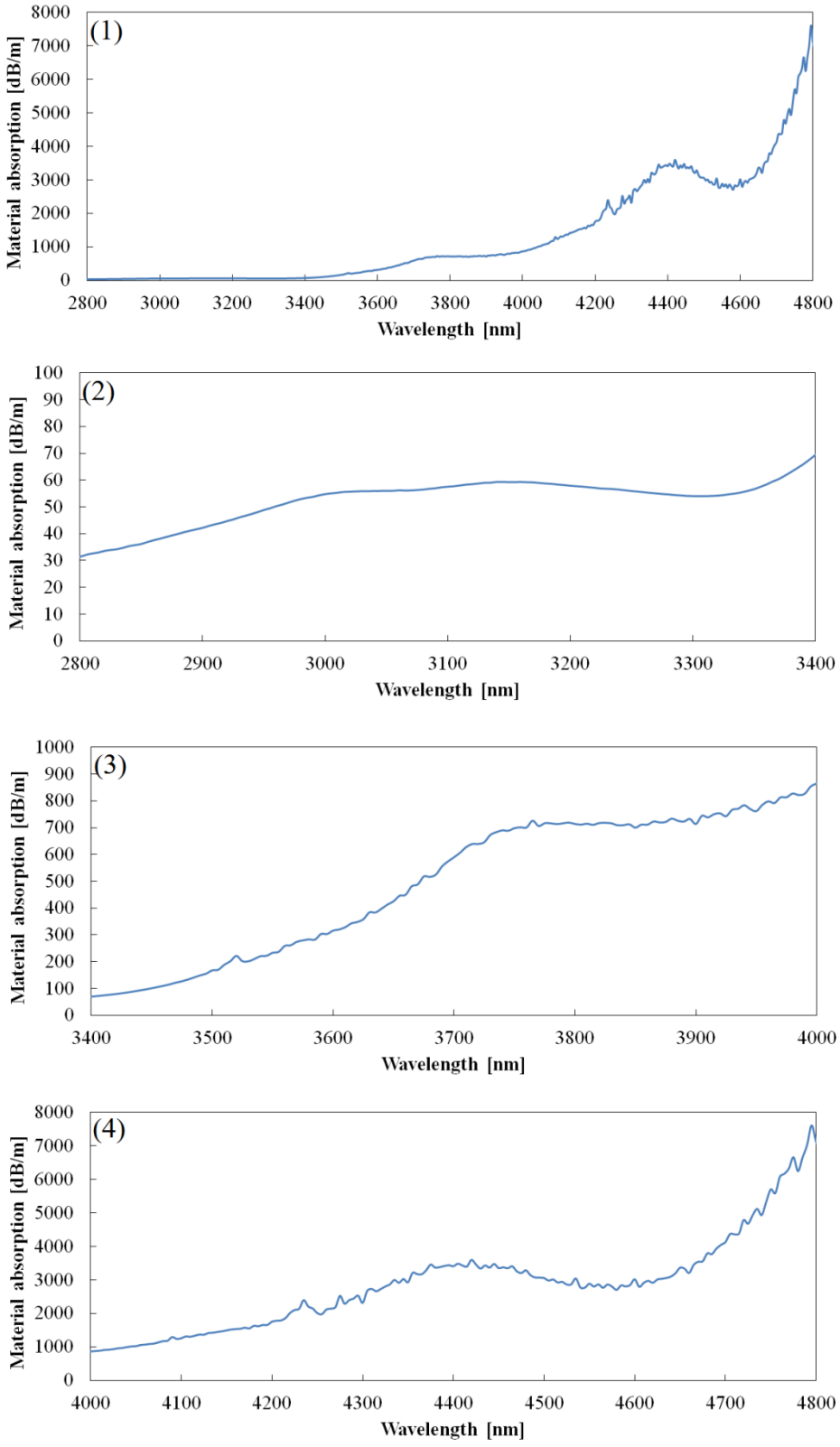

Fig. 5.9 Final F300 synthetic fused silica material absorption from 2800 nm to 4800 nm. (2) (3) and (4) are zoomed-in regions of (1).

5.3 Attenuations of HC-NCFs in the first transmission band

As fig. 3.5 shows, HC-NCF features multi-band transmissions. The band edge can be approximately determined by the ARROW model [9] and the first band in HC-NCF always has the broadest transmission bandwidth. The study of HC-NCF in this section mainly focuses on the attenuation properties of the first band.

To study the attenuation properties, more than 50 HC-NCFs of different dimensions have been fabricated and measured. Nine of HC-NCFs are selected and presented here which have the lowest attenuations in the first bands in their own wavelength ranges. Fig. 5.10 shows these nine first bands together spanning the infrared spectrum from 800 nm to 4500 nm. And the lowest attenuation measured is 24 dB/km at the wavelength of 2400 nm. Fig 5.11 shows the images of these nine HC-NCFs taken by optical microscope and scanning electron microscope.

In fig. 5.10, different gas absorption peaks can be found from 2600 nm to 4500 nm. HCl molecules in the core of fibre (originating from Cl^- in F300) result in the rotational-vibrational absorption features between 3200 nm to 3700 nm [8]. CO_2 molecules in the air cause absorption between 4200 nm and 4400 nm [1]. Absorption lines of CO_2 and H_2O molecules overlap between 2600 nm and 2900 nm [1, 2]. The OH^- groups in the silica can also contribute to losses in this spectral range.

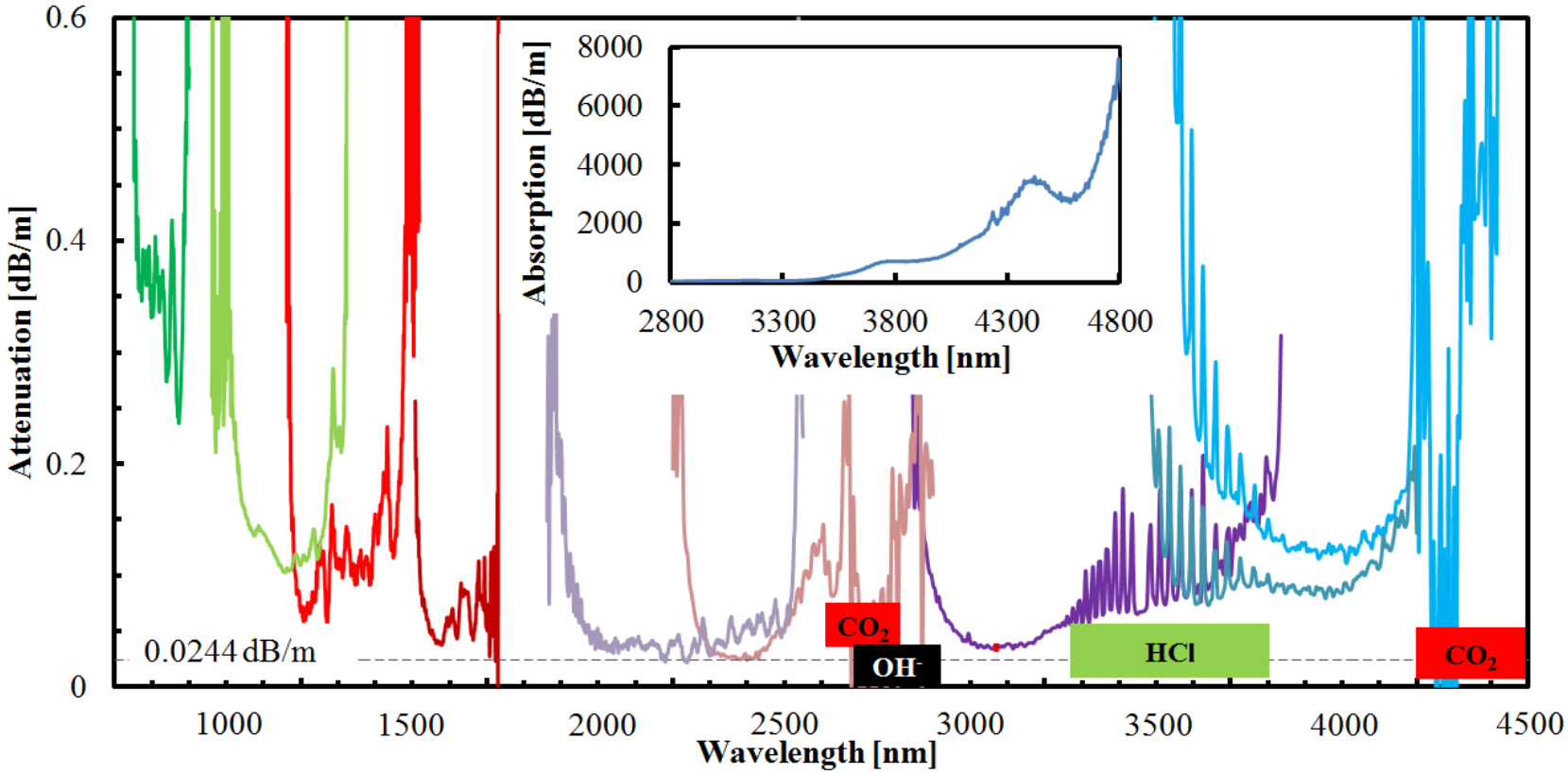

Fig. 5.10 Measured attenuation curves of the fundamental mode in the first transmission band in 9 different fibres. The absorption features between 3200 nm and 3700 nm are from HCl molecules in the fibre core [8], and between 4200 nm to 4500 nm are from CO_2 molecules [1]. Gas-borne CO_2 and H_2O molecules and OH^- in the silica material contribute to the absorption feature between 2600 nm to 2900 nm [1, 2]. Inset: Measured material absorption of F300 synthetic fused silica used as the fabrication material.

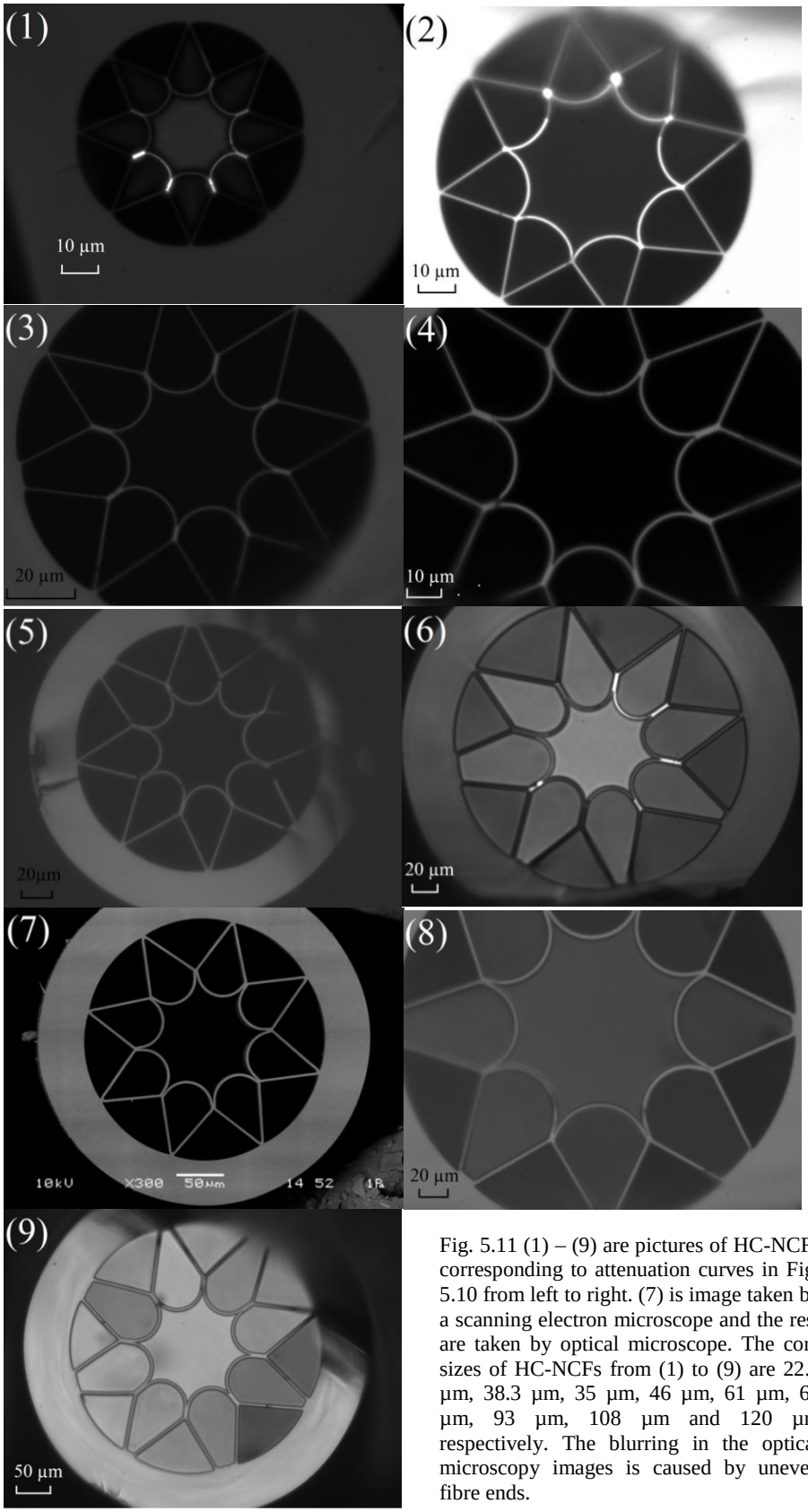

Fig. 5.11 (1) – (9) are pictures of HC-NCFs corresponding to attenuation curves in Fig. 5.10 from left to right. (7) is image taken by a scanning electron microscope and the rest are taken by optical microscope. The core sizes of HC-NCFs from (1) to (9) are 22.5 µm, 38.3 µm, 35 µm, 46 µm, 61 µm, 61 µm, 93 µm, 108 µm and 120 µm respectively. The blurring in the optical microscopy images is caused by uneven fibre ends.

5.3.1 The first band between 3 µm and 4 µm

Figure 5.12 shows the attenuation spectrum measured by cut-back of the HC-NCF with the first transmission band in between 3 µm and 4 µm (NCF (7) in fig. 5.11). The total fibre length in the measurement was 83 m which was cut back to 3.1 m. The resolution of the monochromator was set to 10 nm. As fig. 5.12 shows, the lowest attenuation was measured to be 34 dB/km at 3050 nm, and the low-loss band spanned over 900 nm from 2900 nm to 3850 nm. A second measurement in which the fibre was cut from 79.9 m to 2 m gave a similar minimum attenuation of 32 dB/km at 3050 nm.

In the cut-back, the free space coupling method was adopted and one of the fibre ends was put as close to the tungsten lamp envelope as possible. Due to the high absorption of silica above 3 µm, light in the cladding vanished quickly so that the measured attenuation was accurate and reliable. However, for the shorter wavelengths between 2 µm and 2.45 µm, the cladding light may influence the measured attenuation in the condition of the free coupling method.

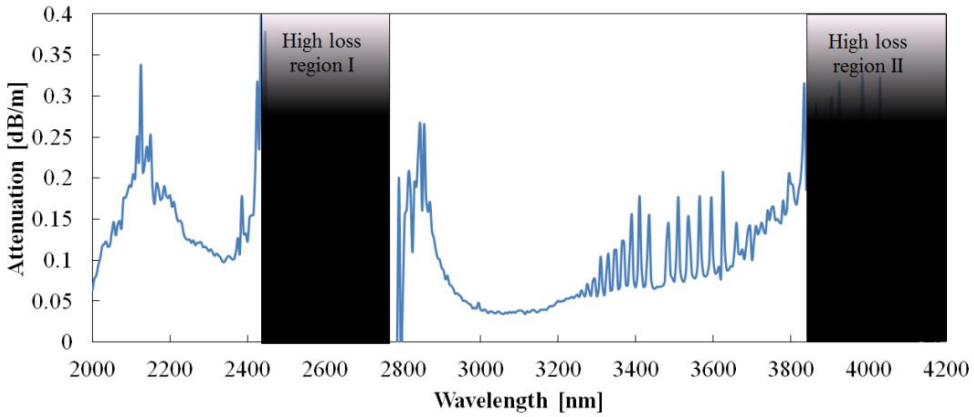

Fig. 5.12 Measured attenuation spectrum of HC-NCF (7) in fig. 5.11 with the first band in between 3 µm and 4 µm. No transmitted signal could be recorded in either of the high loss regions. Due to the potential perturbation from the cladding light, the attenuation of the second band between 2 µm and 2.45 µm was not reliable.

In the attenuation spectrum beyond 3800 nm (high loss region II), no light could be detected over the full 83 m of fibre, although a shorter length of fibre demonstrated the longest wavelength transmitted up to 4 µm. We attribute the band edge at the long wavelength to the rapid increase in the absorption of silica in this spectral range.

The other high loss region appears from 2500 nm to 2800 nm (high loss region I). Within this band we could not reliably record a transmitted signal even for shorter

fibre lengths. This region overlaps with known CO_2 and H_2O molecules absorption bands [1, 2]. However, the very high attenuation in region I should not be due to CO_2 or H_2O absorption, as the cutback measurement was performed following the fabrication, and most of transmitted light would propagate in the nitrogen-filled core (because of pressurisation in the fabrication). Instead, I attribute it to the high leaky loss near a resonant wavelength of the core wall – which coincides with the molecular absorption in this wavelength range.

According to the ARROW model [9] the resonance (high-loss) wavelengths λ_{res} which determines the high loss region is

$$\lambda_{res} = \frac{2d}{m}\sqrt{n_{clad}^2 - n_{core}^2} \qquad (5-5)$$

where d is the thickness of the core wall, m is a positive integer and n_{clad} is the refractive index of silica, which is taken as 1.419 for the mid-IR region around 3 μm [7]. For m = 2 and d = 2.66 μm this gives 2.68 μm as a high-loss wavelength.

A second similar fibre of 7 m length, which was drawn from the same group of canes, has the first band shifted to a longer wavelength range (fig. 5.13). The core diameter was 108 μm and the average core-wall thickness as 3.0 μm. Equation (5-5) would give the first band edge wavelength as 3.02 μm in the new fibre, which is in agreement with the observations in fig. 5.13. The spectral features associated with the CO_2 and OH^- band are now apparent in the transmission spectrum through this shorter piece of fibre, and are distinct from the high-attenuation region. Between 4.2 μm and 4.3 μm, CO_2 absorption features are clear to see.

Although 7 m of fibre was too short to accurately measure the minimum attenuation, a cut-back measurement showed that the attenuation at 4 μm wavelength was below 0.5 dB/m.

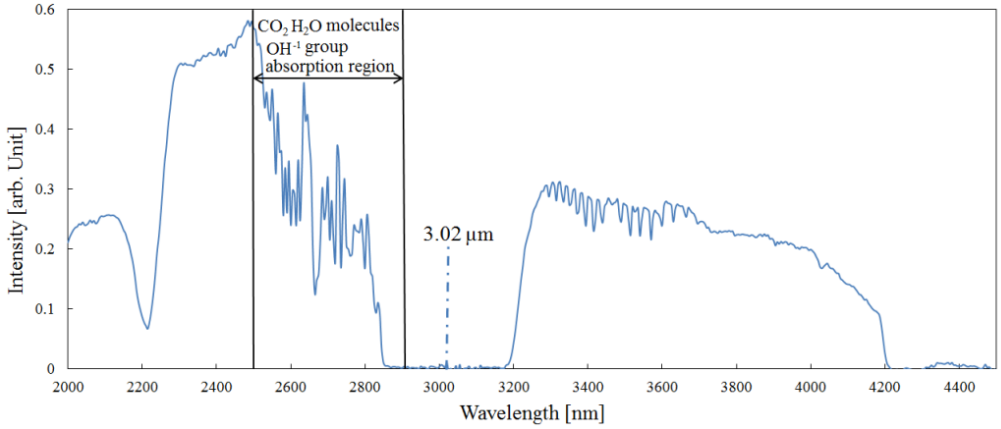

Fig. 5.13 Transmitted spectrum through 7 meters of fibre with 108 µm core, with dashed line representing the theoretical resonant (high-loss) wavelength. The OH^- absorption lines are unresolved in this 10 nm resolution scan.

The confinement of the guided light was investigated by using a fibre butt-coupling technique. The tungsten lamp was used to excite a 79.9 m length of fibre, which was then butt-coupled to a second 3 m length of identical fibre. The transmitted signal was then recorded at the wavelength of 3115 nm by the monochromator as we translated one fibre end in the transverse plane. The recorded data (fig. 5.14) is consistent with the guided light being confined to the hollow core. No deconvolution was applied.

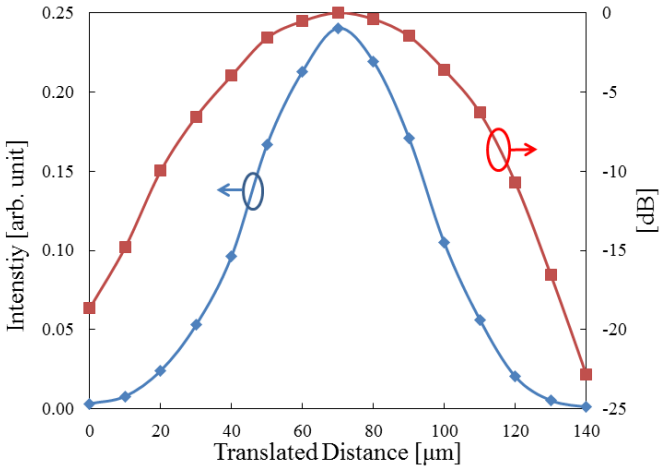

Fig. 5.14 Results of the mode-field measurement using linear and logarithmic scales. The data shown were recorded at a wavelength of 3.15 µm. The core diameter is 94 µm.

As seen in fig. 5.12, absorption peaks appear in the transmission band from 3300 nm to 3700 nm. By comparing the measured absorption spectrum with known gas absorption spectra from the HITRAN 2008 database [8, 10], we found an excellent match in both the peak wavelengths and the relative strengths to HCl. The presence of trace amounts of HCl gas in our fibre would appear to be reasonable given that our

starting material is F300 synthetic fused silica, which the manufacturers state contains 1450 ppm of Chlorine [11], and our measurement is over 80 m in length. Analysis of the observed absorption lines' positions and strengths compared to those from the HITRAN database is shown in fig. 5.15. These lines have subsequently been identified by other groups in their fibres as well [12].

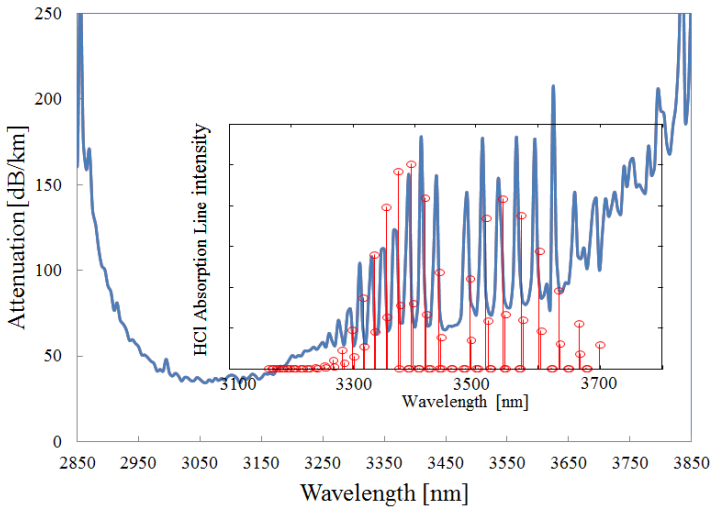

Fig. 5.15 Comparison between the fibre transmission spectrum (blue) and the HCl absorption (red) [10].

It has been confirmed that purging the fibre with nitrogen removes the absorption lines. For a short piece of fibre (e.g. 5 m) the absorption features will also disappear after the fibre is stored in the desiccator for 24 hours.

A laser transmission measurement through the 79 m fibre was performed to verify the spectral transmission band found in the cut-back measurement, using a *Thorlabs H339P2* infrared Helium-Neon laser at a wavelength of 3392 nm. The detected wavelength of the transmitted HeNe laser in fig. 5.16 was 3388 nm, offset by 4 nm from the known value, presumably due to a small miscalibration of our spectrometer.

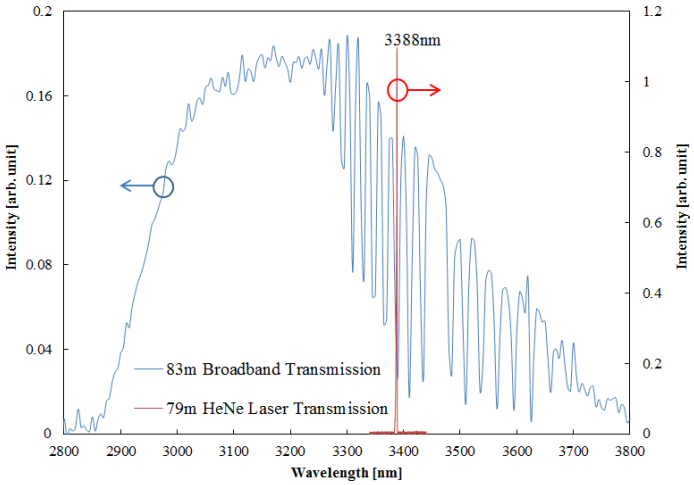

Fig. 5.16 Transmission spectrum through 83 m fibre (blue) and transmitted HeNe laser spectrum (red, 0.5 nm resolution) through 78 m of fibre.

5.3.2 The first band near 4 µm

Figure 5.17 shows the results of cut-back measurement of HC-NCF with the first band in the spectrum around 4 µm (HC-NCF (9) in fig. 5.11). The resolution of the monochromator was set to be 10nm. The total fibre length was 31.2 m and cut back to 5.5 m. The lowest attention of the first band was 0.11 dB/m at the wavelength of 4010 nm. Because the coupling method was free space coupling, the attenuation measurement below 2.8 µm was not reliable.

In the 5.5 m fibre, light transmission can be detected up to 4.7 µm by the monochromator. Between 4.2 µm and 4.3 µm, light coming out of the fibre was completely absorbed by CO_2 in the air [1]. After 4.3 µm, the signal became extremely weak and this was caused by much weaker intensity of light source limited by the black body radiation features and low efficiency of the free space coupling method. In the 31.2 m fibre, no signal can be detected after 4.2 µm.

According to the scaling law, the first band range should span from 3.7 µm to 4.9 µm in theory in comparison with the attenuation spectrum of HC-NCF (7) in fig. 5.11. To precisely determine the first band edge at the longer wavelength, a brighter light source in the mid-infrared spectrum will be necessary for the cut-back measurement.

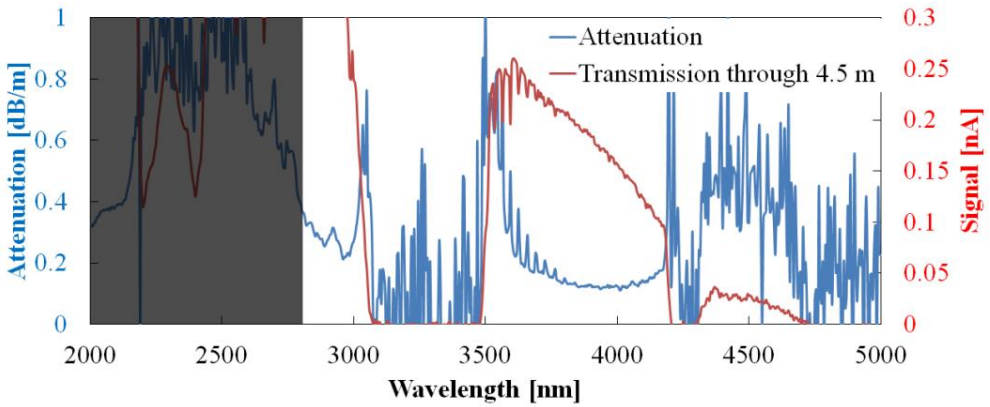

Fig. 5.17 Measured attenuation spectrum of HC-NCF (9) in fig. 5.11 with the first band in above 4 µm. Attenuation above 4.2 µm cannot be determined because of the low intensity of tungsten lamp. The curve in the dark region was not reliable as the free space coupling method was used in the cut-back measurement.

5.3.3 The first band between 2 µm and 3 µm

Figure 5.18 shows the cut-back measurement result of the HC-NCF with the first band transmission between 2 µm and 3 µm (HC-NCF (6) in fig. 5.11). The resolution of monochromator was set to be 10 nm. The total length was 66.8 m and was cut back to 6 m. The lowest attenuation is 24.4 dB/km at 2400 nm wavelength which is the minimum attenuation achieved by HC-NCFs up to now. The fibre-butt coupling method was used in the cut-back measurement and an IR camera was used to monitor the excitation of the fibre modes around 1550 nm in the high order band to prevent light being coupled into the cladding.

In the measurement, a transmission band span of from 2200 nm to 3000 nm was observed in the HC-NCF from the measurement of 6 m fibre after the cut-back; however no signal can be detected in the 66.8 m fibre piece at the wavelength above 2.6 µm. Between 2 µm and 3 µm, CO_2 molecule has a absorption band near 2.7 µm with two main absorption peaks at 3714.7819 cm^{-1} (2.6919 µm) and 3612.8408 cm^{-1} (2.761 µm) [2]. H_2O vapour has multiple strong absorption peaks located around 2.7 µm [10]. On the other hand, because SMF-28 was used in the butt coupling, the coupled light at wavelengths above 2.6 µm would be much attenuated due to the silica absorption. As a result, the weak light through the fibre within this spectral range above 2.6 µm can be strongly attenuated due to the CO_2 and H_2O molecules in the air (this air path is about 1 m inside the monochromator).

Such air absorption effect can also be confirmed in fig. 5.2. OH^{-1} groups in the silica material exhibits a broad band absorption which can also contribute to the measured loss of HC-NCF in this region [2].

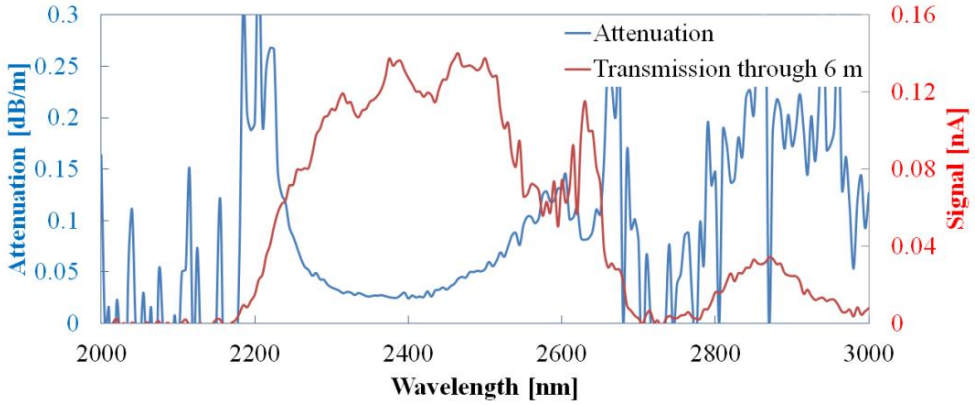

Fig. 5.18 Measured attenuation spectrum of HC-NCF with the first band in between 2 µm and 3 µm (HC-NCF (6) in fig. 5.1). Absorption from CO_2 and H_2O spans from 2.6 µm to 3 µm [1, 2, 10].

5.3.4 The first band below 2 µm

As fig. 5.10 shows, the attenuation of the first bands of HC-NCFs increase rapidly as the wavelength decreases to below 2 µm. Besides higher losses, the attenuation spectra also exhibit distinct spectral fluctuations.

Figure 5.19 shows the cut-back measurement results of the HC-NCF with the first band in between 1500 nm and 1750 nm (HC-NCF (4) in fig. 5.11). An OSA was used for the measurement with the resolution set to be 10 nm. The lowest attenuation is 29.8 dB/km at 1576 nm. The total fibre length was 81 m and was cutback to 3.3 m. The butt-coupling method was used and only the fundamental-like mode was found in the first band when the mode profile was studied by using a camera. The lens coupling method was also used in another cutback measurement of the same fibre. A similar attenuation curve was found but the spectral fluctuations were much stronger.

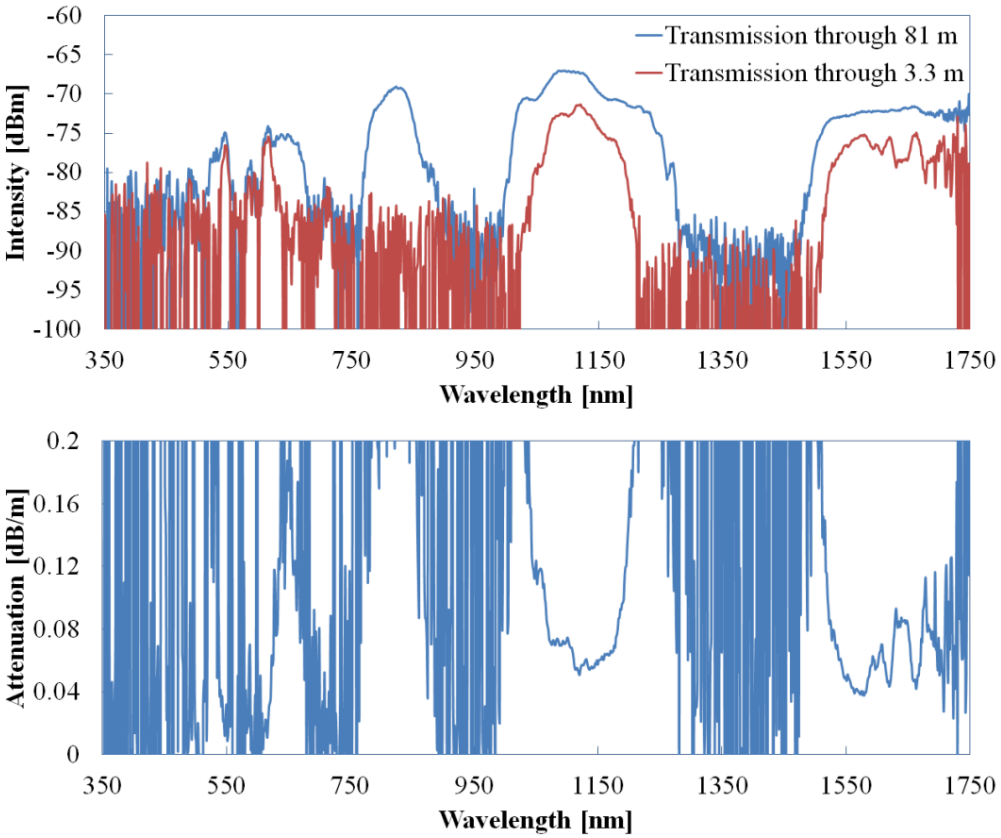

Fig. 5.19 Measured attenuation spectrum of HC-NCF (4) in fig. 5.11 with the first band in between 1500 nm and 1750 nm. Top: measured transmission spectra in 81 m and 3 m fibre lengths. Bottom: calculated attenuation curve.

Mode profiles at different wavelengths were imaged by the objective lens and IR camera at the end of a 3.3 m fibre. A broad light source *Agilent* 83437A (using superluminescent diodes) was used to supply high spectral intensity for imaging at specific wavelengths in the near infrared spectrum. Three 10 nm bandpass filters with central wavelengths at 1540 nm, 1600 nm and 1640 nm were used to take the near field images of modes at specific wavelengths. Figure 5.20 shows the output images at these wavelengths at the end of the 3.3 m fibre.

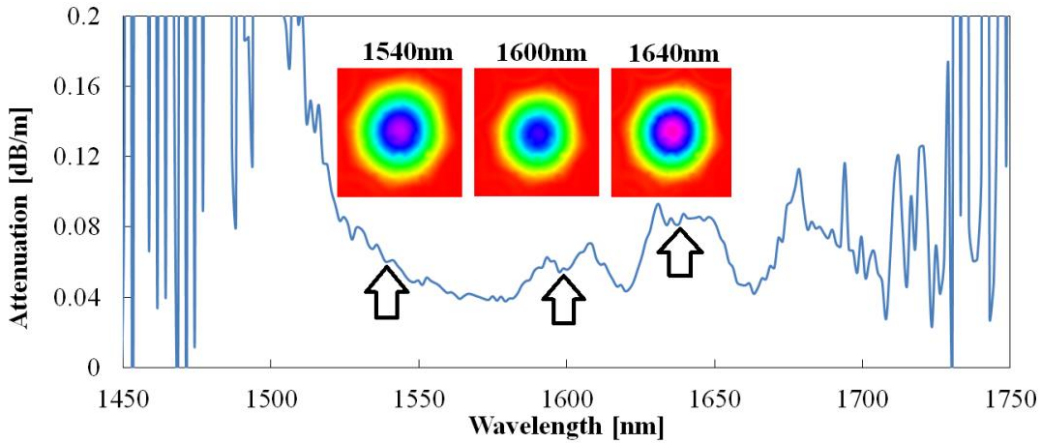

Fig. 5.20 Near field images of the output from the fibre end after 3.3 m transmission. Three 10 nm bandpass filters with central wavelengths at 1540 nm, 1600 nm and 1640 nm were used in the imaging.

The smallest HC-NCF with the first band centred at 850 nm was fabricated too (HC-NCF (1) in fig. 5.11). Figure 5.21 shows the cut-back measurement result. The fibre-butt coupling method was used and the total fibre length was 45 m and was cut back to 3 m.

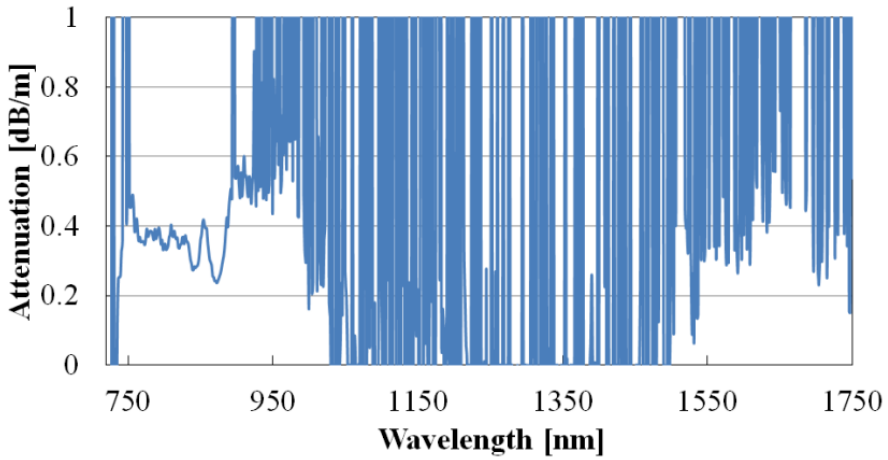

Fig. 5.21 Measured attenuation spectrum of HC-NCF (1) in fig. 5.11 with the first band between 750 nm and 900 nm.

5.3.5 The structural degradation of small HC-NCFs

As shown above, smaller HC-NCFs present higher attenuation in the first band transmission. This characteristics usually emerge with the structural degradation in HC-NCFs.

In fig. 5.22 (left), (1) has the first band between 950 nm and 1300 nm (HC-NCF (3) in fig. 5.11) with the minimum attenuation 0.102 dB/m at 1158 nm. (2) on the right in

fig. 5.22 has the first band between 3 μm and 3.8 μm (HC-NCF (7) in fig. 5.11) with the minimum attenuation 0.032 dB/m at 3050 nm. Comparing the smaller fibre with the bigger fibre in fig. 5.22, we can find that cladding fusion becomes worse for smaller fibres. The fused part between capillaries can be regarded as extra waveguides which may have their own modes interacting with the airy mode in the core. The mode coupling would increase loss level of HC-NCF. In fig. 5.22, we can also find that, the smaller fibre has a less curved core boundary. If we assume that the cladding fusion contributes the loss level of HC-NCFs, then the negative core boundary will help to effectively isolate the core mode from the cladding mode in space which helps to reduce the transmission loss of HC-NCF. As a result, the less curved core boundary and significant fusion in the cladding can lead to a high attenuation level of HC-NCF.

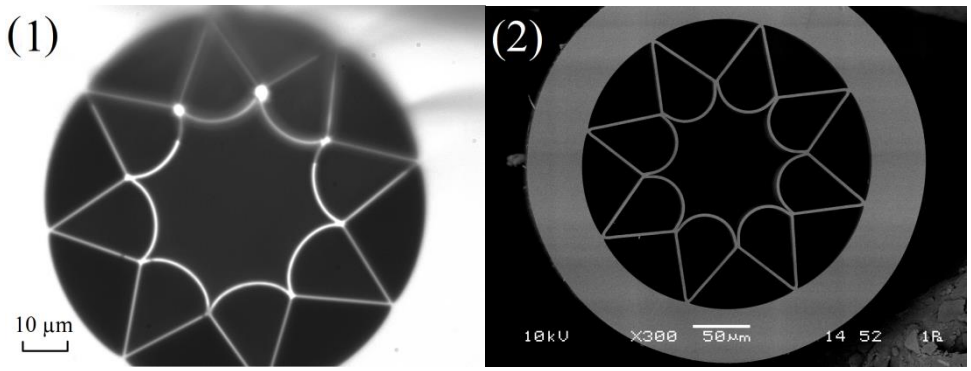

Fig. 5.22 (1) HC-NCF with the first band between 950nm and 1300 nm (fig. 5.11 (3));
(2) HC-NCF with the first band between 3 μm and 3.8 μm (fig. 5.11 (7)).

5.4 Limits of first band attenuations of HC-NCFs

Table 5.1 lists minimum attenuations and other properties of the nine fibres from fig. 5.11 including corresponding wavelengths, core sizes and core wall thicknesses.

NCF NO. in fig. 5.11	1	2	3	4	5	6	7	8	9
Minimum Attenuations [dB/km]	242	102	57	38	35	24.4	32	76.7	110
Wavelength [nm]	869	1158	1270	1576	2026	2400	3050	3635	4010
Core size [μm]	22.5	38.3	35	46	61	61	93	108	119
Core wall thickness [μm]	-	0.91	-	-	-	-	2.66	-	-

Table. 5.1 Minimum attenuations with their corresponding wavelengths, core sizes, and core wall thicknesses of the nine fibres shown in fig. 5.11.

Figure 5.23 plots the minimum attenuations with the wavelengths listed in table 5.1. Since the transverse scale of HC-NCF changes without otherwise changing the fibre's structure, the wavelength λ of minimum attenuation must scale in proportion (section 2.4). It means that the minimum attenuation which is totally determined by the confinement loss must scale with its wavelength λ as λ^{-1}. When other loss mechanisms are involved, the confinement loss is no longer the only loss source and the reciprocal relationship will be changed accordingly. Therefore, to explore the loss mechanisms at different wavelength ranges, the power exponential function is applied in the fitting of minimum attenuations and their wavelengths.

In the short wavelength region from 700 nm to 1300 nm, the minimum measured attenuation scales approximately with the wavelength λ as $\lambda^{-3.6}$ as shown. Fibres in this spectral range are smaller and more difficult to fabricate. Degradation of fibre structure often brings with high attenuation.

Meanwhile the significant fluctuations of attenuation spectra of small HC-NCFs are very hard to ignore. This fluctuation could be caused by coupling between the core mode and surface modes [13, 14]. In the fabrication, the surface roughness of the core

wall is inevitable due to the surface capillary waves (SCWs) frozen into the fibre as it is made [14]. This microscopic variation along the length can cause light scattering and this scattering can be interpreted as interaction between the surface mode and core mode [13, 14]. The scattering effect will be enhanced for shorter wavelengths. In HC-PBG, it has been demonstrated experimentally that the loss caused by the surface scattering α_s is associated with the minimum attenuation wavelength λ_c as $\alpha_s \sim \lambda_c^{-3}$ [15]

The result of $\lambda^{-3.6}$ differs from the familiar λ^{-4} dependence of Rayleigh scattering in the bulk media or λ^{-3} dependence of the surface scattering in HC-PBG [14]. We attribute the observed rapid increase of attenuation below 1 μm to a combination of surface scattering [13, 14, 15] and structure degradation in the cladding of HC-NCFs.

In the wavelength range between 1 and 3 μm, a fit to our data finds the minimum attenuation scaling with wavelength λ as $\lambda^{-0.998}$, which implies that in this wavelength range confinement loss mainly dominates the attenuation.

At long wavelengths beyond 3500 nm, F300 from silica rises rapidly from around 100 dB/m at 3500nm to about 10,000 dB/m at 5μm. In Chapter 3, *Comsol* simulations predict that fibre attenuation will be 7500 times less than the material absorption due to the very low overlap of the airy core mode with the silica glass in the cladding at these long wavelengths (fig. 2.14). By scaling the measured material absorption by this factor and adding it to the predicted confinement loss from *Comsol*, the total fibre loss (orange dashed line in fig. 5.23) is found to increase rapidly with material absorption and to dominate the attenuation of HC-NCF in this spectral range. Measured attenuation for our best fibre was found to be 85 dB/km at the wavelength of 4 μm, which is 10000 times less than the measured bulk glass absorption.

In summary, in conventional index guiding fibres, the attenuation is limited by Rayleigh scattering and by multi-phonon absorption at short and long wavelengths, respectively. However, in HC-NCF, due to the small overlap between core mode and fibre material those effects are significantly reduced [14]. The attenuation in the fibres reported here is dominated by surface scattering and structural losses at short wavelengths and by material absorption at long wavelengths. At intermediate wavelengths, and away from the OH^- absorption bands in the silica matrix [11], attenuation is limited by confinement losses.

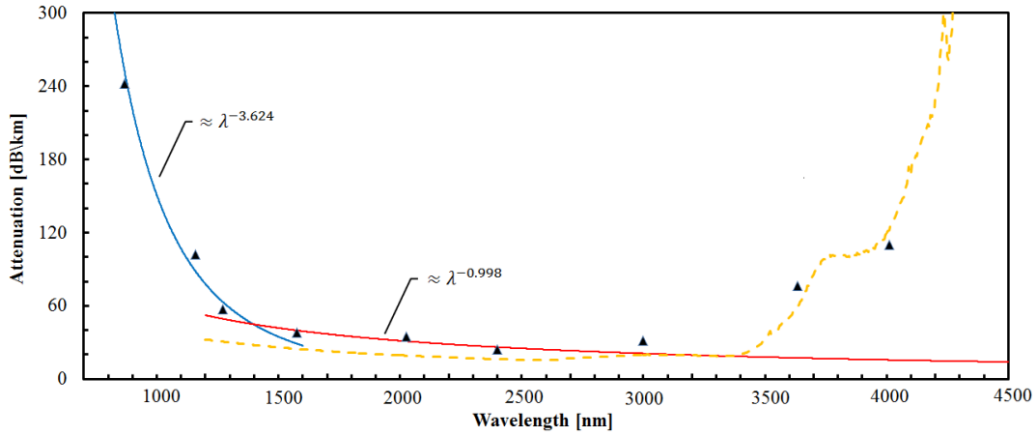

Fig. 5.23 Scaling of minimum attenuations with wavelength. Measured data is shown as triangles. The blue and red solid lines represent fits to selected points of attenuation = $A \bullet \lambda^x$ with a resulting x of -3.642 and -0.998 separately (blue curve fitting data points between 700 nm and 1300 nm; red curve fitting points between 1500nm to 2500 nm). The orange dashed line is total attenuation based on predictions of confinement losses from *Comsol* and scaled absorptive loss.

Figure 5.24 shows the relationship between the core sizes and the minimum attenuation wavelengths in the first band. Due to the scaling law, the change of fibre dimension will shift the first band's position and rescale the attenuation level accordingly. Then the ratio of the core size to the minimum attenuation wavelength should be constant in the scaling of fibre dimensions in theory. This ratio exhibits the dimensional consistency between different HC-NCFs. Any deviation from it can reflect the deformation of fibre structure.

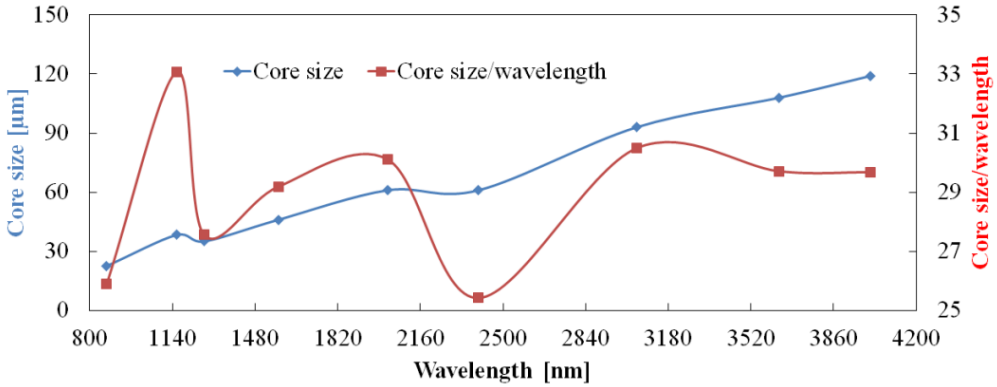

Fig. 5.24 Relation between the core sizes and wavelengths of minimum attenuations.

In fig. 5.24, all the nine fibres show a reasonably good dimensional consistency. Among them fibres (4), (5), (7), (8) and (9) in fig. 5.11 present better consistency than the rest. As a result, the minimum attenuations of these five fibres have very strong correlation between each other. In contrast, fibres (1), (2), (3), (4) and (6) are relatively deformed.

5.5 Conclusions

Chapter 5 presents the study of attenuation properties of HC-NCFs.

The cut-back measurement is the main method to determine the attenuation of HC-NCF experimentally. Although it is simple in theory, many factors can influence the accuracy of measurement results. The mode excitation method, the choice of cutting position and the prevention of additional bending loss are keys to obtaining reliable attenuation measurements.

The material absorption of F300 fused silica as the fabrication material of HC-NCF was measured in the spectral range between 2.8 μm and 4.8 μm. The absorption increases rapidly with wavelength from tens of dB/m around 3 μm to more than 8000 dB/m near 5 μm.

Different NCFs were designed and fabricated for coverage of various spectral regions. The measured attenuation reached 24 dB/km at 2.4 μm wavelength (limited by confinement) and 85 dB/km at 4 μm wavelength where the material absorption is about 865000 dB/km.

The scaling of minimum attenuation with wavelengths reveals that surface scattering and structural imperfections, confinement loss and material absorption dominate attenuation properties of HC-NCFs in different wavelength ranges. In the shorter wavelength range below 1.5 μm, the structural degradation of HC-NCFs may fundamentally limit the performance of fibres; in the long wavelengths after 3 μm, the material absorption causes the rising of fibre loss; finally the confinement loss dominates the wavelength range in between and the lowest attenuation can be found in this wavelength range.

Reference

[1] L. S. Rothman, R. L. Hawkins, R. B. Wattson, and R. R. Gamache, “Energy levels, intensities, and linewidths of atmospheric carbon dioxide bands,” Journal of Quantitative Spectroscopy and Radiative Transfer **48**, 537-566 (1992).

[2] O. Humbach, H. Fabian , U. Grzesik, U. Haken, and W. Heitmann, “Analysis of OH absorption bands in synthetic silica,” J. Non-Cryst. Solids **203**, 19-26 (1996).

[3] H. Haken, *Light: Waves, Photons, Atoms* (North-Holland, 1981).

[4] A. W. Snyder and J. D. Love, *Optical waveguide theory* (Chapman & Hall, 1983).

[5] A. Urich, R. R. J. Maier, Fei Yu, J. C. Knight, D. P. Hand, and J. D. Shephard, "Flexible delivery of Er:YAG radiation at 2.94 μm with negative curvature silica glass s: a new solution for minimally invasive surgical procedures," Biomed. Opt. Express **4**, 193-205 (2013)

[6] A. N. Kolyadin, A. F. Kosolapov, A. D. Pryamikov, A. S. Biriukov, V. G. Plotnichenko, and E. M. Dianov, "Light transmission in negative curvature hollow core fiber in extremely high material loss region," Opt. Express **21**, 9514-9519 (2013)

[7] R. Kitamura, L. Pilon, and M. Jonasz, “Optical constants of silica glass from extreme ultraviolet to far infrared at near room temperature,” Appl. Opt. **46**, 8118-8133 (2007).

[8] J. A. Coxon and P. G. Hajigeorgiou, “The radial Hamiltonians for the X1S+ and B1S+ states of HCl,” J Mol Spectrosc **203**, 49–64 (2000)

[9] N. M. Litchinitser, A. K. Abeeluck, C. Headley, and B. J. Eggleton, “Antiresonant reflecting photonic crystal optical waveguides,” Opt. Lett. **27**, 1592-1594 (2002).

[10] L.S. Rothman, I.E. Gordon, A. Barbe, D.Chris Benner, P.F. Bernath, M. Birk, V. Boudon, L.R. Brown, A. Campargue, J.-P. Champion, K. Chance, L.H. Coudert, V. Dana, V.M. Devi, S. Fally, J.-M. Flaud, R.R. Gamache, A. Goldman, D. Jacquemart, I. Kleiner, N. Lacome, W.J. Lafferty, J.-Y. Mandin, S.T. Massie, S.N. Mikhailenko, C.E. Miller, N. Moazzen-Ahmadi, O.V. Naumenko, A.V. Nikitin, J. Orphal, V.I. Perevalov, A. Perrin, A. Predoi-Cross, C.P. Rinsland, M. Rotger, M. Šimecková, M.A.H. Smith, K. Sung, S.A. Tashkun, J. Tennyson, R.A. Toth, A.C. Vandaele, and J. Vander Auwera, “The HITRAN 2008 molecular spectroscopic database”, Journal of Quantitative Spectroscopy and Radiative Transfer **110**, 533-572 (2009).

[11] U. Haken, O. Humbach, S. Ortner, and H. Fabian, “Refractive index of silica glass: influence of fictive temperature,” J. Non-Cryst. Solids **265**, 9-18(2000).

[12] N. V. Wheeler, A. M. Heidt, N. K. Baddela, J. R. Hayes, S. R. Sandoghchi, E. Numkam Fokua, F. Poletti, M. N. Petrovich, and D. J. Richardson, “Low loss side bandwidth low bend sensitivity HC-PBGF for mid-IR applications,” Workshop on Speciality Optical Fibres (WSOF) Sigtuna,Sweden 28-30 Aug 2013

[13] K. Saitoh, N. Mortensen, and M. Koshiba, "Air-core photonic band-gap fibers: the impact of surface modes," Opt. Express **12**, 394-400 (2004)

[14] P. J. Roberts, F. Couny, H. Sabert, B. J. Mangan, D. P. Williams, L. Farr, M. W. Mason, A. Tomlinson, T. A. Birks, J. C. Knight, and P. St.J. Russell, "Ultimate low loss of hollow-core photonic crystal fibres," Opt. Express 13, 236-244 (2005).

[15] B.J. Mangan, L. Farr, A. Langford, P. J. Roberts, D. P. Williams, F. Couny, M. Lawman, M. Mason, S. Coupland, R. Flea, H. Sabert, T. A. Birks, J. C. Knight, P. St. J. Russell, "Low loss (1.7 dB/km) hollow core photonic bandgap fiber," in Optical Fiber Communication Conference, (Optical Society of America, 2004) pp.33.

Chapter 6 Other properties of hollow core negative curvature fibre

Chapter 6 presents characterization of other properties of HC-NCFs including the bending loss and group velocity dispersion.

As HC-NCFs cannot truly confine light in the core like index-guiding fibre or HC-PBG, the bending, which alters the geometry of HC-NCFs, will inevitably affect the guidance of light and cause extra loss. In section 6.1, the bending effect is experimentally explored by bending a 2.3 m HC-NCF into a half circle of different diameters and comparing the transmission spectra. The bending effect is discussed based on the measurement.

The dispersion of HC-NCFs is fundamentally determined by the waveguide dispersion in the low loss spectral region. Section 6.2 presents the measured group velocity dispersion of HC-NCF. A white light interferometer was used in the measurement. The challenges in the dispersion measurement are also discussed.

6.1 Bending loss

6.1.1 Bending loss measurement

Bending loss of HC-NCF was explored by bending a 2.3 m long HC-NCF with the first transmission band between 2.9 μm and 3.8 μm (HC-NCF (7) in fig. 5.11) into a semicircle. At one end, light from a tungsten lamp was coupled into the HC-NCF with the free space coupling and the transmission spectrum in the first band was measured by the monochromator at the other end. The transmission spectra were recorded under different bend diameters *D* and the results are presented in fig. 6.1.

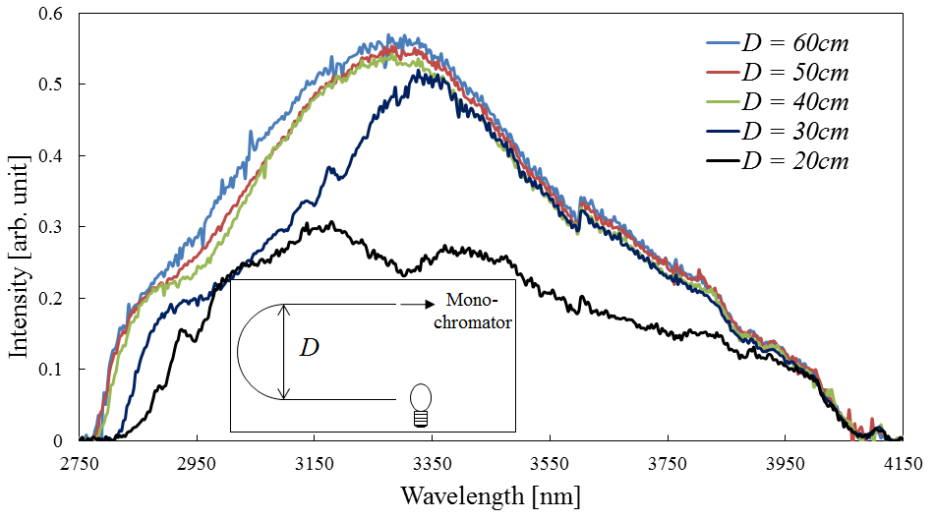

Fig. 6.1 Transmission spectra of HC-NCF with different bending diameters. Light from a tungsten halogen lamp was coupled into 2.3 m fibre and the output spectrum was measured with monochromator. The middle of fibre was bent in a half circle of different diameters D and both ends were kept straight as shown in the inset.

Figure 6.1 shows that, with *D* above 40 cm, bending loss does not affect the transmission spectrum significantly. When *D* becomes smaller than 40cm, the transmission spectrum starts to be attenuated and the shorter wavelengths are more sensitive to the bending effect than the longer wavelengths. For *D* smaller than 20 cm the transmission over the whole spectrum is substantially degraded.

6.1.2 Discussions

Generally, the bending loss in the optical fibre can be categorized into macro-bending and micro-bending according to the mechanisms dominating the loss [1]. The micro-bending refers to the periodic or random deformations of the refractive-index distribution or of the geometry of optical fibres along the length, which can cause the energy to couple between the core modes and cladding modes if the deformations

change sufficiently rapidly along the fibre axis [2]. The loss mechanism of micro-bending is essentially a scattering phenomenon which is not the interest of this chapter. The bending effect discussed in this chapter is the macro-bending which accounts for the radiated loss associated with the curved guidance when the fibre is bent.

The bend loss of index guiding fibre has been widely studied for the needs in the telecommunication. In 1969, Marcatili raised the first model to analyse the bending loss in a slab waveguide of rectangular cross-section [3]. He adopted the Hankel function to represent the cladding mode instead of the modified Bessel functions in order to introduce the radiation leakage caused by bending in the framework of mode theory [3]. Following a similar method, Lewin extended the analysis to optical fibre with cylindrical cross-section in 1974 [4]. In 1975, Heiblum and Harris introduced the equivalent refractive index distribution model and simplified the analysis by replacing the curved fibre with a straight one of equivalent refractive index distribution [5]. In 1976, Marcuse derived the bending loss formula of optical fibre from the scalar wave equation using the large argument approximation of the Hankel function [6]. The works introduced above fundamentally established our understanding of bending loss of index guiding optical fibre.

The studies of bending loss in HCFs are mainly performed by experimental measurement [7 - 9] and numerical simulations [10]. Although the complete picture describing bending loss in HCF has not been fully described, we can still point out some potential origins of bending loss which are summarized below.

1) Coupling between the core modes and cladding modes

According to Vincetti and Setti's model (section 2.2.3) [11], the coupling between the core modes and cladding modes fundamentally determines the high loss spectral region in leaky HCFs. When HC-NCF is bent, both the cladding and the core have to experience deformation. This deformation can significantly alter the mode properties in HC-NCF and the loss associated with bending can be expected to change accordingly.

A capillary waveguide is the simplest leaky HCF and the discussion of the influence of bending on the mode attenuation of the capillary waveguide can give us some preliminary understanding of bending loss in HC-NCF. The equivalent refractive index distribution model is adopted in the discussion here [5].

Figure 6.2 schematically illustrates the refractive index distributions of the horizontal cross-section of a straight capillary waveguide (fig. 6.2 left) and the equivalent refractive index distribution of the horizontal cross-section of the same capillary waveguide being bent horizontally (fig. 6.2 middle and right). The refractive index of the solid material is n_1

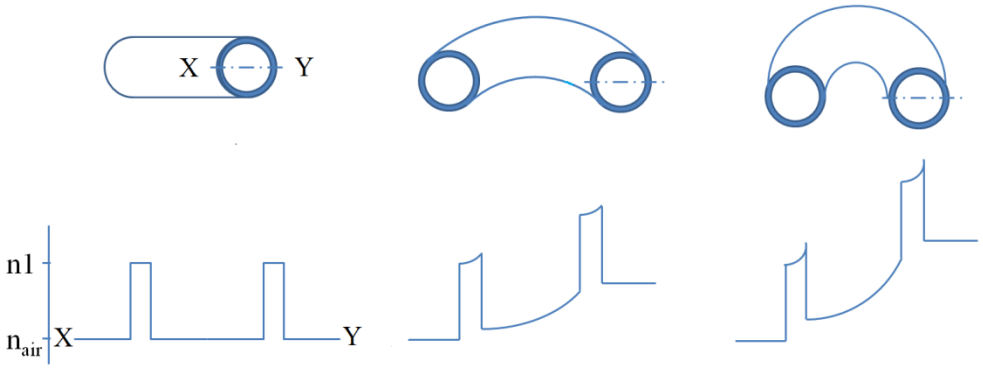

Fig. 6.2 Schematics of a capillary waveguide (top) and the corresponding refractive index distribution (bottom) from being straight to bending.

As the capillary is bent, the airy modes in the core and the cladding modes all experience phase lags in space because different locations have different local bending radiuses. The phase lag in a bent fibre can be equivalently to the refractive index redistribution in a straight fibre as illustrated in fig. 6.2.

In fig. 6.2, as the fibre is bent, the refractive index difference between the cladding on one side where the bending radius is smaller and the average refractive index of air core region becomes smaller. In Vincetti and Setti's model [11], for a given wavelength, such reduced refractive index difference will shift the dispersion curves of cladding modes. And the cut-off frequency of the cladding mode increases in this condition. The coupling between the core modes and cladding modes at certain wavelengths will be enhanced, which may fundamentally result in higher loss due to the bending effect (fig. 2.6) [11].

An extreme example of bending distortion influencing the cladding mode coupling is that, as the bending radius of HC-NCF is extremely small, the thickness of the core wall can even be tuned according to the local bending radius so that the resonance property of cladding mode can be totally changed according to the ARROW model

(section 2.2.2) [12]. In this case, the first band transmission would become much narrower.

2) High order mode conversion

In the ray optics model, the bending effect causes the propagation of light in the fibre to deviate from the axial direction. Under a certain condition, such a deviated light ray can efficiently excite high order modes. As high order modes are usually accompanied with higher loss, the increased attenuation at small bend radius can be caused by conversion of the guided light to higher-order modes.

In 1969, Marcatili firstly pointed out the high order mode conversion as a main loss mechanism in the higher refractive index core waveguide [3]. He demonstrated that, under multimode guidance, the loss originating from high order mode conversion is many orders of magnitude larger than the radiated loss of the fundamental mode because of bending [3].

In the HC-NCF, a cutback measurement revealed that the high order mode experienced a much higher loss than the fundamental mode [13]. The high order mode conversion can be an important reason of high bending loss in HC-NCFs.

3) Enhanced material absorption and surface scattering

As the fibre is bent, the overlap between the core mode field and the cladding material may increase. Recently Belardi and Knight studied the bending effect in HC-NCFs by simulations and demonstrated that as HC-NCF is bent, the core mode field approaches towards one side of the core wall, which can raise the percentage of power of optical field in the cladding [10].

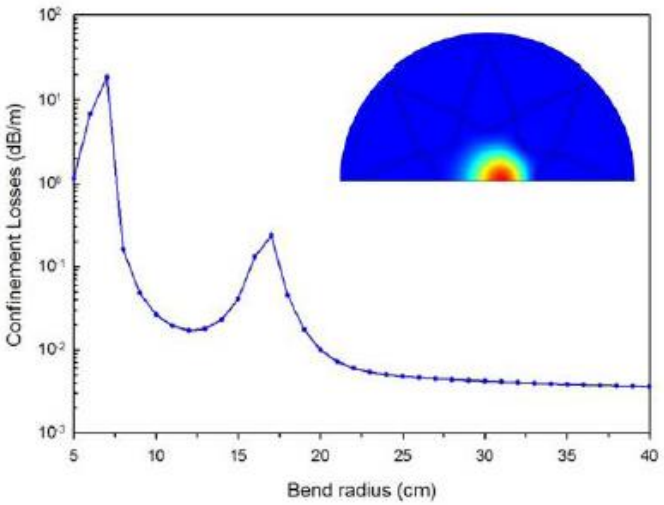

Fig. 6.3 The relationship between the loss of HC-NCF and bend radius. Inset illustrates the fundamental mode in HC-NCF in bending (fig. 6.3 is cited from ref [10]).

The increased overlap between the core mode field and cladding material can enhance the material absorption and surface scattering effects. Under this assumption, especially at the long wavelengths, where the cladding material becomes opaque, and the short wavelengths, where the scattering effect becomes more significant, light propagation in the HC-NCF is more susceptible to the bending effect.

In summary, the study of loss mechanisms associated with bending in HC-NCF is still under development. I qualitatively analysed how bending influences the loss of HC-NCF, which are cladding mode coupling, higher order mode conversion and enhanced material absorption and surface scattering due to the increased overlap between the core mode field and the cladding material. To further improve our understanding of bending effect, more theoretical and experimental works are necessary.

6.2 Group velocity dispersion

6.2.1 White light interferometer

Dispersion is an important property of optical waveguides which plays a key role in both linear and nonlinear optics. The commonly used experimental measurement methods of group velocity dispersion (GVD) of optical fibre can be generally categorized as follows [14]

1) Pulse delay measurement: characterizes the flight time of pulses in a long piece of fibre. This technique requires a fast pulse detection method and a long fibre length which is usually over 0.5 km [14, 15]. A pulsed laser source with a relative broadband tuning spectrum is also necessary.

2) Phase shift measurement: measures the phase shift of a sinusoidally modulated signal from a broadband light source after propagation in a long piece of fibre. This technique also requires a long length of optical fibre for a precise measurement. Meanwhile, a LED with a large signal-to-noise ratio and dynamic range is often required [14, 16].

3) Interferometry method: measures the group delay of wavelengths after propagation in a known length of fibre. This technique is adopted in this chapter.

The interferometry method can usually achieve the highest resolution of all the three even with a very short length of fibre. The white light interferometer used to measure the GVD was firstly reported in the dispersion measurement of the conventional optical fibre in 1981 [17, 18] and in 1999 it was reported to be used to obtain the dispersion of PCF [19]. In 2009, this method was successfully applied to accurately measure GVD of HC-PBG [20].

1) Configuration of experiment setup

Figure 6.4 is the schematic of the white light interferometer used to measure the GVD of HC-NCF. White light beam is firstly divided by 50 : 50 broadband beam splitter. One beam is coupled into HC-NCF (signal arm) and the other travels in the air (reference arm) where the path length is adjustable by mirror reflection.

A lens is used to achieve a high coupling efficiency between the beam and the fibre. At the other end of fibre, a mirror is set as close as possible to the fibre end to reflect light back to the core of fibre. In the reference arm, an identical lens and a

mirror are installed on a translation stage. The use of an identical lens in the reference arm is to compensate the material dispersion caused by the lens in the system as much as possible. The mirror on the stage is set in the focal plane of the lens to minimize divergence of beam. Finally the two beams of light from the signal arm and reference arm are combined by the same beam splitter. After passing a narrow bandpass filter, the combined beams are detected by a sensor and then the signal from the sensor will be amplified by a lock-in amplifier system. With the movement of the translate stage, the interference signals of two beams are recorded and by recognizing the peak position of the interference patterns at the different wavelengths, finally the group delay as function of wavelength is obtain and GVD will be calculated based on the data.

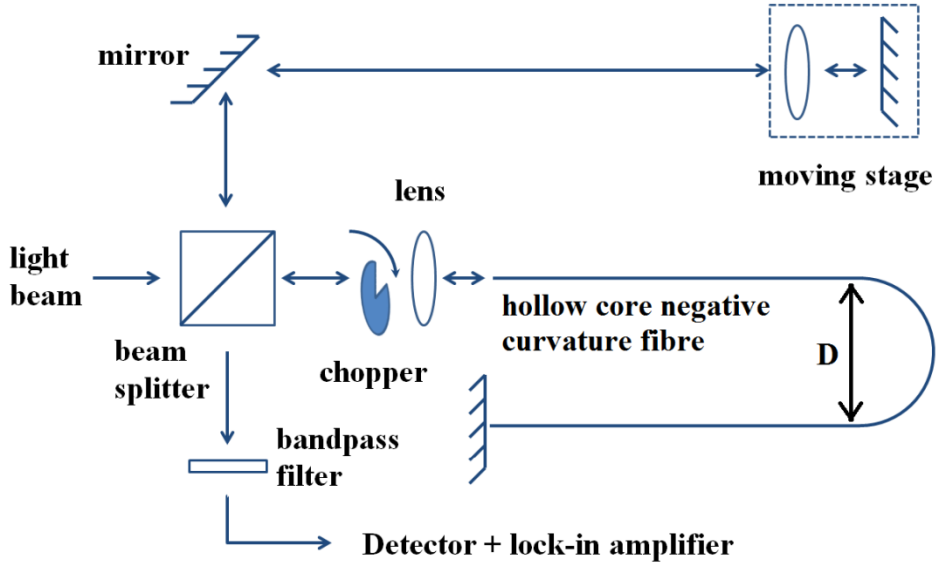

Fig. 6.4 Schematic of white light interferometer to measure GVD of HC-NCF.

2) Design of experiment

As the core of HC-NCF is full of air, the dispersion of HC-NCF is fundamentally determined by the waveguide dispersion. Due to the large core size of HC-NCF in comparison with other HCFs like HC-PBG, a much smaller GVD is expected in HC-NCF because of much reduced waveguide dispersion. To obtain a precise measurement of the interference peak shift at different wavelengths, a long fibre length is necessary to accumulate dispersion so that the shifting of interference peaks at different wavelength can be measured precisely. In the experiment, a Michelson interferometer configuration is chosen rather than a Mach-Zehnder interferometer, in order to double the distance the light travels through the fibre.

Because of the bending effects, the fibre in the experiment should be straight or bent with a large bending radius. Due to the space limit in the lab, the longest length of fibre measured in the experiment was 2.2 m. It was bent in a big loop of nearly 50 cm in radius.

In our experiment, HC-NCF which has the second band between 1540 nm and 1750 nm (HC-NCF (6) in fig. 5.11) was chosen for the dispersion measurement. This choice is because of the challenge of the weak interference signal detection in the white light interferometer at the longer wavelength range above 2 μm.

Because of the nature of black body radiation (section 5.1.1), the thermal light source is not the first choice for GVD measurement at long wavelengths. On the other hand, the use of a narrow bandpass filter only allows a 10nm spectral pass band, greatly increasing the difficulty of signal detection. For wavelengths above 1.7 μm, the sensitivity of detectors which are commercially available drops quickly (fig. 6.5) [21]. Even with the help of lock-in amplifier system, the GVD measurement for those long wavelengths is still too difficult. A commercial supercontinuum light source can usually supply a much brighter broad band spectrum spanning from the visible to the near infrared, however the wavelength range does not extend beyond 2.6 μm [22]. λ

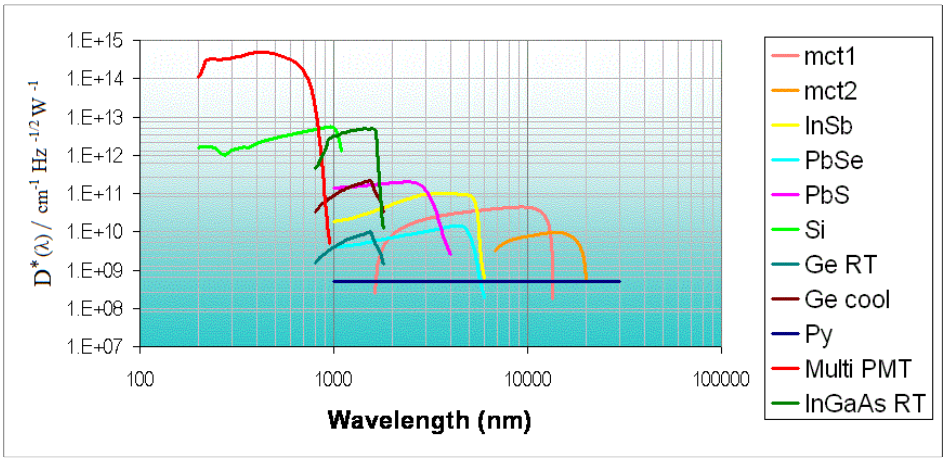

Fig. 6.5 Responsitivity of common commercial optical detectors. Fig. 6.5 is cited from ref [20].

In the signal arm, a substantial amount of optical power will be lost due to the limited coupling efficiency, as HC-NCF has a small numerical aperture which makes coupling challenging. Considering other origins of loss in the experiment, including the beam splitter, mirror reflectivity and chromatic dispersion of lens focusing *etc.*, a

bright broadband light source with a high spectral density of power and a highly sensitive detector are required for a reliable GVD measurement. The supercontinuum source is finally chosen as the light source and the optical detector of high responsitivity below 2 μm, *New Focus 2513* femto-watt InGaAs photoreceiver with a maximum gain as $2x10^{11}$ V/W is used in the measurement.

The HC-NCF which was chosen for the dispersion measurement (HC-NCF (6) in fig. 5.11) has a second transmission band between 1520 nm to 1750 nm. Comparing with other HC-NCFs with transmission in this spectral range, this fibre has a flatter transmission spectrum in both the first and second transmission bands (fig. 5.18 and fig. 6.6), which implies that the interactions between the core mode and surface mode/cladding mode are much reduced. Therefore the measured GVD should reflect the "ideal" core mode dispersion without interference from surface modes. Figure 6.6 shows the attenuation of the second band measured using a cut-back measurement. The fibre was cut from 39 m to 4 m. The second band spans 210 nm and has the minimum attenuation of 0.18 dB/m at the wavelength of 1708 nm. The inset in fig. 6.6 is the near field image of the output of fibre. No filter was used to record this image.

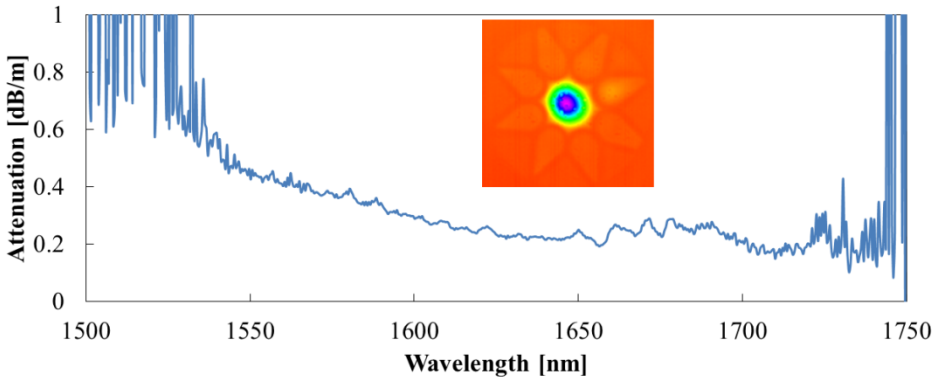

Fig. 6.6 Measured attenuation of the second band of HC-NCF used in the dispersion measurement (HC-NCF (6) in fig. 5.11). The total fibre length was 39 m and cut to 4m. Inset: near field image of output of fibre.

6.2.2 Results and discussions

Figure 6.7 shows the relative group delay of light at different wavelengths after propagating inside 0.88 m and 2.2 m long fibres.

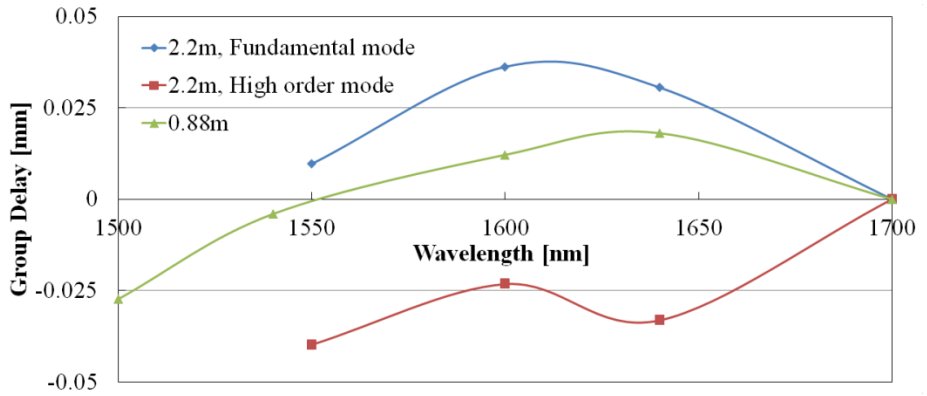

Fig. 6.7 Results of group delays in the 0.88 m and 2.2 m long fibres.

In the 2.2 m fibre, two interference peaks were always found in a long scan of the translation stage at the same wavelength while changing the bandpass filters. Figure 6.8 shows interference patterns filtered by the 10 nm wide bandpass filter centred at 1640 nm. Figure 6.8 (2) and (3) are zoom-in of the two peaks near 4mm and 12 mm respectively.

According to the waveguide theory [23], the group velocity can be generally expressed as

$$\upsilon_g \propto \frac{c}{n_{core}^2}\frac{\beta}{k} \qquad (6-1)$$

where c is the speed of light, n_{core} is the refractive index of the core, β is the propagation constant, $k = 2\pi/\lambda$.

By comparing their corresponding group refractive indexes, it can be confirmed that the interference peak near 12 mm corresponds to the fundamental mode which has the lowest group refractive index and the other belongs to some high order mode.

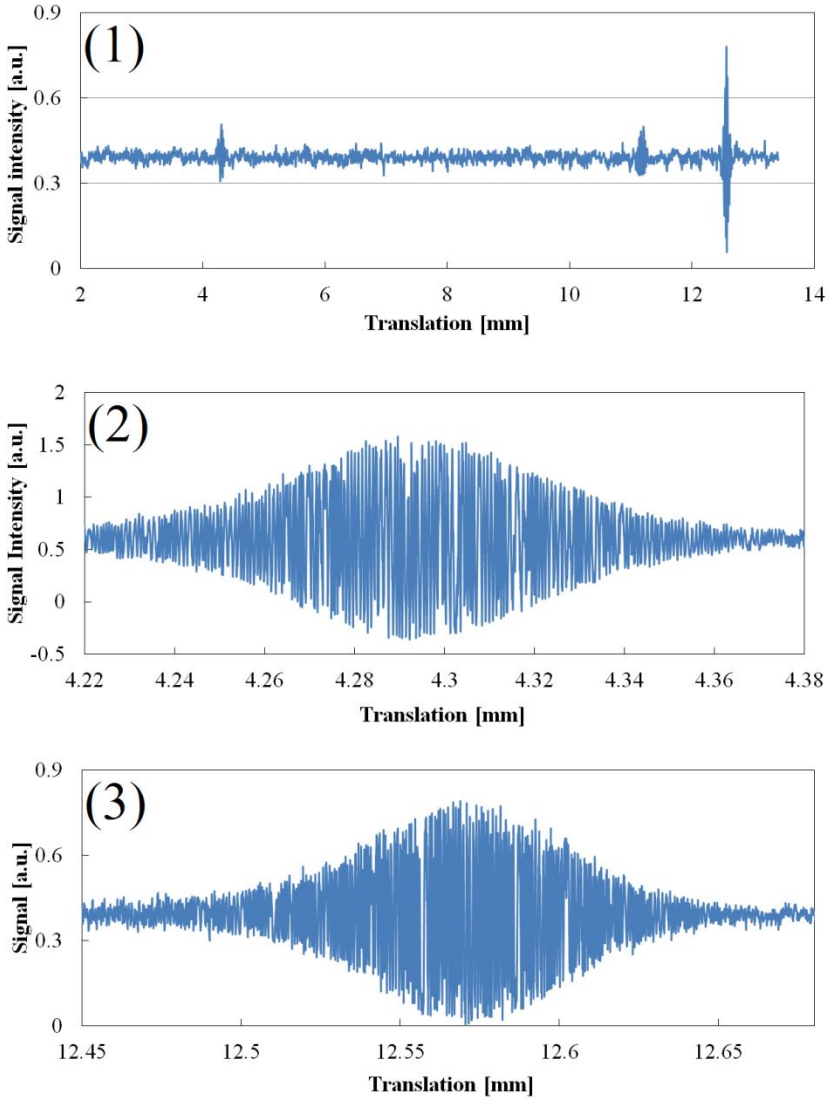

Fig. 6.8 Interference patterns with a bandpass filter centring at 1640 nm. (1) the whole scan shows two interferences near 4 mm and 12 mm; (2) zoom-in of the interference pattern near 4 mm; (3) zoom-in of the interference pattern near 12 mm.

In fig. 6.7 the group delay in the 0.88 m fibre follows a similar trend as the fundamental mode in the 2.2 mm fibre. At 1600 nm and 1640 nm wavelengths, the 2.2 m fibre has a bigger group delay roughly twice that of the 0.88 m fibre.

Figure 6.9 shows the calculated GVD based on the data from fig. 6.7. As expected, due to the large core size, HC-NCF exhibits a very small GVD.

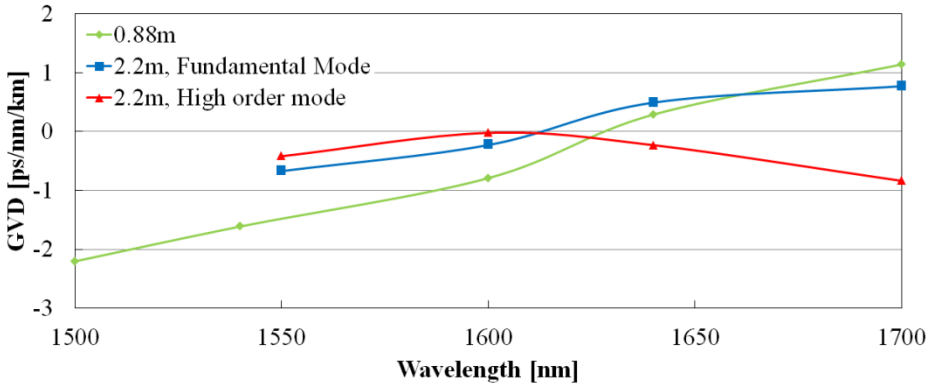

Fig. 6.9 Calculated GVD based on data of the group delays in fig. 6. 7.

The accuracy of the GVD measurement is mainly limited by the accuracy of the relative group delay measurement at different wavelengths and limited wavelength points

At the moment, the reading of the interference peak position in the white light interferometry is by eye, which is hard to analyse the reading errors. A better method can be using program to extract the envelope of the interference pattern and distinguish the peak position by computer.

Due to the smaller dispersion, extending the fibre lengths can improve the accuracy of measurement. However, the accumulation of group delay is linear with the length of fibre. It becomes unrealistic to increase the fibre length by one order of magnitude to improve the measurement precision, especially if we notice that the attenuation of the fibre in the second band is higher than 0.1 dB/m.

The translation stage used in the experiment has a minimum step size of 200 nm and on average interference peak shifts approximately 10 μm in the experiment at two wavelengths of 40 or 50 nm differences. A finer translation stage with a smaller minimum step size could also help to increase the accuracy of the measurement. Although the translation stage suffers from restriction trade-off between the travel range and minimum step, considering the small dispersion in HC-NCF, a small travel range would not be a limiting factor.

To increase the bandwidth of the bandpass filter can also contribute to a more accurate measurement. A broader bandpass filter would allow more optical power passing through to obtain an interference pattern with high sign-to-noise ratio. However, the reduced coherence length (interference pattern length) would bring the difficulty of distinguishing the interference position if the minimum step size of the

translation stage does not match with coherent length. Also there might be fewer wavelength points on the group data curve.

To increase the wavelength points on the GVD curve can help reveal more details of the GVD curve. Due to the commercial availability of bandpass filters, it might be more convenient to use a monochromator instead of discrete bandpass filters. However the monochromator can bring new problems in the experiment including the extra loss and alignment of optical path.

In summary, a low GVD was experimentally measured as expected. However the accuracy of the measurement suffered from the low dispersion of HC-NCFs. A better positioning method of interference peaks and a finer translation stage to measure the displacement of the interference patterns are the keys to achieve a more reliable dispersion measurement of GVD in HC-NCF.

6.3 Conclusions

Chapter 6 presents the characterization of bending loss and dispersion of HC-NCF.

Generally HC-NCF is sensitive to bending. A small bend radius below 20 cm can cause a high bending loss. The shorter wavelengths exhibit higher sensitivity to bending effect than the longer wavelengths in the same transmission band. The way bending influences the loss mechanisms dominating the loss of HC-NCFs were qualitatively analysed. The cladding mode coupling, higher order mode conversion and enhanced material absorption and surface scattering were considered as the potential causes of bending loss in HC-NCFs.

The dispersion property of HC-NCF was experimentally studied by using a white light interferometer. A low GVD was found as expected. A better positioning method of interference peaks and a finer translation stage to measure the displacement of the interference patterns would help to improve the measurement accuracy.

Reference

[1] J. A. Buck, *Fundamentals of optical fibers 2nd edition*, 103 - 112 (Wiley-interscience, 2004).

[2] D. Marcuse, "Microdeformation losses of single-mode fibers," Appl. Opt. **23**, 1082-1091 (1984).

[3] E. A. Marcatili, "Bends in optical dielectric guides," Bell Syst.Tech. J. **48**, 2103-2132 (1969).

[4] L. Lewin, "Radiation from curved dielectric slabs and fibers," IEEE Trans. Microwave Theory Tech. **22**, 718-727 (1974).

[5] M. Heiblum and J. H. Harris, "Analysis of curved optical waveguides by conformal transformation," J. Quant. Electron. **11**, 75-83 (1975).

[6] D. Marcuse, "Curvature loss formula for optical fibers," J. Opt. Soc. Am. **66**, 216–220 (1976).

[7] F. Yu, W. J. Wadsworth, and J. C. Knight, "Low loss silica hollow core fibers for 3–4 μm spectral region," Opt. Express **20**, 11153-11158 (2012).

[8] A. Urich, R. R. J. Maier, F. Yu, J. C. Knight, D. P. Hand, and J. D. Shephard, "Flexible delivery of Er:YAG radiation at 2.94 μm with negative curvature silica glass fibers: a new solution for minimally invasive surgical procedures," Biomed. Opt. Express **4**, 193–205 (2013).

[9] P. Jaworski, F. Yu, R. R.J. Maier, W. J. Wadsworth, J. C. Knight, J. D. Shephard, and D. P. Hand, "Picosecond and nanosecond pulse delivery through a hollow-core Negative Curvature Fiber for micro-machining applications," Opt. Express **21**, 22742-22753 (2013).

[10] W. Belardi and J. C. Knight, "Effect of core boundary curvature on the confinement losses of hollow antiresonant fibers," Opt. Express **21**, 21912-21917 (2013)

[11] L. Vincetti and V. Setti, "Waveguiding mechanism in tube lattice fibers," Opt. Express **18**, 23133-23146 (2010).

[12] N. M. Litchinitser, A. K. Abeeluck, C. Headley, and B. J. Eggleton, "Antiresonant reflecting photonic crystal optical waveguides," Opt. Lett. **27**, 1592-1594 (2002).

[13] A. N. Kolyadin, A. F. Kosolapov, A. D. Pryamikov, A. S. Biriukov, V. G. Plotnichenko, and E. M. Dianov, "Light transmission in negative curvature hollow core fiber in extremely high material loss region," Opt. Express **21**, 9514-9519 (2013)

[14] L. G. Cohen, "Comparison of single-mode fiber dispersion measurement techniques," J. Lightwave Technol. **3**, 958–966 (1985).

[15] L. G. Cohen and Chinlon Lin, "Pulse delay measurements in the zero material dispersion wavelength region for optical fibers," Appl. Opt. **16**, 3136-3139 (1977).

[16] B. Costa, M. Puleo, and E. Vezzoni, “Phase-shift technique for the measurement of chromatic dispersion in single-mode optical fibers using LED,” Electron. Lett. **19**, 1074-1076 (1983).

[17] H. T. Shang, “Chromatic dispersion measurement by white-light interferometry on metre-length single-mode optical fibers,” Electron. Lett. 17, 603–605 (1981).

[18] M. Tateda, N. Shibata, and S. Seikai, “Interferometric method for chromatic dispersion measurement in a single-mode optical fiber,” IEEE J. Quantum Electron. **17**, 404–407 (1981).

[19] M. J. Gander, R. McBride, J. D. C. Jones, D. Mogilevtsev, T. A. Birks, J. C. Knight, and P. St. J. Russell, "Experimental measurement of group velocity dispersion in photonic crystal fibre,″ Electron. Lett. **35**, 63-64 (1999).

[20] M. G. Welch, C. E. de Nobriga, R. A. Correa, W. J. Wadsworth, and J. C. Knight, "Accurate measurement of the dispersion of hollow-core fibers using a scalable technique," Opt. Express **17**, 9006-9012 (2009).

[21] Bentham Instrument Ltd, http://www.bentham.co.uk/detectors.htm.

[22] J. M. Stone, J.C. Knight, “From zero dispersion to group index matching: How tapering fibers offers the best of both worlds for visible supercontinuum generation,” Optical Fiber Technology **18**, 315-321 (2012).

[23] A. W. Snyder and J. D. Love, Optical waveguide theory (Chapman & Hall, 1983).

Chapter 7 Summary and future work

In this thesis I have described my study of hollow core negative curvature optical fibres (HC-NCFs).

In Chapter 3, the simulation by *Comsol* demonstrated that the capillary thickness is the most important factor influencing the attenuation level of HC-NCFs. Due to the special structure of HC-NCF, the fibre loss caused by the cladding material absorption is 7500 times less than the material absorption itself. It implies that even in the spectral region where the fabrication material becomes completely opaque, HC-NCFs can still be used for light transmission. In the low loss spectral window, the simulation shows that HC-NCFs present extremely low dispersion property.

In Chapter 4, the fabrication for silica HC-NCFs was reviewed. Currently the main challenges of making good HC-NCFs mainly are maintaining the uniformity along the length and preventing the structural gradation in the cladding.

In Chapter 5 the attenuation properties of HC-NCFs were presented and the spectral limits of HC-NCFs were discussed. Nine best HC-NCFs with different dimensions were selected and their attenuations of the first bands in different wavelength ranges were shows and analysed. By fitting the lowest attenuations of those nine fibres as a function of wavelengths, the limit of attenuation was revealed for different wavelength ranges. In the shorter wavelength range below 1.5 μm, the scattering effect and the structural degradation of HC-NCFs may fundamentally limit the performance of fibres; in the long wavelengths after 3 μm, the material absorption causes the rising of fibre loss; finally the confinement loss dominates the wavelength range in between and the measured lowest attenuation recorded can be found there.

In Chapter 6 bending loss and dispersion of HC-NCF were discussed. Generally HC-NCF is sensitive to bending. The way bending influences the loss of HC-NCFs

were identified as the cladding mode coupling, higher order mode conversion and enhanced material absorption and surface scattering. The dispersion property of HC-NCF was experimentally measured by using a white light interferometer. A low GVD was found as expected.

Although my work has advanced the study of HC-NCFs, this field still remains fertile. The exploration of fabricating HC-NCFs with lower attenuations has not been finished especially at the short wavelengths in the visible and near infrared spectral range. The extension of fabrication materials may bring HC-NCFs into new spectrum where the fused silica becomes a fundamental limiting factor. New designs of HC-NCFs may decrease the attenuation level in the future and help us better understand the guidance mechanism of HC-NCFs. Meanwhile applying HC-NCFs in the high power laser transmission and ultrafast laser pulse delivery will continue being attractive for researchers from the science and industry.

A List of acronyms

TIR	Total internal reflection
HCF	Hollow core fibre
HC-PBG	Hollow core photonic bandgap fibre
PBG	Photonic bandgap fibre
PCF	Photonic crystal fibre
FOM	Figure of merit
SRS	Stimulated Raman scattering
FWHM	Full width at half maximum
GVD	Group velocity dispersion
SPM	Self-phase modulation
ISRS	Intrapulse stimulated Raman scattering
ARROW	Anti-resonant reflecting optical waveguide
HC-NCF	Hollow core negative curvature fibre
OSA	Optical spectrum analyser
SMF	Single mode fibre
NA	Numerical aperture
SCWs	Surface capillary waves

B Publication list

I. My Publications as the first author to the study of HC-NCFs which are fully presented in this thesis

Journals

Fei Yu and Jonathan C. Knight, "Spectral attenuation limits of silica hollow core negative curvature fiber," Opt. Express **21**, 21466-21471 (2013).

Fei Yu, William J. Wadsworth, and Jonathan C. Knight, "Low loss silica hollow core fibers for 3–4 μm spectral region," Opt. Express **20**, 11153-11158 (2012).

Conferences & Proceedings

J. C. Knight and F. Yu, "Silica Hollow Core Fibers for Mid-IR Wavelengths," in Workshop on Specialty Optical Fibers and their Applications, (Optical Society of America, 2013), paper T2.1.

F. Yu and J. C. Knight, "Limits of Hollow Core Negative Curvature Fiber," in conference on CLEO (San Jose, 2013), paper CTu2K.6.

F. Yu, W. J. Wadsworth, and J. C. Knight, "Low Loss (34 dB/km) Silica Hollow Core Fiber for the 3 &4 μm Spectral Region," in Specialty Optical Fibers, OSA Technical Digest (online) (Optical Society of America, 2012), paper SM3E.2

II. Other Publications

Journals

Zefeng Wang, Fei Yu, William Wadsworth, and Jonathan Knight, “Efficient 1.9 μm wavelength conversion by stimulated Raman scattering in H_2-filled hollow core fiber pumped with 1.06 μm microchip laser,” Opt. Express (submitted).

Piotr Jaworski, Fei Yu, Robert R.J. Maier, William J. Wadsworth, Jonathan C. Knight, Jonathan D. Shephard, and Duncan P. Hand, "Picosecond and nanosecond pulse delivery through a hollow-core Negative Curvature Fiber for micro-machining applications," Opt. Express **21**, 22742-22753 (2013).

A. Urich, R. R. J. Maier, F. Yu, J. C. Knight, D. P. Hand, and J. D. Shephard, "Flexible delivery of Er:YAG radiation at 2.94 μm with negative curvature silica glass fibers: a new solution for minimally invasive surgical procedures," Biomed. Opt. Express **4**, 193-205 (2013).

A. Urich, R.R.J. Maier, F. Yu, J.C. Knight, D.P. Hand, J.D. Shephard, “Silica hollow core microstructured fibres for mid-infrared surgical applications,” Journal of Non-Crystalline Solids, (March 28, 2013)

Conferences & Proceedings

H. Liu, F. Yu, A Chong, J. C. Knight and F. Wise, " Extended Self-Similar Pulse Evolution in a Laser with Dispersion-Decreasing Fiber," in conference on CLEO (San Jose, 2013).

P. Jaworski, F. Yu, R.R.J. Maier, W.J. Wadsworth, T.A. Birks, J.C. Knight, J.D. Shephard, and D.P. Hand, "Delivery of high-power nanosecond and picosecond pulses through a hollow-core Negative Curvature Fibre for micro-machining applications, " in conference on E-CLEO (Munich, 2013)

A. Urich, R. R. J. Maier, J. C. Knight, F. Yu, D. P. Hand, and J. D. Shephard, " Flexible delivery of Er:YAG radiation at 2.94 μm with novel hollow-core silica glass fibres: demonstration of tissue ablation, " Proc. SPIE 8576, Optical Fibers and

Sensors for Medical Diagnostics and Treatment Applications XIII, 857608 (March 20, 2013);

Y. Pan, S. Andrews, F. Yu, and J. C. Knight, “Single mode microstructured silica waveguide for broadband THz transmission,” in conference on the 3rd EOS Topical Meeting on Terahertz Science & Technology (European Optics Society, 2012).

L.E Hooper, P.J. Mosley, A.C. Muir, F. Yu, B.J. Mangan, W.J Wadsworth, J.C. Knight, and J.M. Dudley, "Coherent widely tunable source of sub-picosecond pulses using all-normal dispersion fiber supercontinuum," in conference on Fibre and Optical Passive Components (WFOPC) (Photonics Society, 2011).